A DEEP CHANDRA STUDY OF GALACTIC TYPE IA SUPERNOVA

REMNANT G299.2-2.9

by

SETH AARON POST

Presented to the Faculty of the Graduate School of

The University of Texas at Arlington in Partial Fulfillment

of the Requirements

for the Degree of

DOCTOR OF PHILOSOPHY

THE UNIVERSITY OF TEXAS AT ARLINGTON

December 2017

To my wife and children, whose constant love and support enabled me to reach further and succeed.

ACKNOWLEDGEMENTS

ABSTRACT

A DEEP CHANDRA STUDY OF GALACTIC TYPE IA SUPERNOVA

REMNANT G299.2-2.9

Seth Aaron Post, Ph.D.

The University of Texas at Arlington, 2017

Supervising Professor: Dr. Sangwook Park

In this thesis we perform a comprehensive analysis of Galactic Type Ia super-
nova remnant G299.2-2.9. For this study we analyze our deep 628 ks *Chandra* ob-
servation data of G299.2-2.9. G299.2-2.9 has a complex multiple shell-like structure
consisting of a bright inner shell, with enhancements ("knots") in the northeastern
portion of the shell, and a fainter diffuse outer shell. Our spectral analysis of the
outer shells of G299.2-2.9 shows that the bright inner and faint outer shells appear
to be emission features from the swept-up ambient medium (by the supernova blast
wave) whose density is relatively uniform along the distance from the center of the
remnant. We find a density gradient of a factor of $\sim$3 between the bright inner and
faint outer shells. Our analysis of the shell regions suggests that the multiple shell
morphology is likely the result of an explosion taking place on the boundary of two
regions of interstellar material with differing densities. Based on our equivalent width
images and elemental abundance measurements from our spectral analysis throughout
the entire remnant we reveal a highly asymmetrical spatial distribution of metal-rich
ejecta gas. The metal-rich ejecta gas is present mainly throughout the central regions

(surrounded by the outer shells of swept-up ambient medium). In particular we find an intriguing continuous extension of Fe- and Si-rich gas in the western direction. This asymmetric distribution of metal-rich ejecta gas is likely caused by an asymmetric explosion of the progenitor, but non-uniform expansion of the ejecta within the two regions of interstellar material with differing densities cannot be ruled out. We place a new conservative upper limit (8 kpc) on the distance to G299.2-2.9 based on our analysis of HI gas distribution along the line of sight. Based on our new distance upper limit, we place a tight constraint on the distance, $d \sim 5$ kpc (with $\sim$50% errors) to G299.2-2.9, and then we estimate an explosion energy $E_0 \sim 1.8 \times 10^{50}$ erg. We estimate a total Fe mass $M_{Fe} \sim 0.17$ $M_\odot$ and a total ejecta mass of $M_{ej} \sim 0.50$ $M_\odot$ for G299.2-2.9. These estimated values are significantly below those of a canonical Type Ia supernova. Based on these results we propose that G299.2-2.9 may be the result of a double detonation of a sub-Chandrasekhar mass white dwarf or the failed deflagration of a white dwarf.

TABLE OF CONTENTS

LIST OF ILLUSTRATIONS

LIST OF TABLES

CHAPTER 1

INTRODUCTION

1.1   Type Ia Supernova

Supernovae are among the brightest and most energetic events to occur within the universe and as such, they have captivated the imaginations of scientists for generations. Our knowledge and understanding into the nature of these unique phenomena have greatly expanded over the last few decades. These violent and explosive events are due to the gravitational collapse (core-collapse supernova) of massive stars or by the thermonuclear explosion of a white dwarf (Type Ia supernova). They shine with the brightness of several billion suns, typically outshining their host galaxy for many months thus, allowing them to be observed at great distances. These explosions expel stellar debris at velocities of up to $\sim$30000 km s^{-1} ($\sim$10% the speed of light). These stellar ejecta debris play a significant role in shaping and enriching the interstellar medium (ISM) with the heavy chemical elements (e.g, Whittet 2003, pp. 45-46) produced by nucleosynthesis throughout the lifetime of the star and also produced during the explosion itself. This enriched material then later gives birth to the next generation of stars and planets. Supernovae may potentially be sources of strong gravitational waves (Ott et al. 2012). Their remnants are expected to accelerate a large fraction of cosmic rays (Baade & Zwicky 1934). Because these events produce a wide range of astrophysical consequences they are important to many areas of investigation across a wide range of fields of study.

The Type Ia supernova is a subclass of supernovae that occurs in all types of galaxies. They have been detected both in star forming regions as well as areas with

little to no star formation activity. They are believed to occur at a rate of a few 10^{-3} yr^{-1} within our Galaxy (e.g., Maoz et al. 2014). They show early time ($t \sim 1$ week after explosion) optical spectra dominated by strong broad Si absorption lines with an absence of emission from H (Filippenko 1997). They also show line emission from elements like Si, Ca, Mg, S, and O. These elements are likely associated with the outer layers of the ejected stellar debris ("ejecta", hereafter). At late-times ($t \sim$ a few months after maximum light), when the outer layers have expanded to the point of transparency, Type Ia supernova spectra show blends of dozens of Fe emission lines, mixed with Co lines (Filippenko 1997). These Fe-peak elements are produced during the explosion itself. The evolution of the luminosity (Figure 1.1) for the majority of Type Ia supernovae is very similar. Their light curves quickly rise and reach a "homogeneous" peak luminosity ($M_B \sim$ -19.3 in the B-band) at $\sim$20 days after the explosion. After the peak luminosity, the light curve decreases exponentially, which is typical of emission powered by radioactive decay of ^{56}Ni through ^{56}Co to ^{56}Fe (Hillebrandt & Niemeyer 2000). This radioactive decay produces high-energy photons that dominate the energy output at intermediate and late times (i.e. $t \gtrsim 2$ weeks, Hillebrandt & Niemeyer 2000). Thus their peak luminosity is a direct product of the Ni and Fe produced during the explosion.

These overall characteristics of homogeneous peak luminosity and light curve, coupled with their high luminosity, make the majority of Type Ia supernovae ideal for use as "standardizable" candles (standard candles are objects with a small dispersion in their luminosities) to measure distances to the farthest reaches of the universe. This calibration of Type Ia supernovae as standard candles was first pioneered by a collaboration between Chilean and US astronomers for the Calán/Tololo Supernova Survey (Hamuy et al. 1993) in the early 1990's. The absolute magnitudes of unreddened Type Ia supernovae can be calibrated to standard candle values with

the Phillips relationship (Phillips 1993). The Phillips relationship is a linear relation between the absolute magnitude of Type Ia supernovae at maximum light and the magnitude decline of the B-band curve during the first 15 days following maximum luminosity. With the ability to measure greater and greater distances, we see further back in time, thus Type Ia supernovae show how the expansion of the universe has evolved since the Big Bang. In this manner the accelerating expansion of the universe was discovered independently by two groups of scientists in 1998 (Riess et al. 1998, Perlmutter et al. 1999). This unexpected discovery has transformed our understanding of cosmology and the structure of the universe. The utility of Type Ia supernovae as standard candles relies heavily on their "homogeneity" as described above, however, recent studies (e.g., Filippenko et al. 1992a, Li et al. 2011a) show that not all Type Ia supernovae are homogeneous in nature. Thus, it is essential to study the detailed nature of Type Ia supernovae in order to enhance their utility for precision cosmology.

The vast majority of "normal" Type Ia supernovae can be described as above, however, there exists a significant population ($\sim$20–35%) of "peculiar" Type Ia events (Li et al. 2011a). For example, sub-luminous supernova 1991bg-like events (Filippenko et al. 1992a) account for $\lesssim$15% of the total Type Ia supernovae rate (Li et al. 2011a). These events are characterized by peak magnitudes between 1.6 and 2.5 magnitudes below ordinary Type Ia supernovae, faster decline times, and somewhat lower expansion velocities. They are detected almost exclusively in early type galaxies (Doull et al. 2011, Sullivan et al. 2011). Supernova 2002cx-like events are another group of sub-luminous Type Ia supernovae that account for $\sim$5-15% of Type Ia supernovae (Li et al 2011a, 2011b, Foley et al. 2013) although a core-collapse explosion has been suggested as an alternative (Valenti et al. 2009, Lyman et al. 2013). 2002cx–like events are characterized by peak absolute magnitudes $\sim$2 less than ordinary Type Ia

supernovae, low expansion velocities at peak light, and strong mixing of the stellar ejecta. They are found predominately in late-type galaxies (Li et al. 2003, Jha et al. 2006, Foley et al. 2009, 2013).

1.2   Evolutionary Routes and Explosion Mechanisms of a Type Ia Supernova

Our knowledge concerning Type Ia supernovae and their progenitors is far from complete. After over a century of searching we still lack a direct observation of a progenitor for a Type Ia supernova (Kotak 2008). Nevertheless, several lines of evidence point to at least one carbon-oxygen (CO) white dwarf in the progenitor system. Type Ia supernovae have a layered ejecta (stellar debris previously contained within the star and now ejected by the explosion) composition with Fe-peak elements in the center and intermediate-mass elements such as Si and S on the outside as suggested by their spectroscopic evolution (Hillebrandt & Niemeyer 2000). Neither H nor He have been observed in most Type Ia supernova spectra (Leonard 2007). Type Ia supernovae are not associated exclusively with young stars, as are other types of supernovae (van Dyk 1992). All these combined point to Type Ia supernovae as the thermonuclear explosion of CO white dwarfs within close binary systems.

White dwarfs are the dense (typically with mass densities of $\sim 10^4$–10^7 g cm^{-3}) slowly cooling stellar cores of main sequence stars that were not massive enough to experience a gravitational collapse. Stars of very low mass (<0.5 $M_\odot$) would never become hot enough to fuse He in the core. Eventually they would burn all their H leaving behind a dense He core (Laughlin et al. 1997). Stars whose individual masses are ~ 0.5–8.0 $M_\odot$ would be hot enough to fuse He into C and O but they would never reach temperatures hot enough to burn C into Ne (Kippenhahn & Weigert 2012). Such a star, after becoming red giant, would shed its outer layers and form a planetary nebula, leaving behind a CO core. The individual masses of these CO

cores would be $\sim$0.6–1.2 $M_\odot$ (Fisher & Jumper 2015), depending upon the mass of the progenitor star in the main sequence. White dwarfs no longer undergo fusion reactions and as such they no longer have a source of internal energy to generate heat to support their hydro-static equilibrium against gravitational collapse. Instead electron degeneracy pressure forms in the extremely dense core and keeps the white dwarf from gravitational collapse. A white dwarf can only be supported in this manner for masses up to the Chandrasekhar mass limit of $\sim$1.44 $M_\odot$ (or 1 M_{Ch}).

CO white dwarfs that accrete material from a companion star would eventually reach the Chandrasekhar mass limit. As the mass of the white dwarf increases, its internal pressure and temperature may rise high enough in the core to begin C fusion. The ignition of C fusion may spread unevenly outwards in microscopically thin layers that propagate either by shock compression as supersonic detonations or conductively as subsonic deflagrations (Hillebrandt & Niemeyer 2000). The nucleosynthesis products in these processes are sensitive to the density and internal temperature of the white dwarf. In a supersonic detonation there would be no time for the white dwarf to expand as it burns, leaving the core at a high density and temperature, thus producing far too much Fe-peak nuclei and too little intermediate mass elements to match observations (Hillebrandt & Niemeyer 2000). A subsonic deflagration gives the white dwarf time to expand as the burning front propagates, lowering the density and temperature of the core, thus producing less Fe-peak nuclei and more intermediate mass elements. However the burning front would expand slowly, making it impossible to produce sufficiently energetic explosions to match observations (Khokhlov 1995). Another proposed mechanism is the formation of a deflagration front which then at some point transitions to a supersonic detonation (Khokhlov 1991a). In this process a substantial fraction of C and O within the white dwarf is rapidly converted into heavier elements such as Fe, Ni, Si and S. The energy released ($\sim$10^{51} erg) from this

process is large enough to unbind the white dwarf, causing it to explode violently as a Type Ia supernova.

1.2.1 Single-Degenerate Channel

The single-degenerate channel involves a progenitor system originally consisting of two main sequence stars. The star with the greater mass evolves more rapidly into an asymptotic giant branch star. It eventually looses mass and ejects its outer layers as a planetary nebula, leaving behind the compact white dwarf. If the orbit is sufficiently close the white dwarf may accrete material from its companion main sequence, sub-giant or red giant star through Roche-lobe overflow or by stellar wind (e.g., Maoz & Mannucci 2013). In all cases the white dwarf accretes material from its companion star, growing until it reaches the Chandrasekhar mass and explodes. The evolution of the progenitor system during the accretion phase remains uncertain. It depends heavily upon the rate of accretion and the transfer of angular momentum to the white dwarf (Langer et al. 2002).

Some observational evidence supports the single-degenerate model. Variable blue-shifted Na I absorption lines have been detected in the spectra of several Type Ia supernovae (Patet et al. 2007, Simon et al. 2009). These absorption lines are believed to be caused by the interaction of the blast wave shock front with the stellar wind material ejected from the progenitor system prior to the supernova explosion. Such systems are believed to account for $\sim$20–25 % of Type Ia supernovae (Sternberg et al. 2011). In a single-degenerate system the exploding white dwarf is most likely near the Chandrasekhar mass and thus has a high density core ($\sim$2 $\times$ 10^9 g cm^{-3}). This would lead to efficient electron captures which increase nucleosynthesis yields of ^{56}Ni and ^{55}Mn (Yamaguchi et al. 2015). The X-ray spectral analysis of the Type Ia supernova remnant 3C 397 shows strong K-shell emission from ^{56}Ni and ^{55}Mn

consistent with yields from a white dwarf near the Chandrasekhar mass limit and thus likely from a single-degenerate progenitor system.

On the other hand, in order to grow to the Chandrasekhar mass limit theoretical models suggest that a white dwarf must accrete material in a narrow mass transfer range ($\sim 10^{-7}$ $M_\odot$ yr^{-1}; Branch et al. 1995). Below this rate the white dwarf will experience explosive burning leading to a nova (Townsley & Bildsten 2005). If the rate is above the limit, the white dwarf would likely evolve back to a red giant-like configuration. It would then significantly expand and engulf the donor within a common envelope (Iben & Tutukov 1984, Maoz et al. 2014). The white dwarf would no longer continue to grow in mass and no Type Ia supernova would ensue (Maoz et al. 2014). Some of the material that a white dwarf accretes from its companion may burn steadily (not explosively like a nova) at the surface of the white dwarf and could be visible as super soft x-ray sources (the emission spectrum is dominated by soft X-rays at photon energies < 0.5 keV; Di Stefano 2010). However, there is a lack of observational evidence from these X-ray sources in the Galaxy to account for the majority of Type Ia supernovae (Di Stefano 2010). The single-degenerate model also has difficulty in explaining the observed rate of Type Ia supernovae or producing Type Ia supernovae with long delay times (longer that 10 Gyr), where the delay time distribution is the distribution of time-lapses between star formation and supernova explosion (Maoz et al 2014). It is also expected that the binary companion star would survive the Type Ia supernova and might be detectable, however no evidence for a companion star has been detected in pre-explosion images (Li et al. 2011a) or later in the supernova remnant phase (e.g., Kerzendorf et al. 2009, Schaefer & Pagnotta 2012). It is notable though, that recent observations of pre-maximum light show signatures of shocks from the supernova ejecta hitting the companion star in both a

subluminous Type Ia (Cao et al. 2015) and a normal Type Ia supernova (Marion et al. 2015).

1.2.2 Double-Degenerate Channel

The double-degenerate channel involves a close binary system containing two white dwarfs. The combined mass of the white dwarfs in this system exceeds the Chandrasekhar limit (Iben & Tutukov 1984). Both white dwarfs orbit close together (with an orbital period of <15 hours), gradually loosing energy and angular momentum through gravitational wave radiation. The less massive of the two white dwarfs is tidally disrupted and forms an accretion disk around its more massive companion. The more massive white dwarf accretes material from the accretion disk until it reaches the Chandrasekhar mass limit and explodes. An alternative path is the so-called violent merger scenario (Pakmor 2010, 2012). Here two white dwarfs of approximately equal masses (>0.9 $M_\odot$) merge to produce a Type Ia Supernova. Again the less massive white dwarf is tidally disrupted and forms an accretion disk around its companion. During this process "hotspots" begin to form on the surface of the white dwarf due to compression heating. In the hottest regions C burning ignites, further heating the white dwarf leading to a detonation at high enough densities. It has also been proposed that mergers of equal mass white dwarfs with combined masses below that of the Chandrasekhar mass limit (but with individual masses $\gtrsim$0.6 $M_\odot$) may also explode as Type Ia supernovae if they heat up sufficiently to ignite C (van Kerkwijk et al. 2010, Badenes & Maoz 2012).

The double-degenerate channel can naturally explain the lack of H observed in the spectra of Type Ia supernovae as they occur long after the circumstellar material (CSM) from stellar winds and mass loss have dissipated into the ISM. The predicted theoretical rate of the double-degenerate scenario can better explain (than all other

Type Ia models) the observed rate of Type Ia supernovae but still is unable to account for all Type Ia supernovae (Maoz & Dan 2013). The greatest stumbling block for the double-degenerate channel is the need to avoid accretion-induced collapse of the white dwarf (Nomoto & Iben 1985). As the nuclear flame propagates inward the CO white dwarf transitions into an O-Ne-Mg white dwarf. If the O-Ne-Mg white dwarf reaches the Chandrasekhar mass limit, the electron capture on Ne and Mg may cause an accretion induced collapse of the white dwarf into a neutron star. Another issue is that the total mass of the double-degenerate model would vary and generally would be greater than the Chandrasekhar mass limit, hence the total luminosity would also significantly vary, which does not fit most observations of Type Ia supernovae. The predicted light curves and spectra for double-degenerate mergers are generally not in good agreement with those observed from normal Type Ia supernovae (Maoz & Dan 2013). Also the violent merger scenario would produce highly asymmetric ejecta (Pakmor 2012) which is typically not the case for observed Type Ia supernovae (Wang & Wheeler 2008) or in their remnants (Lopez et al. 2009).

1.2.3 Core-Degenerate Scenario

In the core-degenerate scenario a massive asymptotic giant branch star would fill its Roche-lobe and transfer mass onto a white dwarf companion. This mass transfer process is unstable and a common envelope soon evolves. Both stars spiral in towards each other as they loose angular momentum and energy from gravitational radiation, tidal friction, and drag (Kashi & Soker 2011). The white dwarf eventually merges with the hot core of the asymptotic giant branch star (Livio & Riess 2003). The explosion would occur either shortly after the common envelope phase (where the supernova ejecta would interact with the ejected common envelope) or after a very long delay time (where any mass loss from the progenitor has dissipated into the

ISM). If the explosion takes place shortly after the common envelope phase then it would take place inside a planetary nebula.

The hot core of the asymptotic giant branch star may be larger than its colder white dwarf companion. This means that an off-center ignition of carbon is unlikely to occur. The merger may then avoid accretion induced collapse that plagues the double-degenerate channel (Soker 2012). This scenario can explain the H lines found in spectrum from some Type Ia supernovae[1], when the merger happens shortly after the common envelope phase. However, the Type Ia supernova birth rate from this scenario is not well determined and may only account for a small fraction (<20%) of all Type Ia supernovae (Maoz & Mannucci 2013).

1.2.4   Double-Detonation scenario

In this scenario a sub-Chandrasekhar mass white dwarf accretes He-rich material from a companion donor He white dwarf or He main sequence star (Woosley & Weaver 1994). As more material accretes onto the white dwarf it is compressed and eventually detonates on the surface of the white dwarf, leading to a second detonation near the center of the white dwarf (Shen 2013). Models have successfully demonstrated detonations in white dwarfs with masses from as little as 0.45 $M_\odot$ up to 1.1 $M_\odot$ with the He-rich layer having a mass of 0.05–0.2 $M_\odot$ (Sim et al. 2010, Fink et al. 2010, Kromer et al. 2010). Most simulations of double detonations have shown that significant masses of unburnt He should be present in the outer layers of the ejecta.

According to population synthesis studies, only a fraction ($\lesssim$50%) of Type Ia supernovae can occur via this scenario (Ruiter et al. 2011). Their explosions

---

[1]A few Type Ia supernovae, notably 2002ic [Livio & Riess (2003)] and PTF 11kx [Dilday et al. (2012)], show H lines in their spectra at late times.

are highly asymmetrical leading to asymmetrical remnants, probably with dipole asymmetry (Papish et al. 2015). This asymmetry has not been observed within any well-resolved Type Ia supernova remnant (Badenes et al. 2007). The mass of the white dwarf prior to its explosion is predicted to be <1.2 $M_\odot$, which is inconsistent with the finding that a little over half of Type Ia supernovae have ejecta masses near and/or above the Chandrasekhar limit (suggesting that all Type Ia supernova cannot be described by the double-detonation model, Scalzo et al. 2014). Most double-detonation models show light curves and spectral properties that differ from observations. These discrepancies are believed to be caused by line contamination from heavy elements in the ash associated with the detonation of the helium layer (Fink et al. 2007).

1.2.5   Direct Collision scenario

Unlike the double-degenerate scenario where a binary system of two white dwarfs slowly merge over time due to gravitational wave radiation, the direct collision scenario results in two white dwarfs directly colliding. The collision prompts an immediate detonation resulting in a Type Ia supernova. This scenario may take place within triple star systems or dense stellar environments (Katz & Dong 2012, Kushnir et al. 2013).

Simulations for white dwarf-white dwarf collisions predict high velocity intermediate mass elements in the outer layers of the ejecta as seen in observations of Type Ia supernovae. They may also produce a wide range of ^{56}Ni masses, which is dependent upon the total mass of the two white dwarfs. Calculations of light curves and spectra are in reasonable agreement with observations of normal Type Ia supernovae (Rosswog et al. 2009). Nevertheless, the direct collision scenario may also have difficulties explaining the total rate of Type Ia supernovae (Scalzo et al. 2014).

11

Also the explosion is highly non-spherical which is not consistent with observations of nearby Type Ia supernova remnants (Lopez et al. 2009). In this scenario it is difficult to produce explosive events at early delay times (<0.4 Gyr; Scalzo et al.2014).

1.3 Evolution of Supernova Remnants

Supernovae are energetic explosions that do not fade away soon after the explosion. The blast wave or "forward shock" resulting from a supernova explosion expands into interstellar space interacting with its environment for many years. The metal-rich ejecta expands behind the forward shock enriching the ISM with the nucleosynthesis products created inside the star (before the explosion) and during explosion itself. This complex structures of shocked gas and stellar debris is the so-called supernova remnant. The metal-rich ejecta directly reveals the nucleosynthesis products from the explosion and thus provides insight into the explosion mechanism and the progenitor star's nature. As the forward shock propagates outward from the supernova explosion it sweeps up the ambient ISM, heating it to temperatures of $T \sim 10^7$ K. This "hot" phase during the expansion of the supernova remnant may last for $\sim 10^4$ yr.

Supernova remnants evolve through three characteristic phases over the course of their lives (Chevalier 1977). The first of these phases is the ejecta-dominated or "free-expansion" phase. Initially the material from the supernova explosion expands outwards in ballistic motion into the interstellar gas. At this point the surrounding ISM has no influence on the expansion of the shock wave because the pressure of the interstellar gas is negligible. This "free-expansion" phase of the supernova remnant may last up to $\sim 10^3$ years (depending upon the density of the ambient medium with which it interacts).

As the remnant matures and sweeps up more and more ambient material the swept-up mass of the interstellar material becomes comparable with that of the ejecta.

Now the remnant moves into the next phase of its life, the "Sedov phase". As the forward shock propagates outward, the pressure behind the shock wave decreases (McKee 1974). This causes the material inside the forward shock to cool adiabatically. An inward-facing "reverse shock" forms behind the forward shock (Figure 1.2). This reverse shock reheats the ejecta material behind the forward shock as it travels inward (e.g., Reynolds 2008). The boundary that separates the forward shock-heated ISM to that of the reverse shock-heated ejecta material is known as the contact discontinuity (CD; Figure 1.2). The forward shock continues to propagate outwards sweeping up the ISM and forming a dense shell. The forward shock decelerates as it interacts with ISM, therefore the remnant expands adiabatically. This produces a dynamic structure that can be described by the self-similar Sedov-Taylor solutions (hence the name of this phase). The solutions describe a point explosion with a spherically symmetric adiabatic expansion within a uniform ambient medium with negligible pressure (Sedov 1959). The one dimensional solutions governing this dynamical expansion are described in Equations 1.1, 1.2 and 1.3, where r is the radius of the forward shock, t is the time since the explosion, ρ is the mass density of the material into which the shock is expanding, E_0 is the kinetic energy of the explosion, and v_{shock} is the velocity of the forward shock.

$$E_0 = \sim 0.7 r^5 t^{-2} \rho \tag{1.1}$$

$$v_{shock} = \frac{dr}{dt} = \frac{2}{5} E_0^{\frac{1}{5}} \rho^{-\frac{1}{5}} t^{-\frac{3}{5}} = \frac{2}{5} \frac{r}{t} \tag{1.2}$$

$$r = \sim 1.1 E_0^{\frac{1}{5}} \rho^{-\frac{1}{5}} t^{\frac{2}{5}} \tag{1.3}$$

The two-shock structure (forward and reverse shocks) evolves self-similarly, having a constant ratio between the forward shock, reverse shock and CD radii. This structure would persist until the reverse shock reaches the inner ejecta material where the ejecta density is close to constant. The overall central ejecta distribution can be approximated by a power law in the outer layers of this constant density region at which point it would accelerate and quickly shock the central-most parts of the stellar debris. The Sedov phase may last up to several thousand years. These middle aged supernova remnants may produce emission from approximately two characteristic components of the hot gas, representing the superposition of the radiation from the forward shock heated ambient gas with that from the reverse-shock-heated stellar debris gas.

The final phase starts when the mass of the swept-up ISM becomes much larger than that of the interacting ejecta. At this point radiative cooling dominates and the adiabatic approximation breaks down for the forward shock front. This phase is also known as the "snow-plow phase". Once most of the forward shock has become radiative the shell would coast outwards due to significant pressure provided by the hot interior which is still expanding adiabatically. As the ejecta cools the expansion of the remnant enters a momentum-conserving phase. The remnant would eventually merge with its surroundings as the shock speed becomes comparable to the sound speed of the ISM. This process is estimated to take place over $\sim 10^6$ years.

1.4 Galactic Type Ia Supernova Remnant G299.2-2.9

Galactic supernova remnant G299.2-2.9 was first discovered in the *Röntgenstrahlen* (*ROSAT*) all sky survey (Busser & Aschenbach 1995). Observations with *ROSAT*, *Einstein Observatory* and the *Advanced Satellite for Cosmology and Astrophysics* (*ASCA*) all reported an X-ray morphology consisting of a "centrally" enhanced emis-

sion with a partial shell-like structure (Busser & Aschenbach 1995, Slane et al. 1996, Bai & Wang 2000; Figure 1.3). The X-ray spectrum was dominated by thermal emission with no detection of non-thermal synchrotron emission that would have originated from a pulsar wind nebula near the center of the remnant or from relativistic electron accelerations at the forward shock front. The early *ROSAT* PSPC data could not distinguish between a young/nearby and a middle-aged/distant remnant. Later works supported a middle-aged remnant ($\tau \sim$ 5000–7000 yr; where τ is the time since the explosion) located at a distance $d \sim 5$ kpc (Slane et al. 1996, Bai & Wang 2000). However, these distance estimates are speculative, involving large uncertainties as they are not based on robust measurements of physical quantities[2]. These works estimated an explosion energy of $E_0 \sim 0.1$–0.3×10^{51} erg, substantially lower than the canonical value of 10^{51} erg.

Because of the relatively small angular size ($\sim 15'$) of supernova remnant G299.2-2.9 coupled with the poor angular resolution ($\sim 30''$–$2'$) of the detectors used in the previous studies the true morphology of G299.2-2.9 was not revealed until the *Chandra* study performed by Park et al. (2007). Park et al. (2007) discovered a complex multiple shell-like structure consisting of a bright inner shell, with enhancements ("knots") in the northeastern portion of the shell, and a fainter diffuse outer shell (Figure 1.4). The knots are located at a position where the inner and outer shells connect or overlap. The estimated angular size of the bright inner shell is $\sim 9'$–$10'$ in diameter, while the faint outer shell extends out to $\sim 13'$. They showed that an average density variation by a factor of ~ 3 exists between the bright inner shell and

---

[2]Slane et al. (1996) estimated a large distance in order to obtain a self-consistent model that could reproduce the observed X-ray and IR fluxes; Bai & Wang (2000) based their distance estimates on the relatively large N_H values obtained from their spectral model fits of the *ASCA* spectrum of the entire supernova remnant.

the faint outer shell. Based on these results, Park et al. (2007) proposed that G299.2-2.9 may have exploded near the boundary of two distinct density regions of ISM. In this scenario two "hemispheres" of the expanding shells may propagate into ambient medium with distinctive densities, respectively. One hemisphere would expand into the relatively low density medium with a relatively high velocity. The other hemisphere would expand into the relatively high density medium with a relatively low velocity. These hemispheres (when seen in superposition along the line of sight) may result in the "double-shell" morphology observed in G299.2-2.9. The observed X-ray spectra from the bright inner shell exhibit an average electron temperature of $kT \sim 0.5$ keV (where k is the Boltzmann constant), an ionization timescale $n_e t \sim 4.9 \times 10^{11}$ cm^{-3} s (where n_e is the electron density and t the time since the gas was shocked), and sub-solar metal abundance values (~ 0.5–0.7 with respect to solar; Anders & Grevesse 1989). The spectra from the faint outer shell indicate an average electron temperature of $kT \sim 0.7$ keV and an average ionization timescale $n_e t \sim 1.8 \times 10^{11}$ cm^{-3} s, and sub-solar metal abundance values. The measured sub-solar abundances indicate that the origin of these shells is the shocked ISM with low metal abundances. Park et al. (2007) discovered a previously undetected faint emission feature from the central region with an angular size of $\sim 4'$. This faint central region shows strong atomic spectral line features due to emission from overabundant Fe, Si, and S, which indicates the presence of reverse shock heated metal-rich stellar debris. Park et al. (2007) found that the Si-to-Fe mass ratio (~ 0.52) was in good agreement with Type Ia supernova models and thus proposed a Type Ia classification for the remnant. Park et al. (2007) found a lack of enhanced O and Ne in the spectrum of the metal-rich ejecta, which is also in good agreement with Type Ia supernova models. Based on N_H values obtained from their spectral model fits of *Chandra* spectrum, Park et al. (2007) estimated the distance to G299.2-2.9 to be ~ 5 kpc. This distance

estimate is crude, based on comparisons between the measured N_H for G299.2-2.9 and the general N_H distribution along the Galactic disk, and involves a factor of ~ 2 uncertainties. Assuming $d \sim 5$ kpc to G299.2-2.9 Park et al. (2007) estimated an explosion energy of $E_0 \sim 1.6 \times 10^{50}$ erg and an age of $\tau \sim 4500$ yr for the remnant.

It is notable that the complex multiple shell X-ray morphology of G299.2-2.9 is inconsistent with those of standard Type Ia supernova remnants. This complex shell morphology of G299.2-2.9 may indicate that the shock front is expanding into a non-uniform ISM or into medium that has been modified by the progenitor system. Estimates of the explosion energy for G299.2-2.9 appear to be lower than canonical values. However, the distance to G299.2-2.9 is rather speculative with large uncertainties, which leads to large uncertainties in the age, size and explosion energy of this supernova remnant in the previous works. Most Type Ia remnants are relatively spherical or axially-symmetric in shape (Lopez et al. 2009,2011) unlike the morphology of G299.2-2.9, where two distinctive "complete" shells are clearly observed. Kepler's supernova remnant is another unusual supernova remnant that shows similar properties to those of G299.2-2.9. Both are Type Ia supernova remnants that show shocks interacting with non-uniform ambient medium (Reynolds et al. 2007, Katsuda et al. 2015). On the other hand, G299.2-2.9 appears to be the result of a sub-energetic Type Ia supernova explosion, while Kepler is likely a luminous Type Ia supernova explosion (Patnaude et al. 2012) from a metal-rich white dwarf (Park et al. 2013). Kepler's supernova remnant is an order of magnitude younger than G299.2-2.9. Thus, G299.2-2.9 may represent a complementary opportunity (to Kepler) for the study of this group of peculiar Type Ia supernova remnants.

1.5 *Chandra* X-Ray Observatory

The shock-heated plasma found within supernova remnants spends a significant amount of its lifetime radiating in X-rays. Thus, X-ray observations of supernova remnants are effective for the study of the stellar debris as well as for the study of swept-up ISM. We performed our observations of G299.2-2.9 using the *Chandra* X-ray Observatory. The *Chandra* X-ray Observatory was first proposed to NASA in 1976 under the name of *Advanced X-ray Astrophysics Facility. Chandra* is a satellite in a 64-hour orbit around Earth, which was launched in July of 1999. *Chandra* was originally scheduled with a mission length of 5 years but in 2001 the mission plan was lengthened to 10 years due to the "observatory's outstanding results". Currently after over 17 years of operation *Chandra* is still going strong gathering data that have greatly advanced nearly the entire fields of astronomy. Examples of discoveries made based on *Chandra* observations include; the X-ray emission seen from the super massive black hole at the center of the Milky Way (Baganoff et al. 2001), the earliest images in X-rays of the shock wave of a supernova (Supernova 1987A; Burrows et al. 2000), and Jupiter's X-rays coming from poles (Gladstone et al. 2002).

Chandra's High Resolution Mirror Assembly consists of four pairs of nested grazing-incidence mirrors along with their support structure (Figure 1.5, Burke et al. 1997). The thick mirror substrate along with careful polishing provides an unmatched angular resolution (0.492″ on axis), allowing *Chandra* to collect $\sim$80–95% of incoming X-rays within a circular region of 1″ radius. *Chandra's* $\sim$0.5″ angular resolution is an order of magnitude better than that of the first orbital X-ray imaging telescope (*Einstein*; Giacconi et al. 1979). *Chandra's* Science Instrument Module consists of two instruments, the High Resolution Camera (HRC, Murray 1997) and the Advanced CCD Imaging Spectrometer (ACIS; Garmire et al. 1997). Both instruments consist of a spectroscopic array (HRC-S and ACIS-S, used in conjunction with transmission

gratings) along with an imaging array (HRC-I and ACIS-I) intended for wide field imaging.

The ACIS (Figure 1.6) is a focal plane instrument capable of measuring the position and energy of incoming X-ray photons. The ACIS-S consists of a 6 by 1 array of charged coupled devices (CCDs), including 4 front-illuminated and 2 back-illuminated CCDs. The ACIS-S array provides a $8' \times 51'$ field of view. Front-illuminated CCDs have the gate electrodes facing towards the incoming photons, giving them a slightly higher quantum efficiency (than back-illuminated CCDs) at photon energies of $E \gtrsim 3$ keV). Back-illuminated CCDs have the gate electrodes facing away from the incoming photons, giving them greater quantum efficiency (than front-illuminated CCDs) at photon energies of $E \lesssim 1$ keV). The ACIS-I consists of a 2 by 2 array of front illuminated CCDs providing a $17' \times 17'$ field of view. The good energy resolution ($\sim$95 eV at $E = 1.49$ keV) and superior spatial resolution ($\sim 0.5''$) allow for detailed spectroscopic investigations of relatively small features found within large extended sources such as the substructure in supernova remnants.

1.6   Software Tools

We use the *Chandra* Interactive Analysis of Observations (CIAO) in order to process and analyze the data we obtained from our *Chandra* observations of G299.2-2.9. CIAO is the standard software package for the data reduction and analysis of the *Chandra* observational data, and it is publicly available through the *Chandra* X-Ray Center (http://cxc.harvard.edu/ciao/). We used CIAO version 4.3 for our initial work and later upgraded to 4.6.1 (for its better scripting ability) when it became available for the works presented in this thesis. We use the X-ray data analysis software package, HEASOFT which is provided by the High Energy Astrophysics Science Archive Research Center (HEASARC) at NASA's Goddard Space Flight

Center (http://heasarc.gsfc.nasa.gov/lheasoft/). We perform our spectral model fits to the *Chandra* data (see Sections 2.2–2.5) using a HEASOFT tool XSPEC versions 6.12 and 6.15. XSPEC is an X-ray spectral-fitting program designed to be detector-independent so that it can be used for the analysis of spectral data taken with any spectrometer. We also use the Interactive Spectral Interpretation System (ISIS; http://space.mit.edu/asc/isis/) for some spectral analysis. ISIS is a spectral fitting tool similar to XSPEC yet it has the ability to automate repetitive data analysis tasks and take full advantage of multi-core processing, which is needed for our extensive spectral analysis of G299.2-2.9 utilizing an adaptive mesh algorithm (see Section 2.5). We apply an adaptive mesh algorithm using our own version of the software that we developed here at UTA's supernova remnant group.

1.7   Spectral Modeling of X-Ray Emission from Supernova Remnants

The observed X-ray spectrum of supernova remnants is dominated by emission from optically-thin plasma, containing atomic X-ray emission lines for a wide range of ionization states. In order to characterize the X-ray emission from G299.2-2.9 we fit the observed X-ray spectrum with an absorbed non-equilibrium ionization (NEI) plane-parallel shock spectral model (Borkowski et al. 2001, VPSHOCK in XSPEC) based on the atomic data ATOMDB (Foster et al. 2012). We use NEI version 2.0 to correctly measure prominent lines from highly ionized (H- and He-like) X-ray-emitting ions. This model can also account for "inner-shell" lines from Li-like ions which are important to measure electron temperatures for under-ionized gas (Badenes et al. 2006). The latest Fe-L shell lines at $E \sim$ 0.7-1.2 keV (Badenes et al. 2006) are also included. This model characterizes the X-ray spectrum with the following parameters; the electron temperature, the abundances for a number of elements (including C, N, O, Ne, Mg, Si, S, Fe, and Ni; measured with respect to solar values), the ionization

timescale $n_e t$, and a normalization parameter (see Equation 1.4), related to the scaled volume emission measure (see Equation 1.5),

$$normalization = \frac{10^{-14} EM}{4\pi D_A^2}.$$ (1.4)

In Equation 1.4, D_A is the the distance (in cm) to the source and EM is the volume emission measure,

$$EM = \int n_e n_H dV.$$ (1.5)

In Equation 1.5, n_H is the post-shock hydrogen number density, n_e is the electron number density, and V is the X-ray emitting volume.

1.8 Thesis Composition

In Chapter 2 we present our *Chandra* data analysis of G299.2-2.9 to study the structure and nature of the metal-rich ejecta and the swept-up ambient medium in this remnant. In Chapter 3 we discuss our results concerning the spatial and chemical distributions of the stellar ejecta debris. We also discuss the nature of the complex multiple shell-like structures of swept-up ambient medium. We estimate the explosion energy and age of the remnant along with the total ejecta mass and Fe ejecta mass. Based on these results we explore viable scenarios for the progenitor system of G299.2-2.9. In Chapter 4 we present a summary and conclusion. Part of this thesis has been published in *The Astrophysical Journal Letters* (Post et al. 2014). We will submit the unpublished part of this thesis to *The Astrophysical Journal* (Post et al. 2018, in preparation).
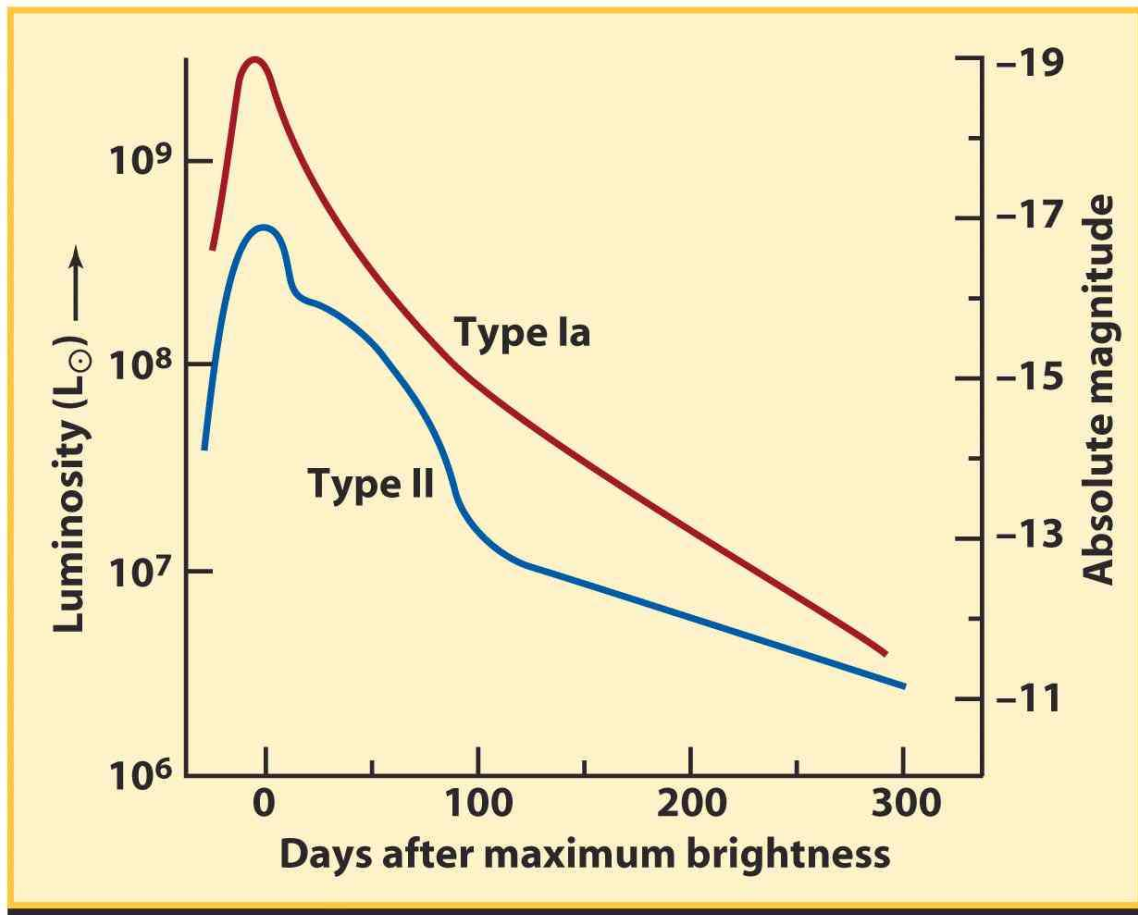
Figure 1.1 Cartoon representation of the light curves for Type Ia and Type II (a subtype of core-collapse) supernovae. The red curve represents light curve of a normal Type Ia supernova and the blue curve represents the light curve of a Type II supernova. Credit: NASA's Goddard Space Flight Center / Nick Short
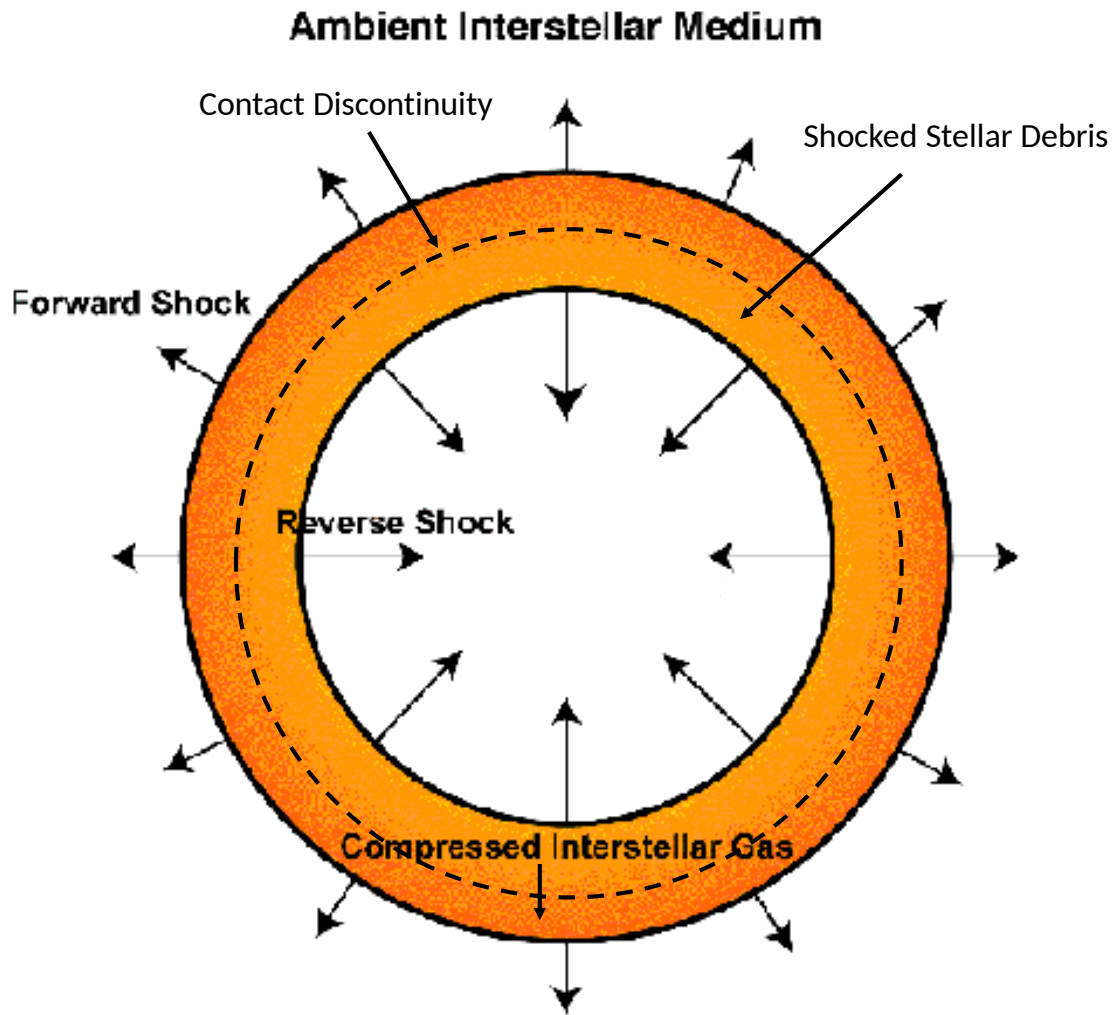
Figure 1.2 Cartoon representation of the shock structure of a supernova remnant. The forward shock is the outermost limit of the remnant. The reverse shock travels backwards into the metal-rich ejecta material. The contact discontinuity is the boundary that separates the forward shock-heated ISM to that of the reverse shock-heated ejecta material. Credit: https://heasarc.gsfc.nasa.gov/docs/objects/snrs/cartoon.html

ASCA OBSERVATION OF G299.2 − 2.9
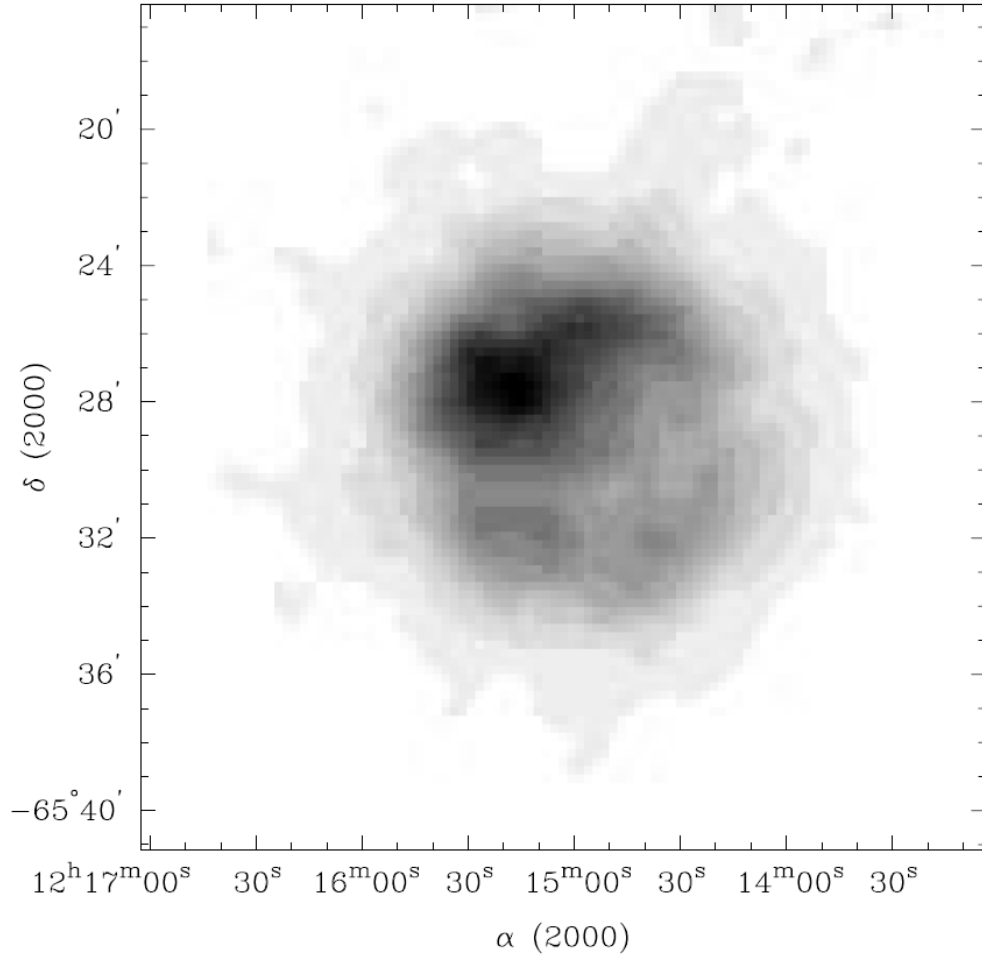
Figure 1.3 Image of G299.2-2.9 extracted from *ASCA* GIS data. The image was smoothed with a $\sigma = 29''$ Gaussian. Credit: Bai & Wang (2000)
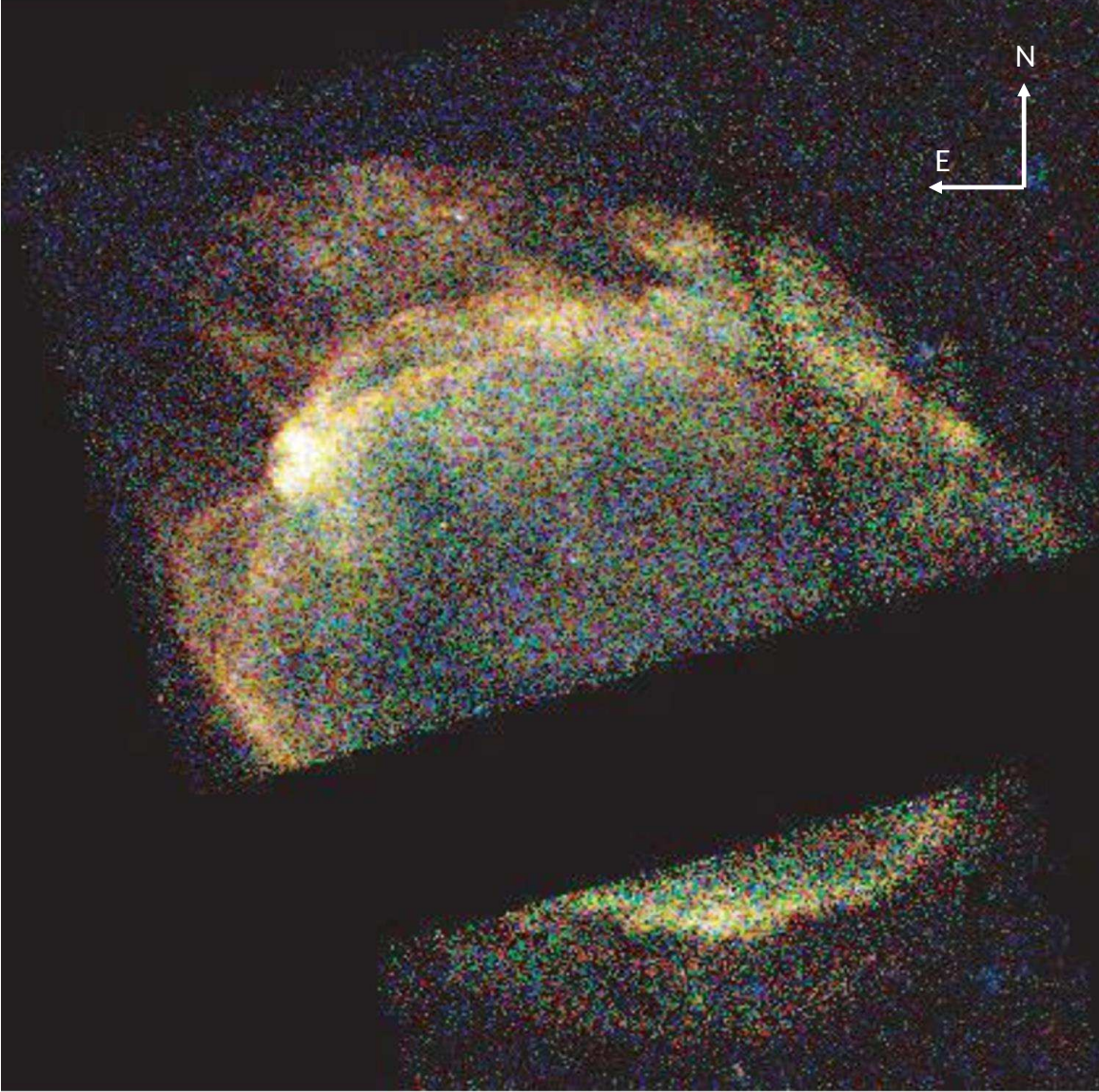
Figure 1.4 *Chandra* ACIS three-color image of G299.2-2.9 (this *Chandra* data is not used for this thesis). Red represents 0.4–0.9 keV, green 0.9–1.4 keV and blue 1.4–3.0 keV. All suband images have been exposure corrected and binned by 4 pixels. Credit: Park et al. (2007)
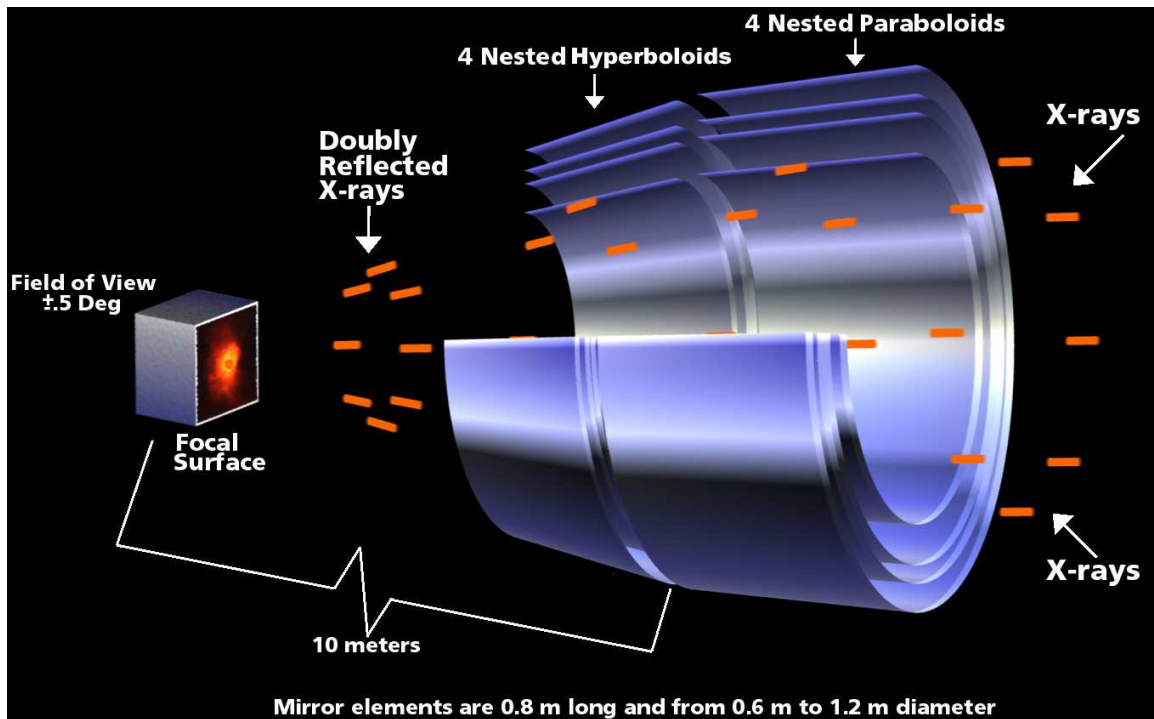
Figure 1.5 A schematic presentation of the High Resolution Mirror Assembly of *Chandra* telescope. The assembly consists of four pairs of nested grazing-incidence mirrors which collect incoming X-ray photons, focusing it into a one-arcsecond circle. Credit: `http://chandra.harvard.edu/about/telescope_system.html`

ACIS FLIGHT FOCAL PLANE
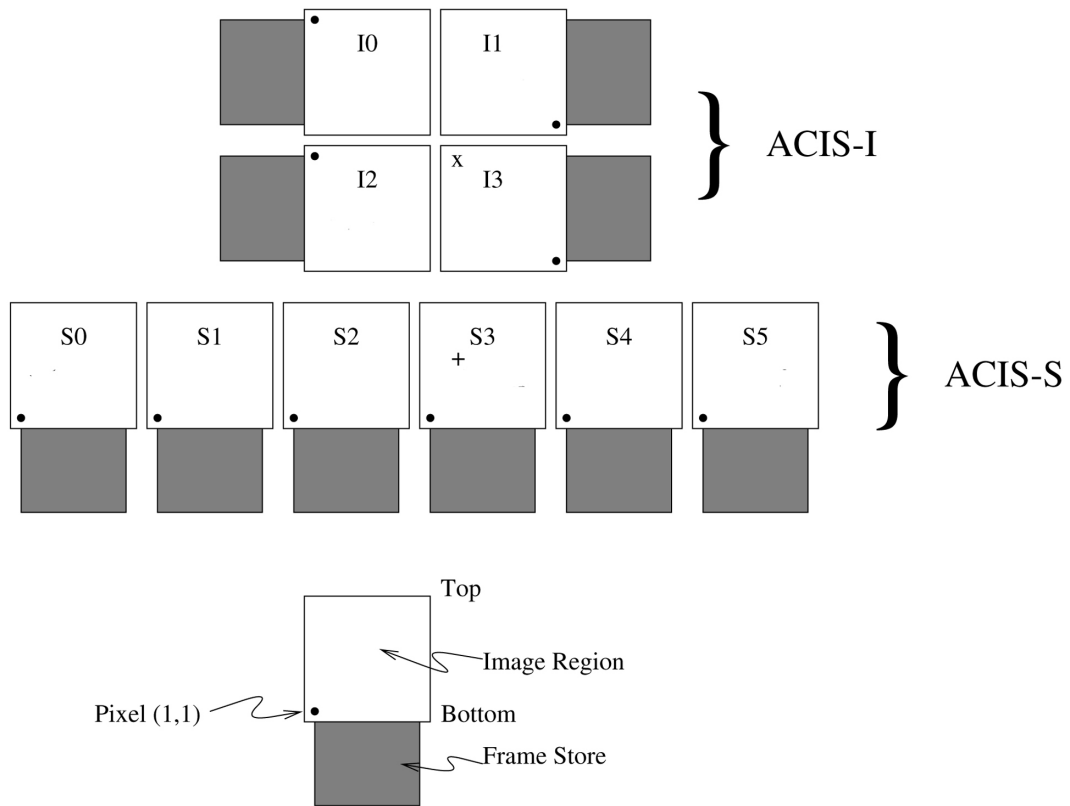
Figure 1.6 ACIS CCD schematic layout overhead view. Default aimpoints are shown for ACIS-I ('X') and ACIS-S ('+') arrays. The ACIS chips S1 and S3 are back-illuminated, while all others are front-illuminated. Credit: `http://chandra.harvard.edu/about/science_instruments.html`

CHAPTER 2

Data Analysis

2.1 Observations

We performed our *Chandra* observations of G299.2-2.9 with the ACIS-I array (Garmire et al. 2003). The observations were performed between 2010 October 26 and 2010 November 13. A total of nine ObsIDs were obtained in Very Faint mode (Table 2.1). We performed data reduction with CIAO (see Section 1.6). We did not find severe variability in the background light curve. We corrected the spatial and spectral degradation of the ACIS data caused by radiation damage, known as the charge transfer inefficiency (Townsley et al. 2000). We carried out standard data screening by status, grade, and photon energy selections. We removed "flaring" pixels and selected ASCA grades (02346). The total effective exposure is $\sim$628 ks after the data reduction. The overall X-ray emission from G299.2-2.9 is spectrally-soft with few source photons above $E \sim 3$ keV. At low energies ($E < 0.4$ keV), the source flux is negligible because of the foreground absorption, and X-ray emission is dominated by the detector background. Thus, we extracted photons between 0.4 and 3.0 keV for each ObsID in our data analysis.

2.2 Imaging Analysis

2.2.1 Three Color Image

Combining all ObsIDs, we detected $\sim$190 faint point-like sources within the ACIS-I field of view using the wavdetect script in CIAO. We removed them before any further data analysis. We present an X-ray 3-color image of G299.2-2.9 in Figure

2.1. The 3-color image reveals the detailed X-ray morphology of this supernova remnant in its entirety[1]. The 3-color image also reveals the entire morphology of the central ejecta region. The outermost angular extent of G299.2-2.9 is $\sim$13′ from east to west while that from north to south is $\sim$11′. The angular extent of the bright inner shell from north to south is $\sim$8′ and from east to west is $\sim$11′. The main part of the central ejecta region is roughly circular with an extent of $\sim$4.2′ in diameter. This central ejecta region is overall dominated by emission in the 0.72-1.4 (green) and 1.4-3.0 keV (blue) bands (Figure 2.1) whereas the 1.4-3.0 keV band emission is emphasized in the southern half of the central ejecta region. This spectrally-hard emission extends continuously from the central ejecta region to the western outermost boundary of the supernova remnant (Figure 2.1). This significantly elongated (to the west) emission feature was not detected in the previous *Chandra* study (Figure 1.4) because the ACIS-S3 (with a smaller field of view) was used there (Park et al. 2007).

2.2.2 Line Equivalent Width Images and Line Flux Ratio Distributions

We constructed line *equivalent width* (EW) images following the methods pioneered by Hwang et al. (2002). We constructed our EW images for the prominent emission lines from K-shell electron transitions in He-like Si ion and L-shell transitions in various Fe ions in lower ionization states. In Fe-L band, Fe ions in various ionization states (e.g., Fe XVI - XXIII; Liedahl et al. 1995, Foster et al. 2012) produce a complex blend of numerous emission lines. These lines are detected in the CCD spectrometer (with a moderate energy resolution) as a few broad line-like features. We selected line and continuum bandpasses for the Fe-L and Si-K spectral lines as shown in Figure 2.2. We extracted Fe-L line emission from the 0.75–1.15 keV band

---

[1]The entire G299.2-2.9 was also detected in archival *XMM-Newton* data (ObsIDs 0112890101 and 0112890201, with a total exposure of $\sim$28 ks), but these data have not been published.

with the underlying continuum from the 0.5–0.6 keV and 1.20–1.28 keV bands. We extracted Si-K line emission from the 1.78–1.93 keV band with the underlying continuum from the 1.5–1.68 keV and the 2–2.3 keV bands. We binned each image by 8×8 pixels and then adaptively smoothed them with a Gaussian $\sigma = 5''$. We estimate the underlying continuum flux by logarithmically interpolating between the images made from the higher and lower energy bandpasses of each broad line (Park et al. 2002). We subtracted the estimated continuum flux from the corresponding line emission. We divide the continuum-subtracted line emission by the estimated continuum flux to generate the EW image for each element (Figures 2.3a & 2.3b). In order to reduce the noise (due to poor photon statistics near the edge of the remnant) in the EW images we set the EW to zero where the integrated continuum flux is greater than the line flux (Park et al. 2002). These EW images help us map regions where line emission is enhanced across the supernova remnant. We note that the use of EW images is only a qualitative guide to identify line-enhanced/suppressed areas for an efficient regional spectral analysis.

The Si EW image is enhanced (relative to Fe) in the southern half of the central ejecta region. It is remarkable that this enhancement continuously extends to the outermost boundary of the supernova remnant in the west. We note that the marginally-enhanced Si EWs in the eastern outermost boundary of the supernova remnant do not represent the Si overabundance based upon our spectral model fits for those regions. These moderate Si EWs in the eastern boundary of the supernova remnant correspond to the swept-up ambient medium (with sub-solar abundances) identified by Park et al. (2007). This dense ambient medium material surrounds (in projection) the central metal-rich ejecta, except for the western outer boundary. The Fe EW is centrally enhanced and also appears to extend to the western outermost boundary of the supernova remnant. We note that due to potential contamination

from the Ne K-shell emission lines at $E \sim 0.89$ keV and $E \sim 1.05$ keV (Figure 2.5), the Fe-L EW image may not accurately map the true Fe line emission, particularly along the outer shell regions. However, the Fe EW map should be reliable in the central ejecta region as the Ne lines are negligible there (Figure 2.7; see Section 2.3.2). Similar distributions of Si and Fe line emission are evident in the Fe/(O+Mg) and Si/(O+Mg) line ratio maps (Figures 2.3c & 2.3d). In contrast to Fe and Si lines which primarily trace the metal-rich ejecta, the O and Mg lines originate mostly from the shocked ambient medium in G299.2-2.9 (see Park et al.(2007) and Section 2.3.1 for relevant discussion). These line ratio maps clearly demonstrate that Fe and Si line emission is enhanced, compared to O+Mg line emission, in the central ejecta region, and extends to the western supernova remnant boundary (Figures 2.3c & 2.3d). These Fe and Si line enhancements are anti-correlated with the broadband intensity contours which are dominated by emission from the bright swept-up shell. This anti-correlation is consistent with the ejecta origin for the enhanced Fe and Si line emission.

2.3 Spectral Analysis

2.3.1 Ambient Medium

We examined the observed X-ray spectra extracted from many sub-regions in the bright inner and faint outer shells (Figure 2.4). Each region was selected to contain ~ 5000 counts. We extract the regional spectrum from each ObsID for each of the selected regions. We extracted background spectrum from a source free area outside the outermost boundary of the supernova remnant for each ACIS-I chip. We then merged the spectra from each ObsID for each region and grouped them to secure a minimum value of 20 counts per photon energy channel. We fit each of these

background-subtracted regional spectra with an NEI plane-parallel shock model (see Section 1.7). We apply this general procedure of spectral extraction and model fits for all spectral analysis throughout this thesis.

We fit the spectrum of each of these regions, varying the abundances for O, Ne, Mg, Si, and Fe. We fixed the S, Ar, Ca and Ni abundances at the solar value because there are few counts above $E \sim 2$ keV in the observed regional spectra. We also set He, C, and N abundances at the solar value because the spectra for $E < 0.4$ keV is dominated by the detector background emission and few source counts exist. We varied the column density (N_H), electron temperature (kT), ionization timescale $(n_e t)$ and normalization parameters. We found no statistically significant variation (within statistical uncertainties) of the N_H among these regions and thus fixed it at the average value $(3.2 \times 10^{21}$ cm$^{-2})$ for all regions. These fits are statistically acceptable with $\chi_\nu^2 \sim 0.8$–1.3. We present our results in Table 2.2 and representative spectra from the bright inner and faint outer shells in Figure 2.5. For the bright inner shell, the electron temperatures are estimated to be $kT \sim 0.4$–0.7 keV with ionization timescales estimated to be $n_e t \sim 1.1$–2.7×10^{11} cm^{-3} s. The average electron temperature for the bright inner shell is $0.56^{+0.04}_{-0.03}$ keV with a corresponding average ionization timescale of $2.0^{+1.6}_{-0.7} \times 10^{11}$ cm^{-3} s. For the faint outer shell, we estimate the electron temperatures to be $kT \sim 0.5$–1.1 keV with ionization timescales of $n_e t \sim 0.3$–1.7×10^{11} cm^{-3} s. The average electron temperature for the faint outer shell is $0.68^{+0.09}_{-0.09}$ keV with a corresponding average ionization timescale of $1.0^{+1.4}_{-0.5} \times 10^{11}$ cm^{-3} s. Abundance values for both shells are consistent with each other within statistical uncertainties, having values between 0.3–1.0 (depending on elemental species). We summarize these results in Table 2.3. While abundance values for both shells are consistent, the electron temperature of the bright inner shell appears to be lower than that of the faint outer shell, although their statistical uncertainties slightly overlap. Ionization

32

timescales appear to be higher in the bright inner shell, but it is difficult to draw a firm conclusion because of large statistical uncertainties. Nonetheless, assuming a higher ionization timescale in the bright inner shell, it would suggest that it may expand into a denser ambient medium than that of the faint outer shell (see Section 3.5 for a discussion on the density of each shell). Our estimated sub-solar abundance values confirm a swept-up ambient medium for the origin of these regions as identified in Park et al. (2007).

2.3.2 Metal-Rich Ejecta Material

Our EW images show strong line enhancements from shocked Si- and Fe-rich ejecta gas extending from the central ejecta regions out to the western outermost boundary of G299.2-2.9. We select three representative regions (North, South and West) for the shocked Si- and Fe-rich ejecta gas (Figure 2.6). We perform two-component NEI plane shock model fits for these candidate ejecta regions: one for the shocked ejecta emission and the other for the emission from the superposed outer swept-up ambient medium. All model parameters (except for the normalization parameter) for the swept-up ambient medium component were fixed at the average best-fit values[2] that we present in Table 2.3. We found no statistically significant variation (within statistical uncertainties) of the normalization parameter (for the swept-up ambient medium component) among these regions and thus fixed it at the average value for all regions. We fit the shocked metal-rich ejecta component by varying the elemental abundances of O, Ne, Mg, Si, S and Fe. We also varied the electron temperature, ionization timescale and normalization parameters. We estimate the

---

[2]As the line-of-sight passes through both the faint outer and bright inner shells, we use the average values (between the bright inner and faint outer shell regions) to represent the superposed ISM emission.

electron temperature ($kT \sim 1.36$ keV) to be consistent between the three regions. The ionization timescales for these regions are $n_e t \sim 1.69$–3.13×10^{11} cm^{-3} s. All three regions show large abundance values for Si, S and Fe. The North region shows a larger Fe abundance value to those of the South and West regions. The Si-to-Fe abundance ratios to the South and West are $\sim$2, while that of the North is $\sim$1. We place upper limits for O and Ne abundance values for the North and South. These upper limits are clearly lower than the average abundance value obtained for the shells. We also place an upper limit on the Ne abundance value in the West, which is similar to those in the South and North. The O abundance value in the West shows an abundance value similar to the average value for the shell regions. These results are presented in Table 2.4.

2.4 Radial Structure

2.4.1 Structure of the Ambient Medium

Following the methods pioneered by Lee et al. (2010, 2014) we investigate the radial structure of the shocked ambient material which represents the accumulated forward shock propagation history. The southern bright and faint shells are well defined compared to other areas of the supernova remnant, making them ideal for such a study. We selected 11 thin radial regions with thicknesses of $\sim$3″-7″ for the bright inner shell and 7 regions with a $\sim$10″ thickness for the faint outer shell (each region contains $\sim$5000 counts). The regions selected for this analysis are presented in Figure 2.8. We extracted spectrum from each region and fit them with a plane shock model applying the methods described in Section 2.3.1. The observed spectrum for the bright inner shell regions might be superposed by the projected emission from the faint outer shell. To test this effect we considered the faint outer shell emission

for the background spectrum of the inner shell regional spectra. We performed two-component NEI plane shock model fits (one component for the bright inner shell and the other for the superposition of the faint outer shell). All model parameters (except the normalization) for the faint outer shell component were fixed at the average values obtained for the faint outer shell (Table 2.3). We find that the contribution from the faint outer shell component is negligible (e.g., overall flux contribution is <2%). The bright inner shell is much more luminous and thus likely dominates the observed spectrum. Thus we instead use a single-component NEI plane shock model to fit these regions. We use background regions selected from source free regions outside the supernova remnant boundary. We varied the electron temperature, ionization timescale and normalization parameters while fixing the elemental abundances to the average abundance values for the bright inner shell listed in Table 2.3. These fits are statistically acceptable with $\chi^2_\nu \sim 0.8$–1.5. We then refit the data, varying the elemental abundances. These fits did not result in significant statistical improvements over the previous fits and the best-fit abundance values were consistent with the average values for the bright inner shell. Thus, we use our fit results with the elemental abundances fixed to the mean ambient medium values to study the radial structure of the bright inner shell.

We fit the regions in the faint outer shell with a single-component NEI plane shock model. We use background regions selected from source free regions outside the supernova remnant boundary. We varied the electron temperature, ionization timescale and normalization parameters while fixing the elemental abundances to the average abundance values for the faint outer shell listed in Table 2.3. These fits are statistically acceptable with $\chi^2_\nu \sim 0.9$–1.4. We refit the data, varying the elemental abundances. These fits did not result in significant statistical improvements over the previous fits and the best-fit abundance values were consistent with the average values

for the faint outer shell. Thus, we use our fit results with the elemental abundances fixed to the mean ambient medium values to study the radial structure of the faint outer shell. We present our radial profiles of the electron temperature and *EM* for both the bright and faint shells in Figure 2.9 and their best-fit parameters in Table 2.5.

2.4.2   Structure of the Metal-Rich Ejecta Material

In order to study the detailed spatial distribution of metal-rich ejecta gas in G299.2-2.9 we performed spectral model fits for a number of thin slices of sub-regions across the entire western extent of the ejecta feature (Figure 2.10). We also performed a similar spectral analysis of the southern half of the central ejecta gas feature, covering out to the outermost boundary of the supernova remnant (Figure 2.10). For the southern direction we select regions out to the outermost boundary to clearly identify the radial extent of the ejecta gas in this direction (which appears to be limited within the bright inner shell based on the EW images), particularly in comparison to the apparently longer extended ejecta gas into the western direction. We tested for the contribution from overabundant material in each of these areas by fitting regional spectrum with the elemental abundances fixed to the average values obtained from the mean values from the spectral analysis of the outer shells (Table 2.3). We varied the electron temperature, ionization timescale and normalization parameters. In Figure 2.11 we provide χ_ν^2 radial profiles from the best-fit models. The χ_ν^2 profile to the south shows initially high χ_ν^2 values ($\sim$6–7) which drop quickly to $\sim$1.5 at $r = 2.1'$ and then remain relatively constant ($\sim$1.5) until reaching the outermost boundary at $\sim$5.7′. The χ_ν^2 radial profile to the west also shows initially high χ_ν^2 values ($\sim$6–7), which steadily decrease to $\sim$3 at $r = 2.5'$. The χ_ν^2 values remain relatively constant at $\sim$2.5-3 out to $r = 6'$, then drop to $\sim$1.5 at the outermost boundary ($r = 6.8'$).

The regions with high χ^2_ν ($\gtrsim 1.7$) show significant line emission from Si, S and Fe that cannot be fit by the average best-fit abundance values from the shell regions. High χ^2_ν values would suggest that the emission from the shocked metal-rich ejecta gas significantly contributes in the observed X-ray spectrum of these regions. We fit these regions with a two-component shock model as described in Section 2.3.2. We fit the regions where the contribution from the overabundant gas is small (i.e., χ^2_ν from the single shock model fit is $\lesssim 1.6$, Figure 2.11) with a one-component shock model in order to complete the overall picture of the abundance distribution of shocked gas. In this model we varied the O, Ne, Mg, Si, and Fe elemental abundances along with the electron temperature, ionization timescale and normalization parameters.

Based on our spectral model fits for these regions, we construct radial profiles of the best-fit Si and Fe abundances (Figure 2.12). Both the Fe and Si radial profiles in the south exhibit high abundance values ($\sim$8 solar for both Si and Fe) near the center of the supernova remnant ($r < 1.5'$). From $r \sim 1.5'$–$2'$ they decline significantly until reaching sub-solar values at $r > 2'$. We identify the transition distance ($r \sim 2'$) as the location of the CD. Toward the west both the Fe and Si abundance profiles show high abundance values ($\sim$8 solar) near the center of the remnant extending out to $r \sim 2'$. At $r \sim 2'$–$2.5'$ they decline to $\sim$4 solar. At $r \sim 2.5'$–$4.5'$ abundance values for both Fe and Si remain nearly constant ($\sim$3 and $\sim$4, respectively). From $r \sim 4.5'$– $6.8'$ the Fe abundance declines from $\sim$3 to sub-solar values, while the Si abundance declines from $\sim$4 to $\sim$1.5 solar. To the west the Fe abundance transitions to solar values at $\sim$6$'$ (unlike the Si profile). The χ^2_ν radial profile (Figure 2.11) also shows a transition from relatively high values ($>$2) to small values ($\sim$1.4) at $r \sim 6'$. Thus, we identify the CD location in the west at $r \sim 6'$. Radial profiles for the O and Ne abundances to the south (Figure 2.13) show only upper limits ($\sim$0.1–0.4 solar) near the center of the remnant. Near the CD ($r \sim 2'$–$3'$) the O and Ne abundance values

increase to mean shell values and remain constant out to the outermost boundary of the supernova remnant. The O abundance to the west shows upper limits of $\sim$0.1–0.3 for $r < 3'$, which then increases to shell like values near $r \sim 3.8'$. For $r > 3.8'$ the O abundances remain nearly constant (at the average shell like abundance value) out to the outermost boundary. Ne abundance values of the west show upper limit values (0.1–0.4) for $r < 6'$. For $r > 6'$ the Ne abundance transition to shell-like values out to the outermost boundary.

2.5   Ejecta Distribution throughout the Entire Remnant

While our Fe and Si radial abundance profiles provide information on the distribution of ejecta material to the south and west, the overall distribution of metal-rich ejecta material throughout the entire supernova remnant remains unclear. In order to determine the location of the CD with a relatively high resolution throughout the entire remnant we perform extensive spatially-resolved spectral model fits of numerous small regional spectra all over the supernova remnant. This analysis may also help us determine if other ejecta-like features exist outside of the central ejecta region and the elongation of ejecta material to the west. To effectively perform such an analysis, we adopt an adaptive mesh method to define numerous small regions for the spectral analysis. Each region in the mesh is adaptively selected to contain at least 1200 photon counts. In this way we define 1621 regions, and extract the spectrum from each individual region. We adjusted region shapes along the perimeter of the supernova remnant to better reflect the actual boundary of the supernova remnant. The regions defined by our adaptive mesh script are shown in Figure 2.14a. We note that the limited photon counts for these small regions is insufficient to accurately measure individual elemental abundances. Our intention with this analysis is to map the overabundant regions based on the overall statistics of the spectral model fits

to these small regions (see below) rather than to provide actual metal abundance distributions throughout the entire remnant.

We perform spectral model fits (using ISIS; see Section 1.6) for each region with the NEI plane shock model. We fixed all elemental abundances to the average best-fit values obtained for the shell regions (as shown in Table 2.3). We varied the electron temperature, ionization timescale and the normalization parameters. In this manner we can statistically separate regions dominated by the overabundant ejecta gas (regions with statistically poor fits) from those of the low-abundant ambient medium (regions with statistically good fits). We consider regions showing $\chi^2_\nu \gtrsim$ 1.7 to be ejecta-dominated. These regions show statistically poor fits due to the presence of strong emission lines from Fe and Si. In Figure 2.14b we show the map of the χ^2_ν distribution from our spectral model fits for all of these 1621 regions. The overabundant ejecta regions (as represented by $\chi^2_\nu \gtrsim 1.7$) dominate the central regions of the supernova remnant and extend out to the western outermost boundary. This overall spatial structure is consistent with those for the Si and Fe line enhanced regions identified by our EW images. The boundary of the overabundant ejecta regions identified by this χ^2_ν map is consistent with the location of the CD that we identified, to the south and west, based on our analysis of the abundance radial structure. For completeness we considered a range of χ^2_ν values (higher or smaller than 1.7) to identify the ejecta distribution. Selecting regions with $\chi^2_\nu \gtrsim 2$ does not affect the CD locations that we identified with $\chi^2_\nu \gtrsim 1.7$. We find that lowering our criteria (e.g., $\chi^2_\nu < 1.4$) would identify regions with sub-solar abundances as metal-rich ejecta. Based on our spectral model fits for those additional regions, we find that they are clearly low abundant ISM regions. We thus conclude that the $\chi^2_\nu \gtrsim 1.7$ reasonably represents ejecta-like regions. It is notable that there are small regions of relatively high χ^2_ν values near the eastern, northeastern, and southern outermost boundaries

beyond the bright shell (Figure 2.14b). Our two component spectral model fits (see Figure 2.15 for spectra and Figure 2.6 for region selection) for these regions (with elemental abundances varied) show relatively enhanced abundances for Fe, Si and S ($\sim$1.5-4 solar; see Table 2.6) and only upper limits for the Ne abundances. In contrast to the central ejecta region, we detect a significant O emission line in these outer regions, indicating the presence of O gas with an $\sim$solar abundance. These features are also consistent with the outer portions of the western extent of ejecta.

Table 2.1.   Our *Chandra* Observations of Galactic Supernova Remnant G299.2-2.9.

ObsId	Exposure (ks)	Start Date
11098	95.87	2010-11-02
11099	129.72	2010-11-05
11000	98.74	2010-10-26
11001	88.87	2010-10-28
13157	35.15	2010-10-30
13158	94.1	2010-10-31
13159	9.93	2010-11-11
13160	34.94	2010-10-27
13187	40.52	2010-11-13

Table 2.2.   Best-fit Spectral Parameters for the Bright and Faint Shell Regions.

Region Name	kT (keV)	O	Ne	Mg	Si	Fe	$n_e t$ (10^{11} cm^{-3} s)	χ^2/dof
Bright1	$0.55^{+0.03}_{-0.04}$	$0.51^{+0.20}_{-0.19}$	$0.77^{+0.20}_{-0.19}$	$0.50^{+0.15}_{-0.15}$	$0.52^{+0.20}_{-0.17}$	$0.55^{+0.19}_{-0.20}$	$1.57^{+1.69}_{-0.22}$	115.61/77
Bright2	$0.59^{+0.04}_{-0.03}$	$0.63^{+0.41}_{-0.20}$	$0.65^{+0.18}_{-0.14}$	$0.50^{+0.18}_{-0.13}$	$0.33^{+0.17}_{-0.12}$	$0.63^{+0.28}_{-0.17}$	$2.52^{+1.10}_{-0.84}$	83.19/76
Bright3	$0.73^{+0.06}_{-0.05}$	$0.84^{+0.67}_{-0.32}$	$0.63^{+0.24}_{-0.23}$	$0.82^{+0.35}_{-0.21}$	$0.60^{+0.30}_{-0.19}$	$1.24^{+0.60}_{-0.38}$	$1.71^{+1.20}_{-0.65}$	80.13/79
Bright4	$0.61^{+0.05}_{-0.03}$	$0.33^{+0.18}_{-0.11}$	$0.52^{+0.14}_{-0.12}$	$0.42^{+0.14}_{-0.10}$	$0.42^{+0.16}_{-0.12}$	$0.42^{+0.17}_{-0.13}$	$2.29^{+1.16}_{-0.82}$	81/79
Bright5	$0.54^{+0.03}_{-0.01}$	$0.26^{+0.26}_{-0.08}$	$0.42^{+0.14}_{-0.09}$	$0.51^{+0.21}_{-0.10}$	$0.50^{+0.29}_{-0.13}$	$0.68^{+0.46}_{-0.21}$	$2.67^{+0.90}_{-0.81}$	84.27/80
Bright6	$0.68^{+0.06}_{-0.05}$	$0.53^{+0.36}_{-0.18}$	$0.61^{+0.21}_{-0.13}$	$0.58^{+0.24}_{-0.15}$	$0.57^{+0.25}_{-0.17}$	$0.68^{+0.46}_{-0.21}$	$1.06^{+0.43}_{-0.41}$	76.65/84
Bright7	$0.54^{+0.30}_{-0.30}$	$0.38^{+0.22}_{-0.11}$	$0.53^{+0.16}_{-0.11}$	$0.49^{+0.18}_{-0.11}$	$0.42^{+0.17}_{-0.14}$	$0.54^{+0.17}_{-0.14}$	$1.91^{+1.08}_{-0.69}$	93.66/77
Bright8	$0.63^{+0.06}_{-0.04}$	$0.61^{+0.35}_{-0.20}$	$0.56^{+0.19}_{-0.13}$	$0.55^{+0.21}_{-0.15}$	$0.48^{+0.22}_{-0.17}$	$0.82^{+0.37}_{-0.25}$	$1.29^{+0.80}_{-0.52}$	71.31/77
Bright9	$0.58^{+0.02}_{-0.02}$	$0.87^{+1.67}_{-0.48}$	$0.90^{+0.89}_{-0.31}$	$0.85^{+0.78}_{-0.30}$	$0.65^{+0.53}_{-0.15}$	$1.00^{+0.96}_{-0.39}$	$4.49^{+3.01}_{-1.75}$	103.59/78
Bright10	$0.45^{+0.03}_{-0.01}$	$0.41^{+0.14}_{-0.11}$	$0.70^{+0.17}_{-0.14}$	$0.49^{+0.14}_{-0.11}$	$0.60^{+0.22}_{-0.18}$	$0.49^{+0.15}_{-0.13}$	$1.77^{+1.82}_{-0.75}$	112.21/75
Bright11	$0.44^{+0.03}_{-0.03}$	$0.39^{+0.15}_{-0.09}$	$0.61^{+0.16}_{-0.11}$	$0.42^{+0.13}_{-0.11}$	$0.42^{+0.17}_{-0.15}$	$0.50^{+0.18}_{-0.11}$	$1.80^{+1.92}_{-0.78}$	103.43/75
Bright12	$0.54^{+0.03}_{-0.034}$	$0.50^{+0.76}_{-0.18}$	$0.61^{+0.20}_{-0.12}$	$0.51^{+0.18}_{-0.13}$	$0.58^{+0.22}_{-0.17}$	$0.63^{+0.75}_{-0.22}$	$1.62^{+1.70}_{-0.51}$	91.68/74
Bright13	$0.55^{+0.03}_{-0.03}$	$0.48^{+6.20}_{-0.11}$	$0.40^{+0.10}_{-0.08}$	$0.30^{+0.81}_{-0.08}$	$0.39^{+0.13}_{-0.13}$	$0.54^{+2.81}_{-0.10}$	$1.57^{+0.51}_{-0.83}$	136.52/80
Bright14	$0.54^{+0.03}_{-0.03}$	$0.53^{+0.35}_{-0.17}$	$0.54^{+0.18}_{-0.12}$	$0.55^{+0.20}_{-0.13}$	$0.42^{+0.18}_{-0.15}$	$0.68^{+0.30}_{-0.19}$	$2.15^{+1.25}_{-0.69}$	92.59/78
Bright15	$0.48^{+0.05}_{-0.03}$	$0.55^{+0.34}_{-0.18}$	$0.89^{+0.40}_{-0.23}$	$0.98^{+0.48}_{-0.28}$	$0.95^{+0.47}_{-0.31}$	$0.91^{+0.48}_{-0.29}$	$1.63^{+1.54}_{-0.78}$	95.54/77
Faint1	$0.53^{+0.05}_{-0.04}$	$0.44^{+0.21}_{-0.16}$	$0.82^{+0.25}_{-0.21}$	$0.49^{+0.19}_{-0.15}$	$0.41^{+0.21}_{-0.18}$	$0.53^{+0.21}_{-0.20}$	$1.20^{+1.67}_{-0.39}$	102.66/74
Faint2	$0.47^{+0.06}_{-0.04}$	$0.45^{+0.29}_{-0.15}$	$0.66^{+0.27}_{-0.16}$	$0.32^{+0.20}_{-0.19}$	$0.70^{+0.38}_{-0.27}$	$0.52^{+0.31}_{-0.17}$	$1.70^{+3.54}_{-0.91}$	83.23/86
Faint3	$0.56^{+0.04}_{-0.03}$	$0.68^{+0.09}_{-0.09}$	$0.60^{+0.06}_{-0.05}$	$0.89^{+0.40}_{-0.23}$	$0.89^{+0.40}_{-0.23}$	$0.89^{+0.40}_{-0.23}$	$0.89^{+0.40}_{-0.23}$	82.41/84
Faint4	$0.95^{+0.16}_{-0.13}$	$0.80^{+0.57}_{-0.26}$	$0.78^{+0.49}_{-0.28}$	$0.53^{+0.40}_{-0.20}$	$1.56^{+1.01}_{-0.49}$	$1.12^{+0.78}_{-0.36}$	$4.97^{+3.32}_{-1.78}$	118.74/86
Faint5	$0.69^{+0.06}_{-0.06}$	$0.58^{+0.57}_{-0.19}$	$0.66^{+0.36}_{-0.15}$	$0.68^{+0.47}_{-0.16}$	$0.77^{+0.36}_{-0.23}$	$0.98^{+0.99}_{-0.22}$	$0.76^{+0.33}_{-0.33}$	84.23/78
Faint6	$0.54^{+0.04}_{-0.04}$	$0.42^{+0.28}_{-0.13}$	$0.45^{+0.15}_{-0.10}$	$0.41^{+0.17}_{-0.11}$	$0.51^{+0.25}_{-0.18}$	$0.58^{+0.32}_{-0.17}$	$1.12^{+1.19}_{-0.45}$	98.29/81
Faint7	$1.10^{+0.18}_{-0.23}$	$1.01^{+0.53}_{-0.51}$	$0.82^{+0.49}_{-0.34}$	$0.44^{+0.35}_{-0.22}$	$0.31^{+0.40}_{-0.25}$	$0.95^{+0.55}_{-0.50}$	$0.31^{+0.46}_{-0.17}$	87.69/86
Faint8	$0.58^{+0.11}_{-0.10}$	$0.55^{+1.04}_{-0.30}$	$0.99^{+1.53}_{-0.49}$	$0.63^{+1.00}_{-0.38}$	$0.84^{+1.35}_{-0.64}$	$0.83^{+1.38}_{-0.50}$	$0.81^{+2.25}_{-0.52}$	81.57/81

Note. — Uncertainties are at 90% confidence level. All abundance values are measured with respect to solar.

Table 2.3.   Average Values of Spectral Parameters for the Bright and Faint Shells.

Parameter	Bright Shell	Faint Shell	Mean Values
kT^{a} (keV)	$0.56^{+0.04}_{-0.03}$	$0.68^{+0.09}_{-0.09}$	$0.60^{+0.06}_{-0.05}$
O	$0.52^{+0.82}_{-0.18}$	$0.58^{+0.51}_{-0.24}$	$0.54^{+0.71}_{-0.20}$
Ne	$0.62^{+0.24}_{-0.15}$	$0.72^{+0.45}_{-0.24}$	$0.66^{+0.31}_{-0.18}$
Mg	$0.56^{+0.30}_{-0.14}$	$0.49^{+0.35}_{-0.18}$	$0.54^{+0.31}_{-0.17}$
Si	$0.52^{+0.24}_{-0.17}$	$0.69^{+0.53}_{-0.29}$	$0.58^{+0.34}_{-0.22}$
Fe	$0.68^{+0.54}_{-0.20}$	$0.78^{+0.62}_{-0.30}$	$0.71^{+0.57}_{-0.23}$
$n_e t^{\mathrm{a}}$ ($\times\ 10^{11}$ cm^{-3} s)	$2.00^{+1.64}_{-0.67}$	$0.98^{+1.38}_{-0.43}$	$1.64^{+0.80}_{-0.63}$

Note. — Uncertainties are at 90% confidence level.

[a]Uncertainties measured with abundances fixed at their best-fit values.

Table 2.4.   Best-fit Parameters for Characteristic Ejecta Regions.

Parameters	North	South	West
kT (keV)	$1.36^{+0.02}_{-0.07}$	$1.36^{+0.02}_{-0.15}$	$1.31^{+0.08}_{-0.16}$
O	$< 0.21^{a}$	$< 0.20^{a}$	$0.34^{+0.31}_{-0.19}$
Ne	$< 0.42^{a}$	$< 0.12^{a}$	$< 0.09^{a}$
Si	$5.77^{+6.17}_{-3.01}$	$7.53^{+3.93}_{-2.06}$	$4.17^{+2.30}_{-1.14}$
S	$15.80^{+18.47}_{-4.25}$	$18.18^{+11.15}_{-7.42}$	$5.53^{+3.92}_{-2.06}$
Fe	$6.21^{+11.93}_{-1.82}$	$3.73^{+1.18}_{-1.23}$	$2.36^{+0.92}_{-0.46}$
$n_e t$ ($\times$ 10^{10} cm^{-3} s)	$1.69^{+0.41}_{-0.63}$	$2.09^{+0.58}_{-0.25}$	$3.13^{+0.87}_{-0.53}$
χ^2/dof	93.49/75	96.47/86	114.44/99

Note. — Uncertainties are at 90% confidence level.

[a]90% upper limit.

Table 2.5.   Best-fit Parameters for the Bright and Faint Radial Shell Regions.

Region	Distance[a] (arcminute)	EM[b] (10^{55} cm^{-3})	$n_e t$[b] (10^{11} cm^{-3} s)	kT[b] (keV)	χ^2/dof
FS1	5.58	$1.17^{+0.20}_{-0.13}$	$0.38^{+0.22}_{-0.11}$	$0.68^{+0.10}_{-0.09}$	80.92/79
FS2	5.42	$1.43^{+0.22}_{-0.22}$	$0.93^{+0.42}_{-0.31}$	$0.63^{+0.09}_{-0.06}$	100.82/82
FS3	5.25	$1.42^{+0.23}_{-0.22}$	$1.10^{+0.52}_{-0.39}$	$0.62^{+0.08}_{-0.06}$	103.15/80
FS4	5.08	$1.84^{+0.25}_{-0.25}$	$1.25^{+0.49}_{-0.39}$	$0.59^{+0.06}_{-0.05}$	72.75/82
FS5	4.92	$2.04^{+0.25}_{-0.28}$	$1.37^{+0.49}_{-0.43}$	$0.57^{+0.06}_{-0.04}$	94.85/83
FS6	4.75	$2.39^{+0.35}_{-0.20}$	$1.30^{+0.48}_{-0.31}$	$0.55^{+0.03}_{-0.05}$	128.50/84
FS7	4.60	$1.82^{+0.21}_{-0.22}$	$0.70^{+0.27}_{-0.21}$	$0.63^{+0.07}_{-0.05}$	116.25/81
BS1	4.14	$2.20^{+0.27}_{-0.25}$	$1.32^{+0.48}_{-0.35}$	$0.58^{+0.05}_{-0.04}$	100.79/76
BS2	4.07	$2.42^{+0.25}_{-0.25}$	$1.88^{+0.58}_{-0.50}$	$0.57^{+0.04}_{-0.04}$	57.14/77
BS3	4.00	$3.04^{+0.33}_{-0.31}$	$3.59^{+1.10}_{-0.88}$	$0.53^{+0.04}_{-0.03}$	104.55/81
BS4	3.94	$2.57^{+0.25}_{-0.24}$	$2.90^{+0.93}_{-0.68}$	$0.58^{+0.03}_{-0.02}$	90.55/81
BS5	3.89	$2.50^{+0.23}_{-0.21}$	$4.60^{+1.71}_{-1.16}$	$0.58^{+0.03}_{-0.02}$	113.97/81
BS6	3.83	$2.89^{+0.22}_{-0.16}$	$5.78^{+1.98}_{-1.29}$	$0.57^{+0.02}_{-0.02}$	105.64/80
BS7	3.77	$2.46^{+0.20}_{-0.19}$	$6.35^{+2.80}_{-1.69}$	$0.59^{+0.02}_{-0.03}$	81.46/80
BS8	3.69	$2.50^{+0.14}_{-0.25}$	$3.68^{+0.99}_{-0.97}$	$0.59^{+0.04}_{-0.02}$	104.28/81
BS9	3.61	$2.67^{+0.12}_{-0.21}$	$4.71^{+1.23}_{-1.10}$	$0.54^{+0.02}_{-0.03}$	83.8/76
BS10	3.51	$2.73^{+0.32}_{-0.30}$	$4.22^{+1.50}_{-1.19}$	$0.54^{+0.03}_{-0.04}$	111.91/81
BS11	3.39	$2.47^{+0.22}_{-0.20}$	$6.48^{+2.98}_{-1.79}$	$0.57^{+0.02}_{-0.03}$	86.94/83

Note. — Uncertainties are at 90% confidence level. FS1–FS7 refer to regions slected for the faint outer shell. BS1–BS11 refer to regions selected for the bright inner shell

[a]Angular Distance from the center of the supernova remnant.

[b]Uncertainties measured with abundances fixed at the best-fit values.

Table 2.6.   Best-fit Parameters for Outer Ejecta Regions.

Parameters	Outer South	Outer East	Outer Northeast
kT (keV)	$0.87^{+0.20}_{-0.14}$	$0.85^{+0.11}_{-0.08}$	$1.19^{+0.09}_{-0.08}$
O	$1.50^{+0.77}_{-0.44}$	$0.99^{+0.24}_{-0.15}$	$1.27^{+0.46}_{-0.30}$
Ne	$< 0.19^{a}$	$< 0.39^{a}$	$< 0.59^{a}$
Si	$3.53^{+1.29}_{-0.84}$	$1.67^{+0.29}_{-0.23}$	$2.60^{+0.68}_{-0.49}$
S	$5.65^{+2.71}_{-2.06}$	$1.67^{+0.64}_{-0.65}$	$3.3^{+1.29}_{-1.13}$
Fe	$3.72^{+1.36}_{-0.90}$	$2.11^{+0.45}_{-0.28}$	$3.24^{+0.95}_{-0.65}$
$n_e t$ ($\times 10^{10}$ cm^{-3} s)	$10.70^{+10.40}_{-4.20}$	$8.12^{+3.01}_{-1.91}$	$5.00^{+1.04}_{-0.89}$
χ^2/dof	93.49/75	96.47/86	114.44/99

Note. — Uncertainties are at 90% confidence level.
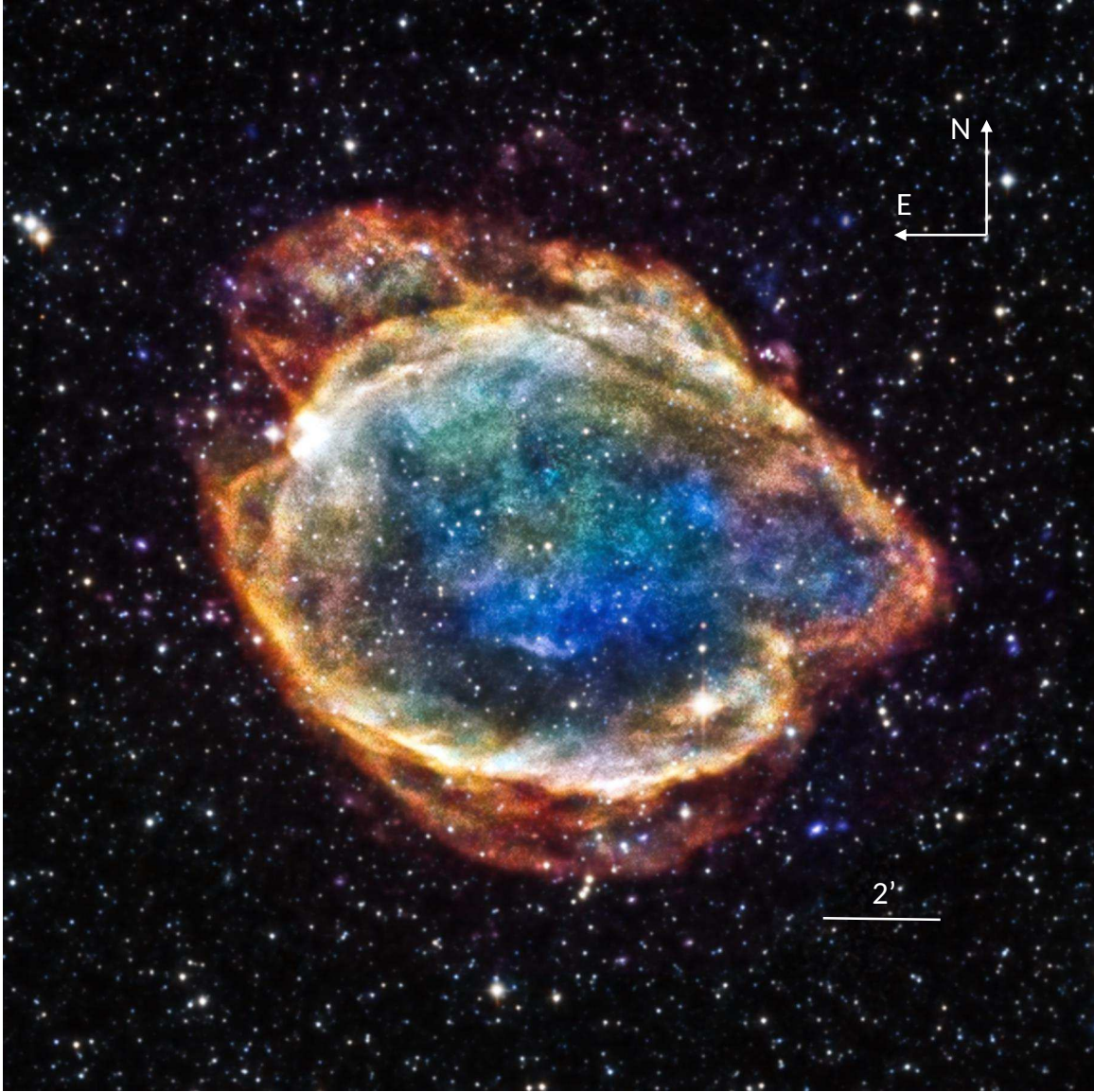
[a]90% upper limit.

Figure 2.1 An exposure-corrected 3-color image of G299.2-2.9 based on our *Chandra* data presented in Post et al. (2014). The image is a composite of *Chandra* data with *Two Micron All-Sky Survey* infrared data. Red, green, and blue represent the 0.4–0.72, 0.72–1.4, and 1.4–3.0 keV bands, respectively. Credit:http://chandra.harvard.edu/photo/2015/g299/
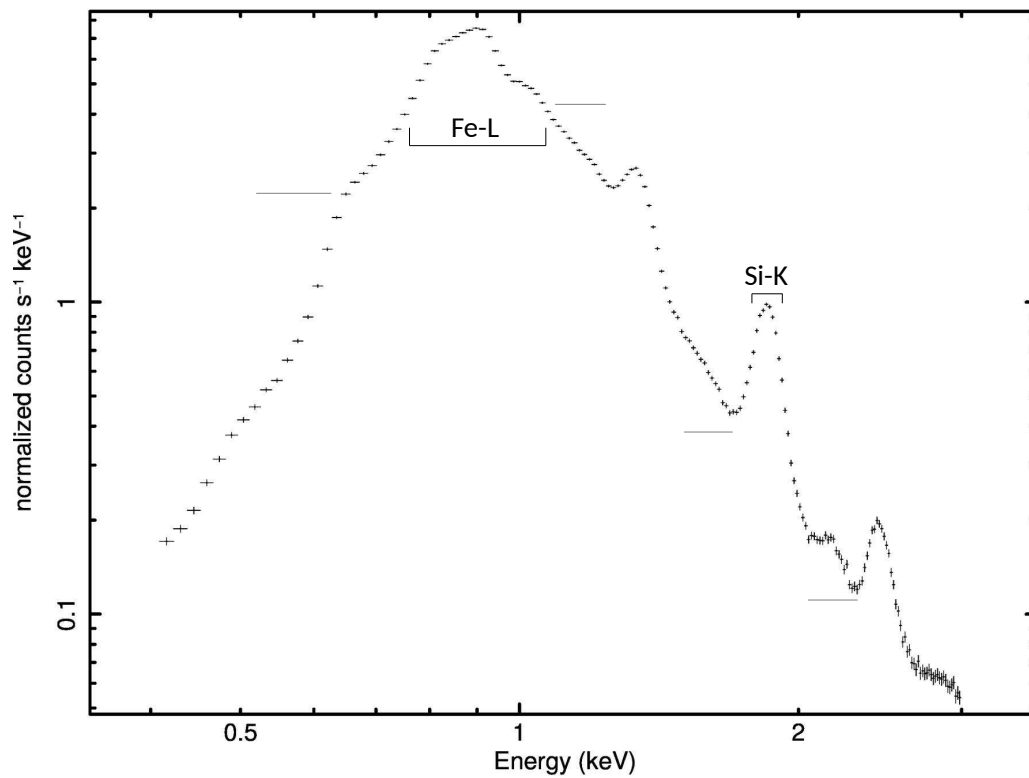
Figure 2.2 *Chandra* ACIS spectrum of G299.2-2.9. Line bands for Fe-L and Si-K elements are labeled on the plot. Horizontal lines mark the high and low continuum bands used to estimate the underlying continuum flux for the Si and Fe lines.
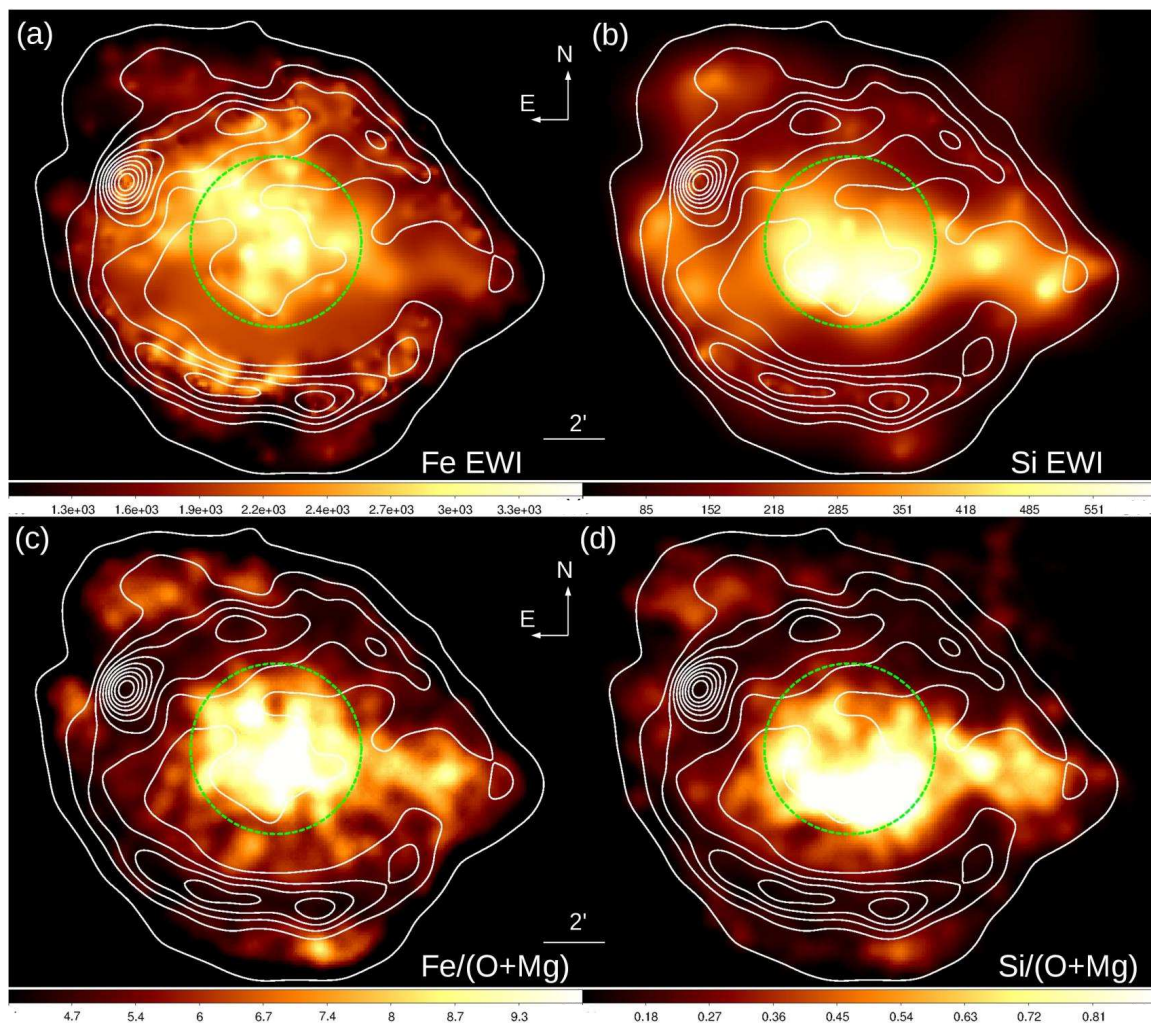
Figure 2.3 (a) Fe-L line EW image of G299.2-2.9. (b) Si line EW image of G299.2-2.9. (c) Fe (0.75–1.15 keV) to O+Mg (0.62–0.7 keV + 1.28–1.38 keV) line ratio map. (D) Si (1.78–1.93 keV) to O+Mg line ratio map. We binned all images by 8×8 pixels and then adaptively smoothed. In (a)-(d), images are overlaid with contours from the broadband image (0.4–3.0 keV) of the supernova remnant. The green circle is the location of the faint central ejecta region. credit: Post et al. (2014, Figure 2)

Figure 2.4 Broadband (0.4–3.0 keV) *Chandra* image of G299.2-2.9. This image has been exposure corrected, binned by 4 × 4 pixels and adaptively smoothed for the purposes of display. Regions for the spectral analysis to characterize the spectral properties of outer shells are overlaid.
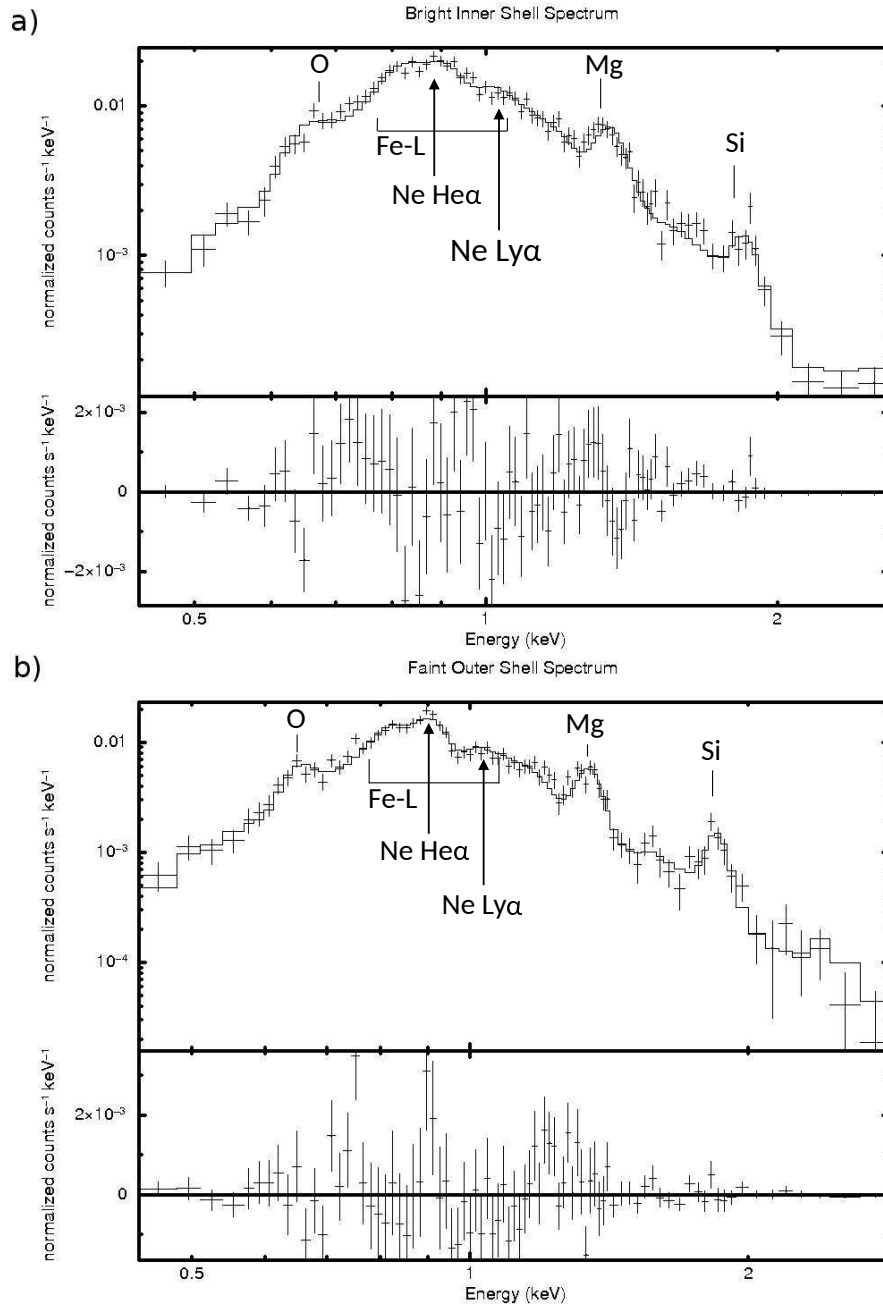
Figure 2.5 (a) Spectrum representative of the bright inner shell (b) Spectrum representative of the faint outer shell. Both spectra are overlaid with best-fit plane shock models. Residuals from the best-fit models are plotted in the bottom panel of each spectrum.
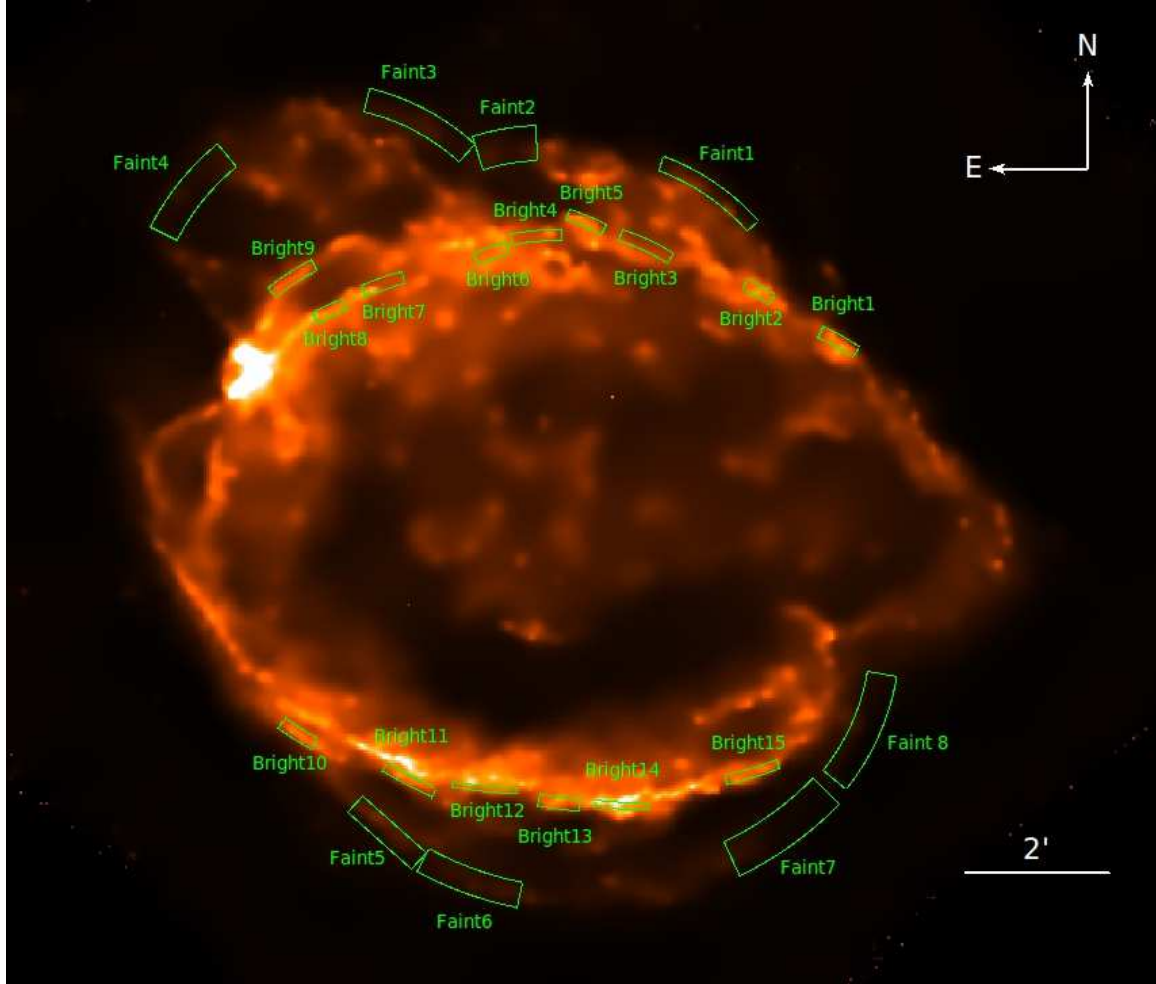
Figure 2.6 Broadband (0.4–3.0 keV) *Chandra* image of G299.2-2.9. This image has been exposure corrected, binned by 4 × 4 pixels and adaptively smoothed for the purposes of display. Regions for the spectral analysis of the representative ejecta features are overlaid.
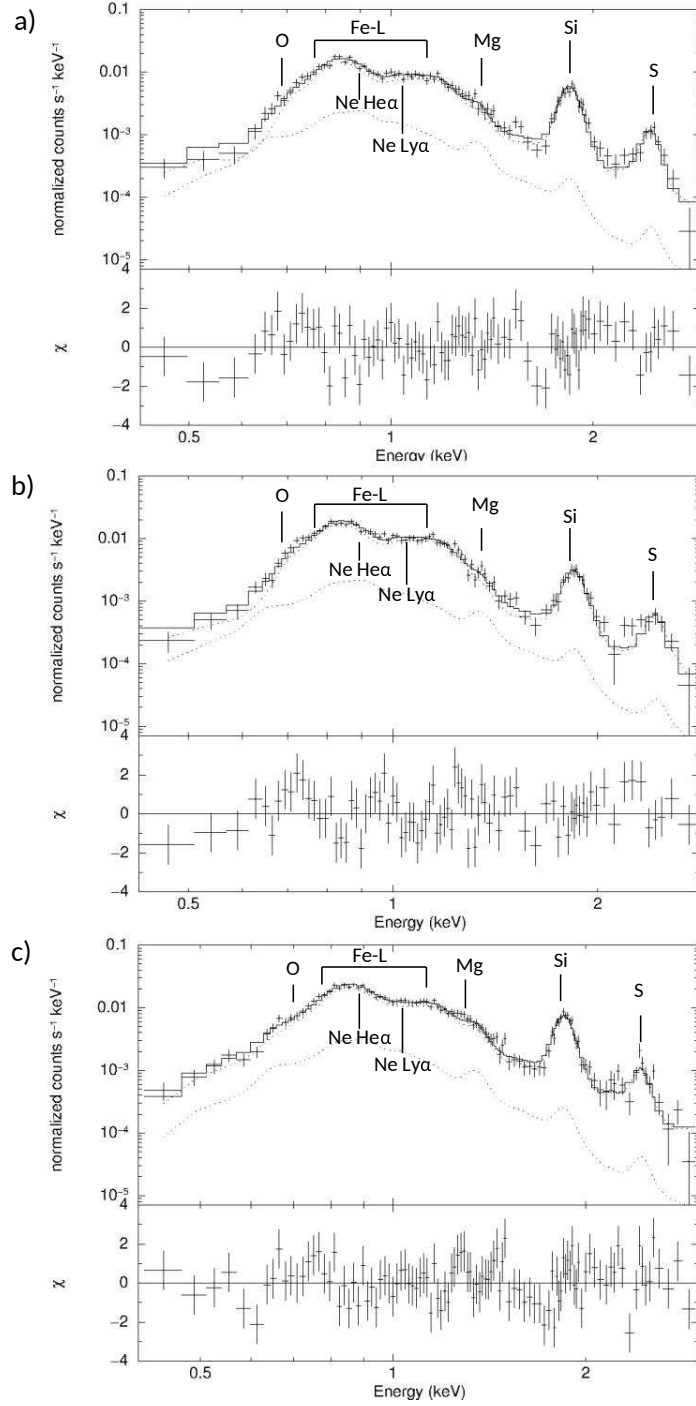
Figure 2.7 (a) Spectrum of the South. (b) Spectrum of the North. (c) Spectrum of the West. All spectra are overlaid with best-fit models (solid line). The dotted line is the contribution from the shell. Residuals from the best-fit models are plotted in the bottom panel of each spectrum.
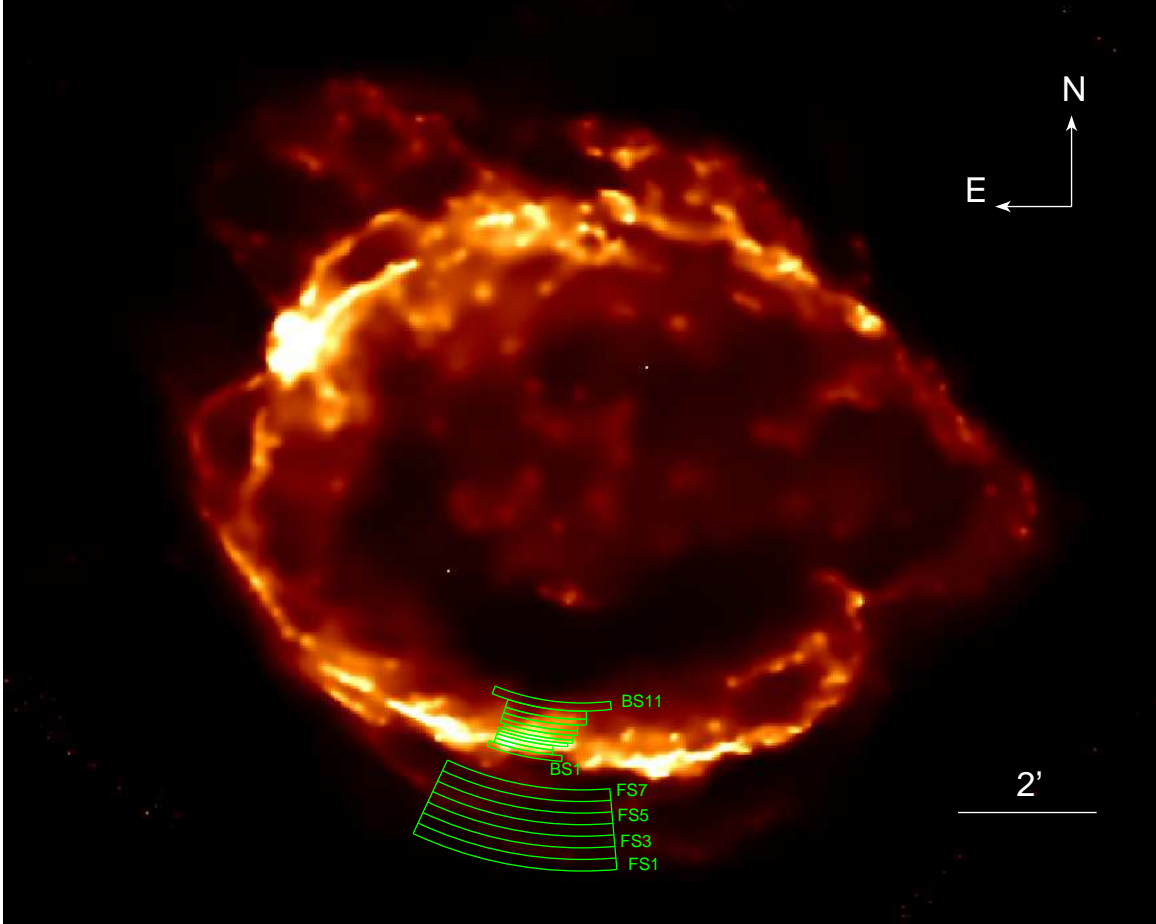
Figure 2.8 Broadband *Chandra* image of G299.2-2.9. This image has been exposure corrected, binned by 4×4 pixels and adaptively smoothed for the purposes of display. Radial spectral regions for the bright inner shell and faint outer shell are displayed.
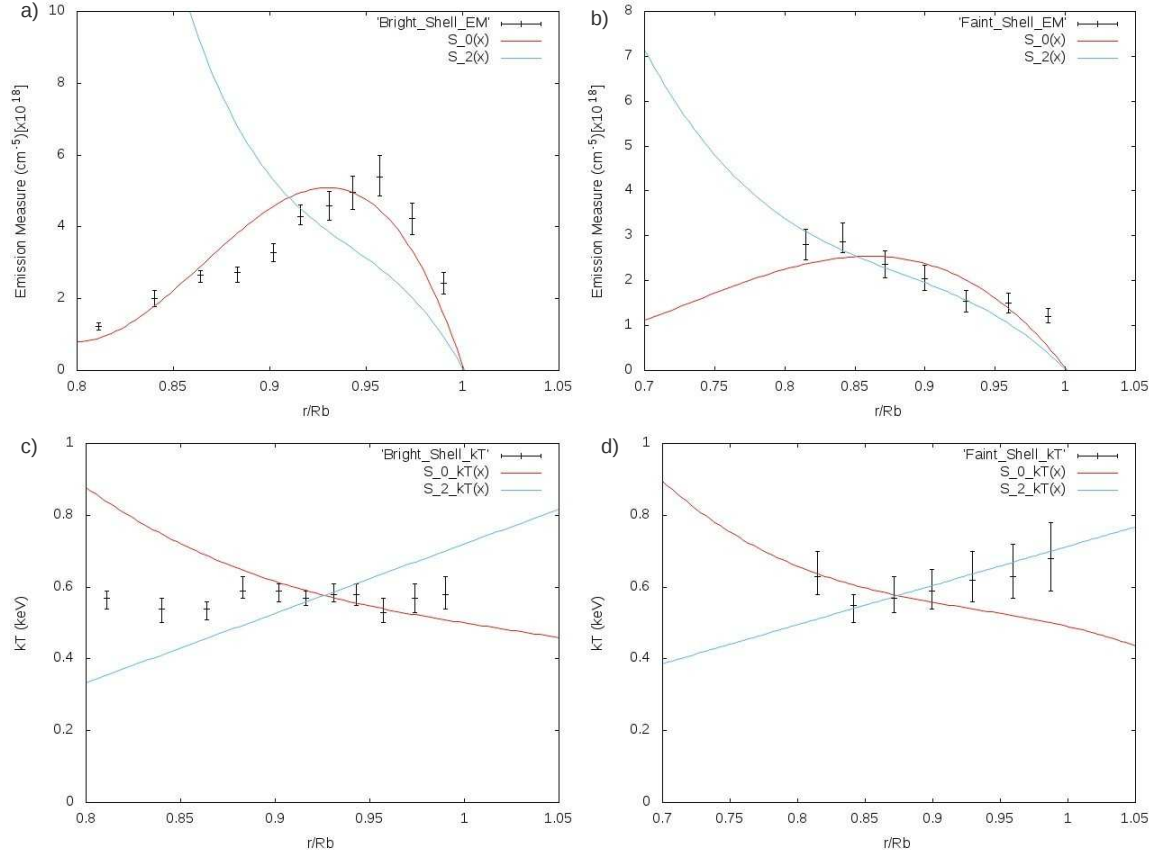
Figure 2.9 (a) The EM radial profile of the bright inner shell (b) The EM radial profile for the faint outer shell. (c) The gas temperature radial profile for the bright inner shell. (d) The gas temperature radial profile for the faint outer shell. The x-axis corresponds to the radial distance (where R_b is the distance of the forward shock from the center of the remnant). Model predictions (Chevalier 1982, Lee et al. 2010, 2014) for the uniform density (red) and wind modified (blue) ambient mediums are overlaid.
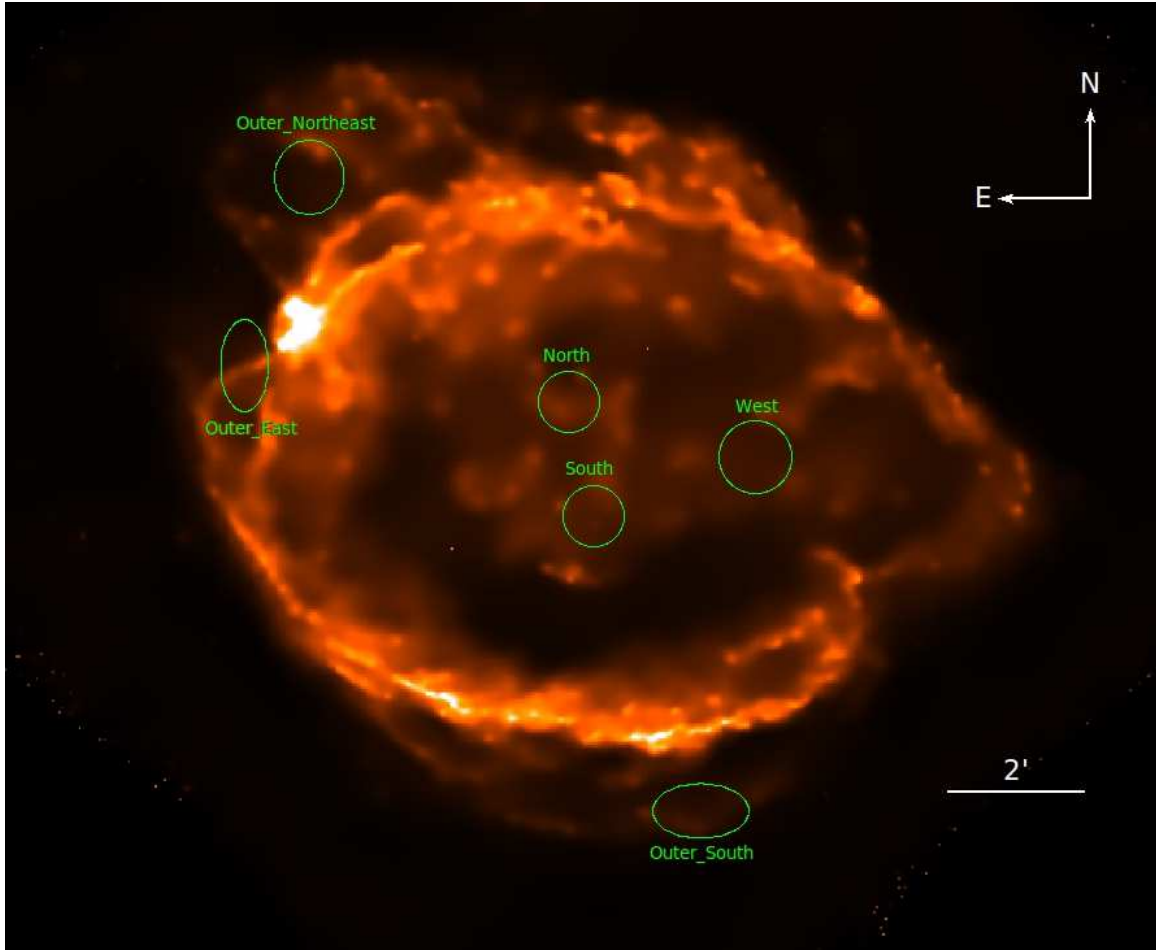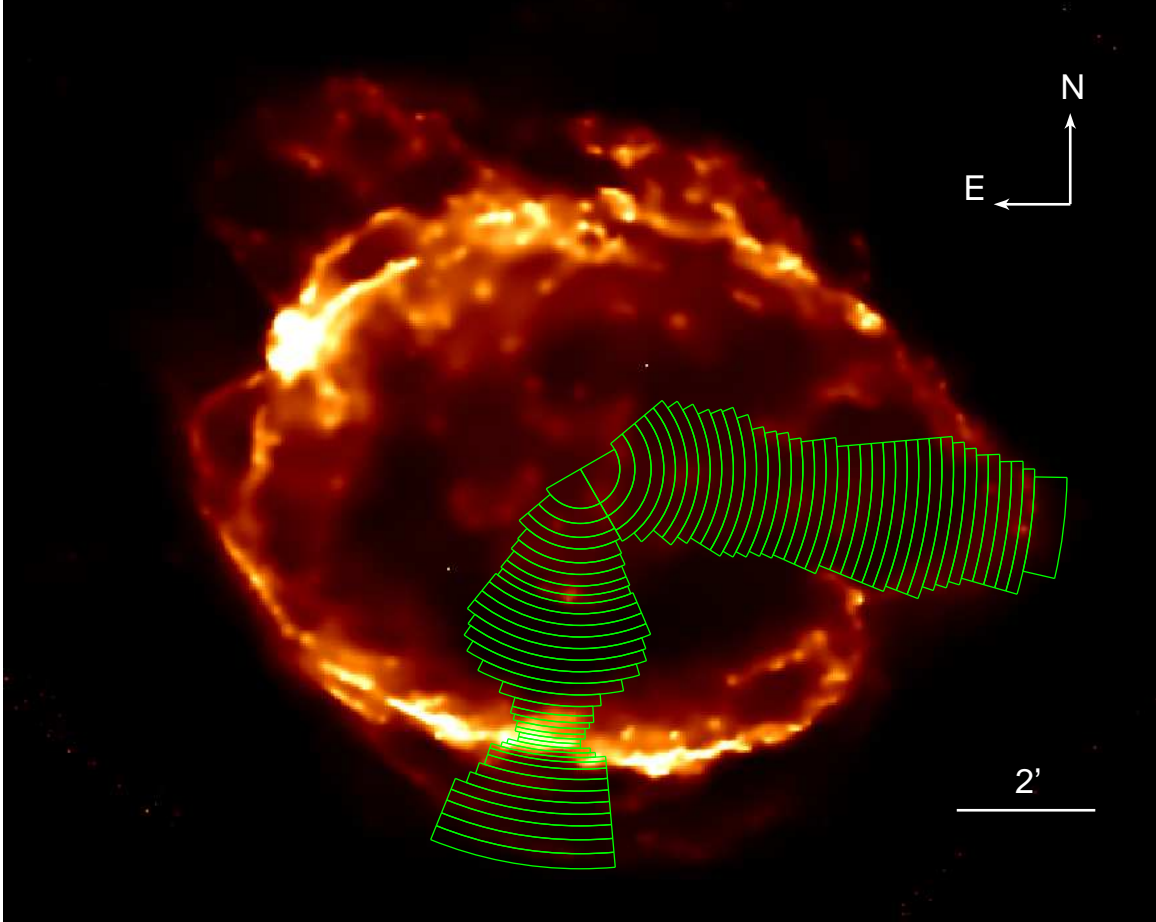
Figure 2.10 Broadband (0.4–3.0 keV) *Chandra* image of G299.2-2.9. This image has been exposure corrected, binned by 8 × 8 pixels and adaptively smoothed for the purposes of display. We overlaid the regions selected for the radial profile study of metal-rich ejecta in the south and west directions.
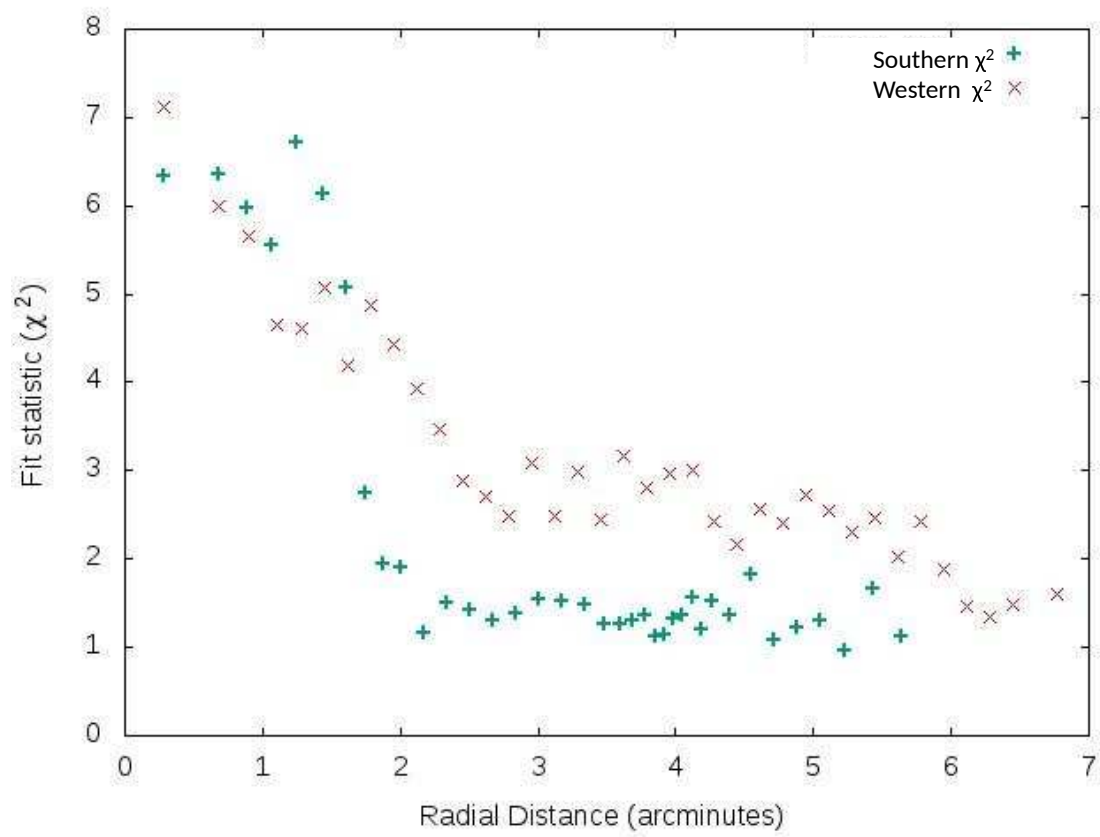
Figure 2.11 Radial profile of the best-fit χ^2_ν values for the south (blue) and west (red) radial profiles (see Figure 2.10).
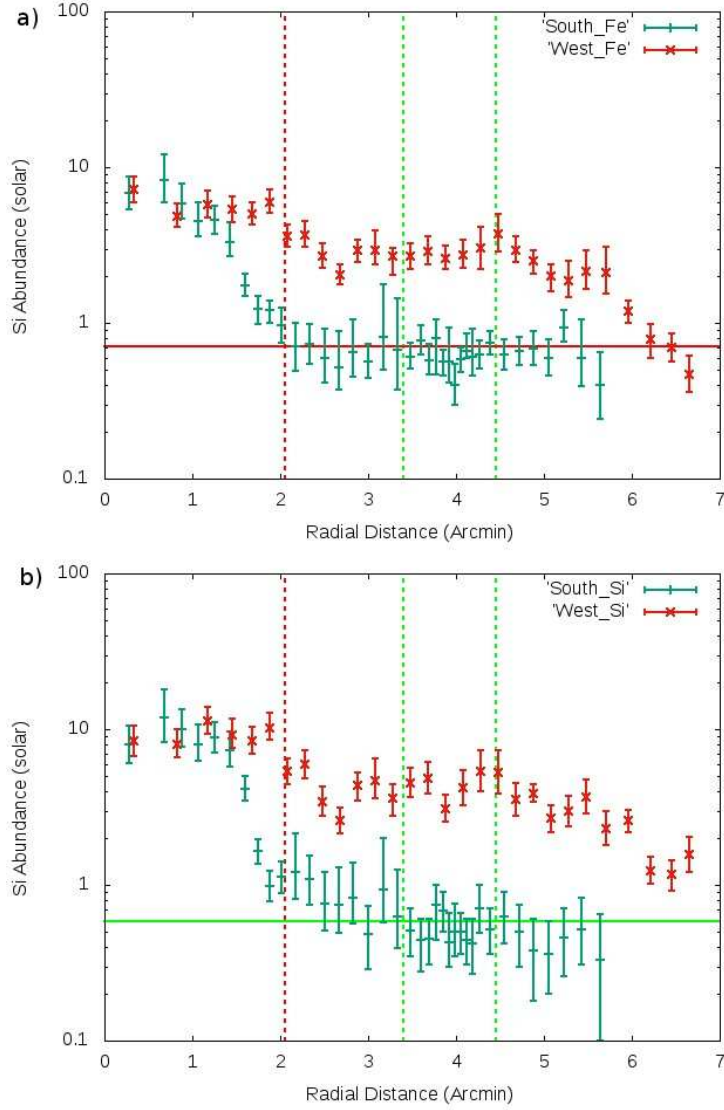
Figure 2.12 (a) Radial profiles of the Fe abundance for the south (blue) and west (red). (b) The radial profile of the Si abundance for the south (blue) and west (red). The x-axis corresponds to the radial distance from the supernova remnant center in arc minutes and the y-axis corresponds to the elemental abundance with respect to solar. The dashed red line is radial angular distance corresponding to the CD towards the south and the area between the green dashed lines represents the radial angular distances corresponding to the bright shell towards the south. The horizontal red line represents the average Fe ISM abundance value and the green horizontal line represents the average Si ISM abundance value.
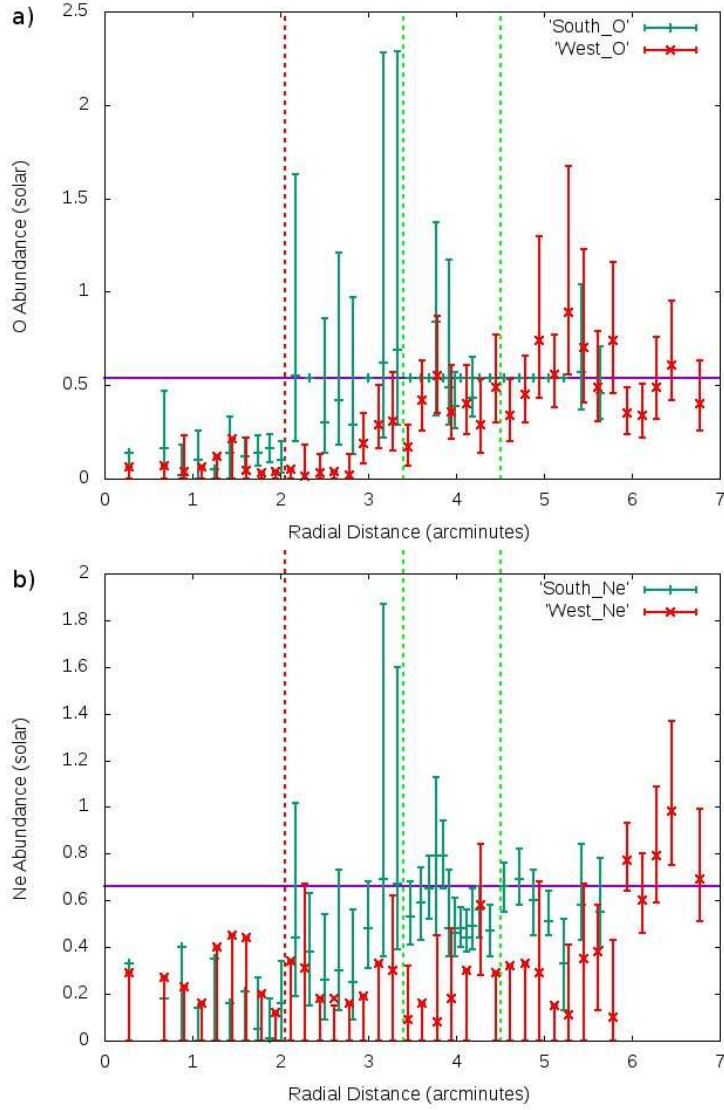
Figure 2.13 (a) Radial profiles of the O abundance for the south (blue) and west (red). (b) The radial profile of the Ne abundance for the south (blue) and west (red). The x-axis corresponds to the radial distance from the supernova remnant center in arc minutes and the y-axis corresponds to the elemental abundance with respect to solar. The dashed red line is the radial angular distance corresponding to the CD towards the south and the area between the green dashed lines represents the radial angular distances corresponding to the bright shell towards the south. The horizontal purple line represents the average ISM abundance value for the respective element.
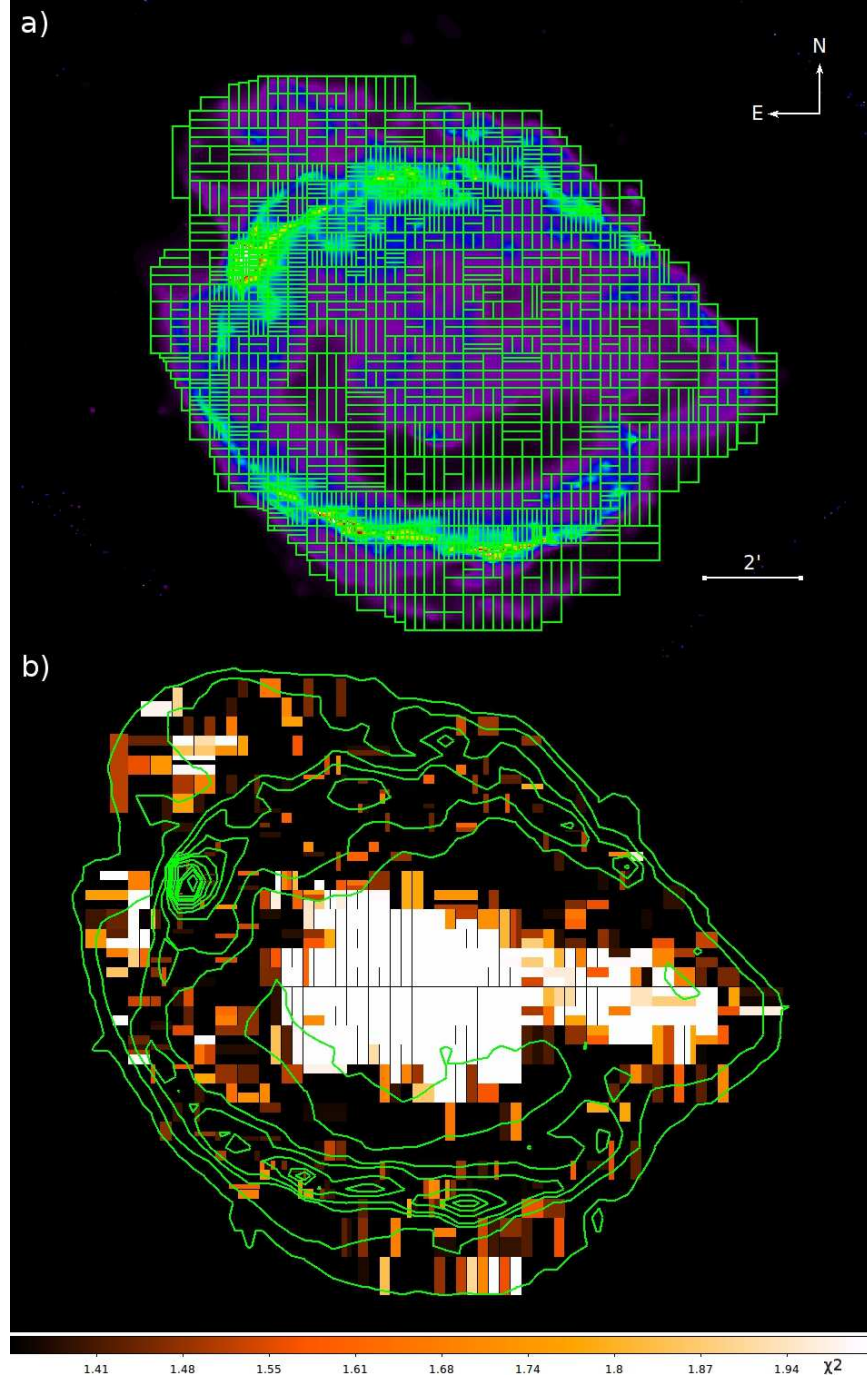
Figure 2.14 (a) Adaptively smoothed broadband (0.4–3.0 keV) image of G299.2-2.9 binned by 4×4 pixels with our adaptive mesh regions overlaid. (b) χ_ν^2 distribution map (see Section 2.5) with broadband contours overlaid.
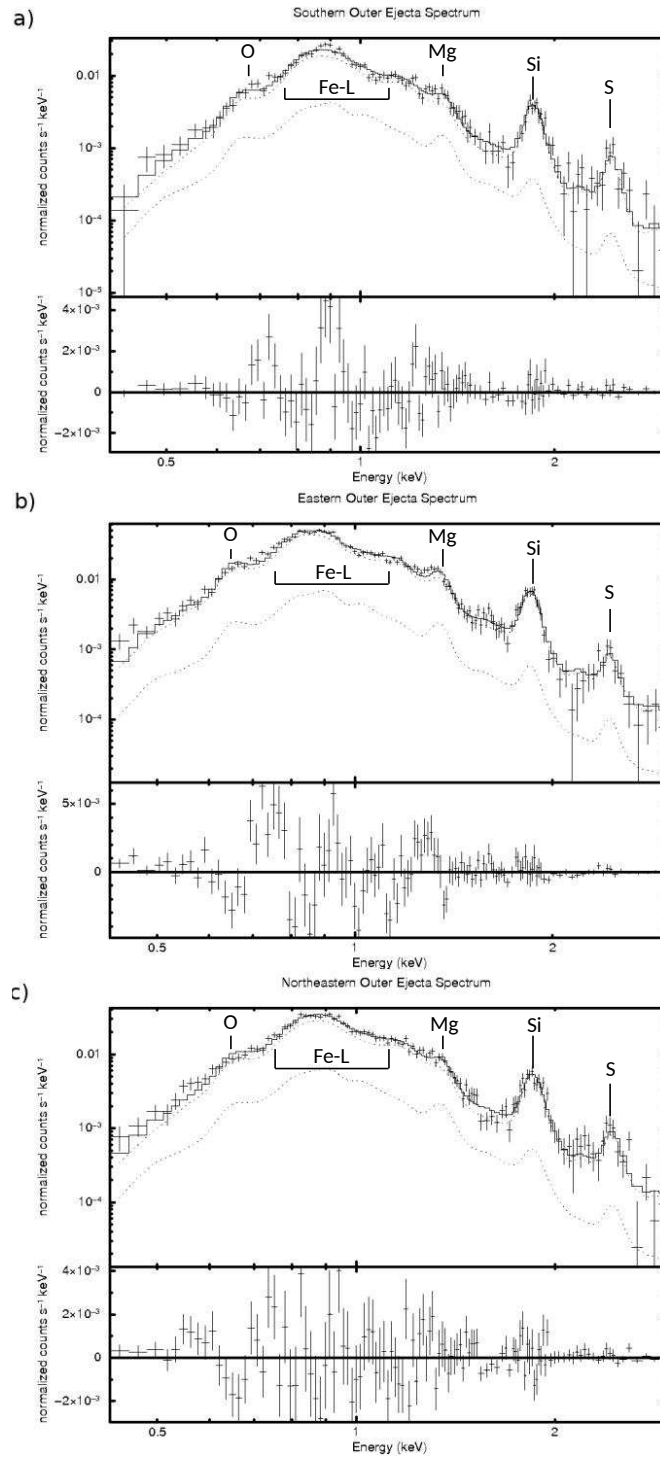
Figure 2.15 (a) Spectrum from the southern outer ejecta region. (b)Spectrum from the eastern outer ejecta region. (c) Spectrum from the northeastern outer ejecta region. Best-fit models (solid line) are overlaid on each spectrum. The dotted line is the contribution from the shell. Residuals from the best-fit models are plotted in the bottom panel of each spectrum.

61

CHAPTER 3

Discussion

3.1 Constraining The Distance To G299.2-2.9

Accurate distance estimates are critical to correctly estimate important supernova remnant characteristics such as the explosion energy, ejecta mass, and the remnant's physical scale. Initial distance estimates made by Busser et al. (1996) were not constraining ($d \sim 0.5$–9 kpc). Later works performed by Slane et al. (1996) and Bai & Wang (2000) ruled out a very nearby distance (<1 kpc) to G299.2-2.9 because it would imply an unrealistically low value ($\sim 10^{46}$ erg) for the explosion energy. They favored a relatively large distance of 5 kpc to G299.2-2.9, which corresponds to a more reasonable explosion energy. Models assuming a distance of $d \sim 5$ kpc would also better fit the observed flux and column density values. With this assumed distance they suggested that G299.2-2.9 is likely a middle-aged supernova remnant in the Sedov phase. Park et al. (2007) noted that the foreground H column density obtained from the X-ray spectral analysis, $N(\mathrm{H})_{\mathrm{X-ray}} \sim 3.5 \times 10^{21}$ cm^{-2}, is about half of the total Galactic HI column density in this direction, and thus adopted 5 kpc as the distance with a factor of ~ 2 uncertainties. While $d \sim 5$ kpc to G299.2-2.9 has been consistently suggested for the distance to G299.2-2.9 in previous works, there still remain large uncertainties involved in these estimates. It is particularly important to constrain the upper limit of the distance to G299.2-2.9 (the nearby distance being robustly rejected in previous works) in order to correctly estimate its energetics and total ejecta mass.

To better constrain the distance to G299.2-2.9, we consider the HI gas distribution along the direction to G299.2-2.9. The radio continuum emission (843 MHz) of G299.2-2.9 was observed with the Molonglo Observatory Synthesis Telescope (MOST; not published). We extracted the archival data from the Sydney University Molonglo Sky Survey (SUMSS, Bock et al. 1999). The angular resolution of the image is $45''$ $\times$ $49''$ and the rms noise is about 2.5 mJy beam^{-1}. The image suffers from interferometric artifacts within the shape of narrow fringes that crosses the field of view. Nevertheless, the ring-like structure of G299.2-2.9 is clearly detected. We also extracted a HI data cube for the region of G299.2-2.9 from the Parkes 21cm Multibeam Survey (Staveley-Smith et al.1996). The data have an angular resolution of $16'$, a velocity (v_{LSR}) coverage from -200 km s^{-1} to +200 km s^{-1} with a velocity resolution of 0.82 km s^{-1}, and an image sensitivity of about 300 mK. We use these supplementary radio data to help constrain the distance to G299.2-2.9.

The observed HI distribution in the direction to G299.2-2.9 shows a complex structures, including contributions from gas in the inner Galaxy (probably associated with the Sagittarius arm) and from the outer Galaxy. The fact that the radio continuum emission of this supernova remnant is quite faint, with an integrated flux density of only $\sim$0.5 Jy, and that the HI emission in this direction of the Galaxy is complex, hinders the use of HI data to provide an independent constraint for the distance to G299.2-2.9 through the traditional HI absorption and/or emission techniques. Instead, here we investigate the distribution of HI along the line-of-sight to constrain the distance to G299.2-2.9. In Figure 3.1 we show the HI emission line intensity profile toward G299.2$-$2.9 (centered at $(\ell, b) = (299.146°, -2.880°)$) extracted from the HI data cube. Based on the Galactic rotation curve (McClure et al. 2007), the emission at $v_{\mathrm{LSR}} < 0$ km s^{-1} in the direction of G299.2-2.9 is essentially from the HI gas inside the solar circle (the distance at which the Sun orbits the center of our

Galaxy). If we add up all the emission at $v_{\mathrm{LSR}} < 0$ km s^{-1} it corresponds to the total atomic H column density up to ∼8 kpc in this direction assuming the distance to the Galactic center $R_0 = 8.5$ kpc (International Astronomical Union [IAU] recommended value; https://www.iau.org). Then, we derive the HI column density $N(\mathrm{HI}) = 4.7^{+0.5}_{-0.5}$ × 10^{21} cm^{-2} (this HI column density is only a lower limit of the total H column density, considering the contribution from molecular H column density) up to $d \sim 8$ kpc, assuming H I spin temperature of 150 K (Liszt 1983). This $N(\mathrm{HI})$ is considerably larger than our estimates of the total H column density ($N(\mathrm{H})_{\mathrm{X-ray}} \sim 3.2^{+0.3}_{-0.4} \times 10^{21}$ cm^{-2}) toward G299.2-2.9. Thus, we consider that 8 kpc is a conservative upper limit for the distance to G299.2-2.9.

The line-of-sight to G299.2-2.9 passes through the Sagittarius arm at distance 1–2 kpc and then the outer portion of the Scutum-Centaurus arm tangentially at 4–8 kpc (Churchwell et al.2009). In Figure 3.1, most of the emission at $v_{\mathrm{LSR}} < -10$ km s^{-1} might originate in these spiral arms. (Note that it is difficult to derive N_{H} as a function of distance in the inner solar circle because of the distance ambiguity in converting the radial velocity to distance and also because of uncertainty in the Galactic rotation curve [Bovy et al. 2012]). Considering that our estimated column for G299.2-2.9 (based on our *Chandra* data) is about 70% of the total HI column density to 8 kpc, G299.2−2.9 is probably beyond the Sagittarius arm (even counting the contribution from molecular gas). Therefore, we conclude that the distance to G299.2-2.9 is ∼5 kpc with a conservative uncertainty of ≲50%.

3.2 Stellar Ejecta Material

3.2.1 Ejecta Mass

Our detailed regional spectral analysis shows nearly the entire extent of the ejecta material within the supernova remnant (Section 2.5, Figure 2.14b). However, our detailed spatially-resolved spectral analysis presented in Section 2.5 involved limited photon counts ($\lesssim$1200 counts per region), which is insufficient to accurately measure individual elemental abundances and the gas density in each region. We need to perform a similar regional spectral analysis of the ejecta region by re-formatting subregions to collect a larger number of photon counts per region ($\sim$5000 counts). For this purpose, we divide the central ejecta region into three areas (north, south, and west) based on their distinctive chemical compositions (i.e. the relatively enhanced Fe in the north; Table 2.4). We further divide each of these areas into subregions along the radial distance from the remnant's center (Figure 3.2) in order to account for any radial abundance variation that might be expected in a Type Ia explosion. We fit these individual regional spectra generally following the method described in Section 2.3.2. For each region we use the best-fit elemental abundances, along with the *EM*, to calculate each ion density. For our volume calculations we assume that the central ejecta region is represented by a spherical shell and that the reverse shock has reached the center of the remnant. We also assume that the ejecta to the west outside the central ejecta region is cylindrical in shape. We sum each elemental mass over all subregions to estimate the total mass of each element. For simplicity we assume "pure" metal (i.e., all electrons originate from each elemental ion) ejecta for the estimate of the electron density for each element. Based on the dominant ionization states of the observed spectrum, we assume electron-ion density ratios of $n_{e,Fe} = 18n_{Fe}$, $n_{e,S} = 14n_S$, $n_{e,Si} = 12n_{Si}$, $n_{e,Ne} = 9n_{Ne}$, and $n_{e,O} = 7n_O$ for Fe, S, Si, Ne, and

O respectively (these elements represent the major Type Ia nucleosynthesis products). We estimate the ion density of each element with the best-fit EM measurements (see Equation 1.5). The elemental ejecta mass can then be estimated by

$$M_{element} = A_r n_{element} m_p V. \tag{3.1}$$

In Equation 3.1 A_r is the atomic mass for the dominating isotope of an element, $n_{element}$ is the ion density of the element, m_p is the mass of a proton and V is the volume of the region. We then sum the mass estimates for each region to obtain the total mass of each ejecta element. We estimate the Fe mass of $0.17^{+0.03}_{-0.02}\ d_5^{5/2} f^{1/2}\ M_\odot$ (where f is the volume filling factor, and d_5 is the distance to G299.2-2.9 in units of 5 kpc), the Si mass of $0.09^{+0.03}_{-0.03}\ d_5^{5/2} f^{1/2}\ M_\odot$, and the S mass of $0.08^{+0.03}_{-0.03}\ d_5^{5/2} f^{1/2}\ M_\odot$. We place upper limits for the O and Ne elemental abundances, thus our measured masses for these elements ($<0.16\ d_5^{5/2} f^{1/2}\ M_\odot$ for O and $<0.05\ d_5^{5/2} f^{1/2}\ M_\odot$ for Ne) are also upper limits (see Table 3.1 for area specific results). We place an upper limit on the total ejecta mass as $\sim 0.60\ d_5^{5/2} f^{1/2}\ M_\odot$. Assuming that the bulk of the ejecta material has been reverse shock heated we may take these results as close to that of the true total elemental masses (however see Section 3.3 for further discussion). Our estimated total ejecta mass limit and total Fe mass are significantly less than canonical Type Ia supernova values (1.44 $M_\odot$ and 0.6–0.8 $M_\odot$, respectively; Branch et al. 1995). Our estimated Si mass is also lower than canonical Type Ia nucleosythesis results (0.15–0.38 $M_\odot$; Iwamoto et al. 1999). Our estimated S, and O values are generally consistent with canonical Type Ia nucleosythesis results (0.09–0.16, 0.06–0.14, respectively; Iwamoto et al. 1999). We note that our estimated ejecta masses are consistent with sub-Chandrasekhar mass models of Kromer et al. (2010) and Sim et al. (2012) (see Section 3.5). Type Ia supernova models predict negligible

production of Ne ($\lesssim 0.01$ $M_\odot$) in the supernova explosion, thus our upper limit Ne mass is consistent with Type Ia models. We note that our Ne and Si masses are consistent with nucleosynthesis results for the core-collapse of a 13 $M_\odot$ star (0.04 $M_\odot$ and 0.08 $M_\odot$, respectively; Nomoto et al. 2006). However, our estimated masses for Fe, S, and O masses are clearly inconsistent with those results for a 13 $M_\odot$ star (0.08 $M_\odot$, 0.04 $M_\odot$, and 0.22 $M_\odot$, respectively). Also, our estimated total ejecta mass is much less than 13 $M_\odot$. Thus, the core-collapse of a 13 $M_\odot$ star is clearly ruled out for the progenitor of G299.2-2.9. Our low estimated values for the Fe and total ejecta masses suggest that G299.2-2.9 was unlikely the result of a canonical Type Ia supernova. We note that there are ejecta-like features observed beyond the bright inner shell, near the eastern, northeastern and southern outermost boundaries (Figure 2.6). These possible ejecta regions do not significantly contribute to the estimated elemental masses or the total ejecta mass (~ 0.009 $M_\odot$ for the total ejecta mass).

As an independent approach we apply theoretical models of the dynamical evolution of the forward shock, reverse shock, and CD in a Type Ia supernova remnant to estimate the total ejecta mass. We adopt the method formulated by Hughes et al. (2003) based on one-dimensional dynamical evolution models for Type Ia supernova remnants developed by Truelove & Mckee (1999) and Wang & Chevalier (2001). The overall CD structure in G299.2-2.9 makes a complicated shape with a "circular" central region plus a western elongation. It may also include ejecta-like regions found near the northeastern, eastern and southern outermost boundaries. For the purposes of applying the simple one-dimensional dynamical evolutionary model for the expansion of Type Ia supernova remnants we assume that the "circular" central region represents the main CD structure. The complex multiple shell morphology of G299.2-2.9 may indicate that the remnant exploded at the boundary of two regions of differing ISM densities (see Section 3.3). In this scenario the bright inner and faint

outer shells may represent "hemispheres" of the forward shock expanding into two different densities (on average) of the ambient medium, respectively. One hemisphere would expand into the lower density medium with a higher velocity, resulting in the faint larger shell. The other hemisphere would expand into the higher density medium with a lower velocity to produce the bright smaller shell. Thus, we consider two separate cases in which each of the bright inner and faint outer shells represents the forward shock of the supernova remnant. We estimate the average radius of the forward shock to be ~4.4′ (6.5 d_5 pc; for the bright inner shell) and ~5.5′ (8 d_5 pc; for the faint outer shell). Our estimated CD has an average radius (excluding the western boundary) of ~2.1′ (3.1 d_5 pc.) The ratio of the forward shock to CD is ~2.1 for the bright inner shell and ~2.6 for the faint outer shell. In the one-dimensional dynamical evolution model for a Type Ia supernova remnant (Wang & Chevalier 2001), the forward shock radius r is related to the total ejecta mass M, the pre-shock H density n_0, and the *normalized radius* r'. Our measured forward shock to CD ratios correspond to r' (estimated from Figure 1 of Wang & Chevalier 2001) ~3.2 and ~4 for the bright inner shell and faint outer shell, respectively. This relation between r, r', M, and n_0 can be expressed in terms of the Chandrasekhar mass M_{Ch} and is independent of the explosion energy (Hughes et al. 2003), as

$$M = M_{Ch} n_0 \left(\frac{r/1pc}{2.19r'} \right)^3 . \tag{3.2}$$

Based on this relation we calculate the total ejecta mass of $M \sim 0.57\ d_5^{5/2} f^{1/2}$ M_{Ch} for the case that the bright inner shell represents the forward shock (with $r' = 3.2$, $r = 6.5\ d_5$ pc, and $n_0 = 0.71\ d_5^{-1/2} f^{-1/2}$ cm^{-3}). For the case that the faint outer shell represents the forward shock (with $r' = 4$, $r = 8\ d_5$ pc, and $n_0 = 0.24\ d_5^{-1/2} f^{-1/2}$ cm^{-3}), we calculate $M \sim 0.20\ d_5^{5/2} f^{1/2}\ M_{Ch}$.

We note that the measurements for the ejecta mass of the faint shell is not consistent with that of the bright shell. In either case our assumptions that the shell represents the complete shock front is not correct (see Section 3.3). The two very different M values we obtained may suggest that our use of the same CD size for both cases may not be valid. Part of the ejecta gas might have followed a dynamical evolution represented by the observed CD and bright inner shell while other parts (probably with a larger expansion velocity) might have followed that of the faint outer shell with a correspondingly larger and fainter (thus probably not detected in our data) CD. Thus, our assumed CD may not be adequate for the faint outer shell leading to an incorrect estimate of the total ejecta mass. In this scenario we may calculate the expected CD size associated with the faint outer shell, assuming that the ejecta mass expanding with the faint outer shell is comparable with that expanding with the bright inner shell. Based on Equation 3.2, we calculate that the radius of the CD associated with the faint outer shell would be $r \sim 5\ d_5$ pc which is $\sim 60\%$ larger than that of the observed central main ejecta region. Alternatively, an intrinsically smaller mass might have been ejected generally into the direction where the faint outer shell is expanding. In general, we may reasonably consider that the ejecta mass is somewhere between 0.20 M_{Ch} and 0.57 M_{Ch}.

At $r \sim 5\ d_5$ pc (corresponding to an angular radius of $3.4'$ from the center of the supernova remnant) the X-ray emission of G299.2-2.9 is dominated by the bright inner shell. Thus, while the presence of this larger "secondary" CD cannot be ruled out, it is difficult to find clear evidence for the presence of another CD-like feature at $r \sim 5\ d_5$ pc in our *Chandra* data of G299.2-2.9. We note that, in light of this tentative "secondary" CD, we speculate that the presence of candidate overabundant emission features extending to the northeast, east, and south beyond the bright shell as well as the outer portion of the western extent might be associated with such candidate ejecta

material expanding with higher velocities into the low density medium. Nonetheless, both direct measurements ($\lesssim 0.43\ M_{Ch}$) and dimensional analysis ($\lesssim 0.57\ M_{Ch}$) suggest that the ejecta mass of G299.2-2.9 is significantly less than the Chandrasekhar mass. These low values for the total ejecta mass is in line with our measured low value of the total Fe ejecta mass ($0.17^{+0.03}_{-0.02}\ M_\odot$).

3.2.2   Spatial Structure of the Ejecta

A significant elongation of Si- and Fe-rich ejecta continuously extends from the center of the supernova remnant out to the western outermost boundary. The central ejecta show a differential composition between the northern and southern halves. Fe to Si abundance ratios are consistent between regions located in the south and west, whereas spectrum from the North region shows a larger ratio (by a factor of $\sim$1.5–2). These non-uniform substructures of ejecta are unlike those found in other Type Ia supernova remnants with a similar age to G299.2-2.9. Lopez et al (2009, 2011) argue that the overall ejecta distribution is symmetric in most of the observed Type Ia supernova remnants. One example is DEM L71, a middle-aged Type Ia supernova remnant in the Large Magellanic Cloud, which shows a nearly circular (or somewhat elliptical) central ejecta emission feature (Hughes et al. 2003) with no observed outflows or asymmetries. The Galactic Type Ia supernova remnant G337.2-0.7 shows a complex X-ray morphology with faint emission features (probably metal-rich ejecta) surrounding the central ejecta region (Rakowski et al. 2006). Although photon statistics are limited in the data for G337.2-0.7, significant spatial variations of ejecta elements were not observed there (Rakowski et al. 2006). Although they are in a different stage of dynamical evolution, young, well-observed "canonical" Type Ia supernova remnants like Tycho or SN1006 do not exhibit similarly asymmetric ejecta

structures as seen in G299.2-2.9[1]. (The two large knots, one Fe-rich and the other Si-rich, along the southeast rim of Tycho (Vancura et al. 1995) might possibly suggest a dynamically younger stage of the ejecta elongation as we observe in G299.2-2.9, but it is only speculative.)

The central ejecta show a differential composition between the northern and southern halves. The northern half of the central ejecta nebula has an Si-to-Fe abundance ratio of $\sim$1 with a Si-to-Fe mass ratio of $\sim$0.4. The southern half of the central ejecta nebula and the western extension show an Si-to-Fe abundance ratio of $\sim$2 with a Si-to-Fe mass ratio of $\sim$0.6. This may suggest a relic structure of the nucleosynthesis from different layers of the Si-burning (Thielemann et al. 1986) during the supernova explosion. Figure 2.13b shows Ne abundances below ISM values within the entire ejecta material. This is consistent with Type Ia models which predict little Ne produces within the supernova explosion. The radial profile of the O abundance (Figure 2.13a) to the south also shows a negligible amount of the O material within the ejecta regions. The O abundance radial profile (Figure 2.13a) in the extended ejecta regions to the west shows that the O abundance increases (up to the level of the ISM values). This O abundance within the ejecta material is similar to those observed in the ejecta regions near the southern, eastern and northeastern outermost boundaries. We speculate that these O abundance values may suggest the presence of unburned O ash ejected with a high velocity from the outer layers of the progenitor[2]. Delayed-detonations and double detonations may eject unburned C and O from the formation of isolated pockets of fuel that could not be caught by the detonation front, so that they remained unburned (Bravo & Garcia-Senz 2008). Deflagration scenarios

---

[1]Mild asymmetries in the ejecta have been observed in SN 1006 (Uchida et al. 2013 and Winkler et al. 2014).

[2]We estimate $\sim 0.4\ M_\odot$ O in the outer ejecta regions and the outer portions of the western extent.

for Chandrasekhar and sub-Chandrasekhar mass white dwarfs also predict unburned C and O in the outer layers of the ejecta (Ropke et al. 2006). Large amounts of unburned C and O may be produced in the double-degenerate scenario (Pakmor 2010, 2012). However, there have been no quantitative discussions in previous works for us to compare our results with.

These structured metal-rich ejecta features in G299.2-2.9 might have been caused by an asymmetric explosion of this Type Ia supernova. Asymmetric Type Ia explosions have been suggested by a growing number of single-degenerate models in which detonations may ignite at multiple off-center positions in the progenitor (e.g., Gamezo et al, 2005; Maeda et al. 2010; Malone et al. 2014). Asymmetries are also suggested to occur in the double-detonation of single-degenerate sub-Chandrasekhar supernovae (Fink et al. 2010). Collisional double-degenerate scenarios also predict asymmetric explosions (Kushnir et al. 2013). Some Type Ia supernovae show strong line polarization, particularly for the [Ca II] and [Si II] lines, before reaching the maximum light, suggesting that portions of the ejecta are asymmetrically distributed (Wang & Wheeler 2008; Maund et al. 2010). Foley et al. (2012) found that Type Ia supernovae with blue-shifted narrow Na D profiles (an indicator of CSM interaction) tend to have higher ejecta velocities than those with no Na D absorption or those with red-shifted single or symmetric profiles. One explanation for these higher ejecta velocities is an asymmetric explosion (Foley et al. 2012). Thus, our observed asymmetrical ejecta distribution in G299.2-2.9, particularly its elongation to the western outermost boundary, might have originated from a significantly asymmetric Type Ia explosion.

Alternatively, the observed asymmetric ejecta might be the result of a spherically symmetric Type Ia explosion in a non-uniform CSM. A CSM-ejecta interaction can be considered in the context of a single-degenerate scenario in which the ambient

medium has been modified by stellar winds from the companion or progenitor, similar to that of Kepler's supernova remnant (e.g, Chiotellis et al. 2012, Patnaude et al. 2012, Burkey et al. 2013) or RCW 86 (Broersen et al. 2014). A non-uniform environment surrounding G299.2-2.9 (Park et al. 2007) would suggest that this supernova remnant may have been a remnant of the Type Ia-CSM class such as supernovae 2002ic, 2005gj, 2008J, and PTF 11kx (Hamuy et al. 2003, Aldering et al. 2006, Soker et al. 2013), in which Type Ia supernovae are interacting with dense CSM. Observations show that >20% of Type Ia supernovae may be interacting with CSM released by the progenitor system prior to the explosion (Sternberg et al. 2011, Foley et al. 2012, Maguire et al. 2013). G299.2-2.9 may belong to this relatively small population of Type Ia supernovae that interact with modified CSM. Our measured density (n_0 ~ 0.4 cm^{-3}) for the western outermost boundary is consistent with that of the faint outermost shell (see Section 3.5 for density discussion of the faint outer shell), which is significantly lower than that of the bright inner shell. Thus, the observed ejecta elongation toward the west might be due to this ambient density gradient rather than the intrinsically asymmetric explosion. However, significant ejecta emission similarly extending toward the faint outermost boundary in other directions, where the ambient density is similarly low to the western outermost boundary, is not clearly observed except for a few small ejecta-like features near the outermost boundaries in the southern, eastern, and northeastern outermost boundaries. It is unclear whether these small features are parts of continuous ejecta outflow from the remnant's center just like the western extent of the ejecta or isolated discrete ejecta "bullet"-like features similar to those detected in some other supernova remnants (e.g., Park et al. 2012, Miceli et al. 2013). Thus, it remains uncertain if the observed western elongation of the ejecta was caused entirely by this ambient density gradient. We note that planetary nebula-like bi-polar outflows from the progenitor or companion (suggested

by Tsebrenko & Soker 2013) are unlikely the cause of the observed ejecta elongation in G299.2-2.9, because such outflows would channel ejecta through a bi-polar stream as well, while G299.2-2.9 shows only a *one-sided* ejecta outflow primarily toward the west.

3.3   Nature Of The Ambient Gas

Radial profiles of the gas temperature and density behind the forward shock can provide useful diagnostics for the density structure of the medium into which the supernova shock is expanding. The utility of this method has been successfully demonstrated by Lee et al. (2010, 2014) for supernova remnants G292.0+1.8 and Cassiopeia A. We constructed *EM* and electron temperature radial profiles for the bright inner shell and faint outer shell (see Section 2.4.1 and Figure 2.9). We overlay a numerical approximation (Figure 2.9) of theoretical one-dimensional models (Chevalier 1982) of the gas temperature and the density behind the forward shock. Chevalier (1982) found self-similar solutions for the interaction of expanding ejecta material with an external ambient medium with different radial density structure,

$$\frac{\rho_2}{\rho_1} = \alpha \left(\frac{R_1}{R_c}\right)^s \left(\frac{R_2}{R_c}\right)^{-n} \left(\frac{n-3}{3-s}\right)^2 \tag{3.3}$$

$$\frac{P_2}{P_1} = \alpha \left(\frac{R_1}{R_c}\right)^{-(2-s)} \left(\frac{R_2}{R_c}\right)^{-(n-2)}. \tag{3.4}$$

In Equations 3.3 and 3.4 ρ is the mass density of the gas, R is the radius of the shock wave, P is the pressure of the gas, and α is a normalization parameter. The subscript c refers to the CD, 1 to the forward shock wave and 2 to the reverse shock. s and n are the power law indices of the density profile for the ambient medium and central metal-rich ejecta, respectively. We assumed $n = 7$, which is

appropriate for the ejecta density profile for a Type Ia supernova. We modeled both the uniform ambient density ($s = 0$) and the wind modified ambient density ($s = 2$). We overlay these models in Figure 2.9. We note that the temperature from our X-ray spectral fits is electron temperature, while the the temperature of the models are ion temperature. The electron and ion temperatures can differ significantly for non-radiative fast shocks ($v > 1000$ km s^{-1}; Ghavamian et al. 2007) in relatively young supernova remnants ($\tau <$ a few 10^3 yr). The time-averaged shock velocity for the bright inner shell (with a average shock radius and age of $r = 6.4$ pc and $\tau = 3900$ yr, respectively; see Section 3.5 for the remnant's age estimate) is $\sim$1600 km s^{-1}. For the faint outer shell (with $r = 8$ pc and $\tau = 3900$ yr) the time-averaged shock velocity is $\sim$2000 km s^{-1}. We note that the true gas temperature (or the shock velocity) can be measured by direct shock proper motion measurements or by measuring the emission line widths (usually in the optical band with a high resolution spectroscopy), both of which are unfeasible with our current X-ray data. The ratio between the electron temperature and ion temperature immediately behind the shock front varies with shock velocities (see Figure 2 in Ghavamian et al. 2007). The ratio of the electron temperature to ion temperature for shock velocities > 1500 km s^{-1} remains relatively constant and thus we assume a constant ratio between the electron temperature and ion temperature across the radius of the post-shock regions that we use in this analysis. Thus our electron temperature radial profiles should reasonably trace the overall radial distribution of actual gas ion temperature.

The *EM* radial profile (calculated by integrating the density square along the line of sight) of the bright inner shell increases (starting from the forward shock front toward the supernova remnant center), peaking near 0.96 r/R_b (Figure 2.9; where R_b is the radius of the forward shock front). After the peak the *EM* steadily drops towards the center of the supernova remnant (Figure 2.9a). Thus, the *EM* radial

profile in the bright inner shell is generally consistent with that of the shock front expanding into a uniform ambient medium. It is difficult to distinguish between a uniform and wind modified ambient medium for the faint outer shell (Figure 2.9b). The observed temperature profile for the bright inner shell remains fairly constant from the outer shock boundary towards the center of the supernova remnant (Figure 2.9c), with which it is not straightforward to discriminate the density profile of the swept-up ambient medium. The temperature profile of the faint outer shell appears to decrease towards the center of the supernova remnant (Figure 2.9d). This inward decreasing temperature radial profile may be consistent with a wind modified ambient medium. However, this interpretation is not clear due to the large statistical errors in Figure 2.9d.

We compare self-similar hydrodynamical models for the evolution of supernova remnants (Truelove and McKee 1990; Hwang and Laming 2012) with the observed overall dynamical structure (locations of the forward shock, reverse shock, and the CD) of supernova remnant G299.2-2.9. We assume a constant mass density for the central ejecta gas with an envelope with a power law profile along the radius, $\rho(r) \propto r^{-n}$, where we consider $n = 7$ for a typical Type Ia density profile. The ambient medium mass density profile is assumed to be $\rho(r) \propto r^{-s}$, where we adopt either $s = 0$ or $s = 2$ for uniform density ambient medium and for an ambient medium produced by a steady stellar wind, respectively. We present our model calculations in Figure 3.3 based on equations provided by Laming & Hwang (2002) and Hwang & Laming (2012),

$$t_0 = 5633 M_{ej}^{\frac{3}{2}} E_{51}^{-\frac{1}{2}} (\rho R_b^2)^{-1} \; yr; \; s = 2 \tag{3.5}$$

$$t_0 = 473.6 M_{ej}^{\frac{5}{6}} E_{51}^{-\frac{1}{2}} \rho^{-\frac{1}{3}} \ yr; \ s = 0 \tag{3.6}$$

$$x_0 = 40.74 M_{ej} (\rho R_b^2)^{-1} \ pc; \ s = 2 \tag{3.7}$$

$$x_0 = 3.43 M_{ej}^{\frac{1}{3}} \rho^{-\frac{1}{3}} \ pc; \ s = 0 \tag{3.8}$$

$$l_{ED} = 1.0 + \frac{8}{n^2} + \frac{0.4}{4 - s} \tag{3.9}$$

$$\phi_{ED} = (0.65 - e^{-\frac{n}{4}}) \sqrt{1 - \frac{s}{8}}. \tag{3.10}$$

In these equations, t_0 is $t_{ST}/2.024$ (where t$_{ST}$ Sedov-Taylor time from McKee & Truelove [1995]), x_0 is $x_{ST}/1.377$ (where x_{ST} is the Sedov-Taylor distance from McKee & Truelove [1995]), l_{ED} is the ratio of the radii of the forward shock to the reverse shock and ϕ_{ED} is the pressure ratio between the forward and reverse shocks. ρ is the mass density of the ambient medium, M_{ej} is the total mass of the ejecta in units of solar masses, R_b is the blast wave radius in units of pc, and E_{51} is the explosion energy in units of 10^{51} erg.

For these models we assume a distance of 5 kpc to the supernova remnant. For the total ejecta mass $M_{ej} > 0.5 \ M_\odot$, our model calculations predict that the reverse shock has not reached the center of the remnant if the bright inner shell represents the forward shock. If the reverse shock is significantly away from the renmant's center (and rather close to the CD), we would probably observe a relatively constant value of metal-rich ejecta abundances along the radius. The intensity may peak near the CD because of limb-brightening. Our abundance radial profiles for Fe and Si (Figure 2.12) show decreasing abundance values along the radius from the center of

77

the remnant out to the CD which is inconsistent with the case of the reverse shock not reaching the center of the remnant. Thus, we find that $M_{ej} > 0.5$ $M_{\odot}$ to be unlikely, and use $M_{ej} = 0.5$ $M_{\odot}$ for our hydrodynamical models. Our choice of $M_{ej} = 0.5$ $M_{\odot}$ is consistent with the ejecta masses we obtained from spectral analysis (<0.6 $M_{\odot}$; Section 3.2) and from dynamical evolutionary models (0.2–0.57 M_{Ch}; Section 3.2). We vary the explosion energy based on our estimated values from Section 3.5 (i.e., our 90% confidence level; $E_0 \sim 0.17$–0.24×10^{51} erg for the bright inner shell and $E_0 \sim 0.12$–0.20×10^{51} erg for the faint outer shell). We present our results in Figure 3.3a and Figure 3.3b. The bright inner and the faint outer shells are consistent with an expansion into an ambient medium of uniform density (solid blue line). This inferred uniform environment is generally consistent with Type Ia supernovae. The corresponding reverse shock (solid red line) for the faint outer shell has not reached the center of the remnant. We note that our observed sizes of the forward shocks and the age of G299.2-2.9 cannot be reproduced by a canonical Type Ia explosion ($M_{ej} = 1.4$ $M_{\odot}$, $E_0 = 1.0 \times 10^{51}$ erg).

G299.2-2.9 might have exploded near the boundary between two regions of different ISM densities (Park et al. 2007). In this scenario part of the forward shock encounters a density gradient and breaks out of the dense ISM into a tenuous ISM. Such a density gradient in the ambient medium would allow the forward shock to expand more quickly through the low-density medium on one side than into the denser ISM on the opposite side, which may result in a formation of a "mushroom–like" morphology (Tenorio-Tagle et al. 1985). When it is projected (face-on view) against the plane of the sky, such a morphology may be detected as a double-shell remnant. A prototype for this scenario may be the supernova remnant VRO 42.05.01 (G166.0+4.3; Pineault et al. 1987, Guo & Burrows 1997). Such a scenario can easily describe the double shell morphology of G299.2-2.9 when viewed face-on against the

plane of the sky along the line of sight. We find that the average density of the bright inner shell is ~3 times greater (see Section 3.5) than that of the faint outer shell. This suggests that the bright inner shell may be expanding into the denser ISM while the faint outer shell is expanding into a less dense environment as expected for an explosion taking place at the boundary of different ISM densities. The ejecta material expanding into the lower density medium would expand at a faster rate (than the ejecta in the higher density medium), which would have produced a larger "secondary" CD (associated with the faster forward shock corresponding to the faint outer shell) in addition to the smaller "main" CD (associated with the slower shock corresponding to the bright inner shell). We find no clear evidence for the secondary CD in G299.2-2.9. However, we note that it would be difficult to detect such a faint secondary CD because its predicted angular size would be similar to that of the bright inner shell (see Section 3.2.1). Thus, the presence of this tentative secondary CD in G299.2-2.9 cannot be ruled out.

Alternatively the complex morphology of G299.2-2.9 may be interpreted as the circumstellar structure produced by a symbiotic recurrent nova progenitor system, consisting of a red giant and a white dwarf. Red giants produce relatively cool, low velocity (up to ~ 50 km s^{-1}) massive winds with a mass loss rate up to $\sim 10^{-5}$ $M_{\odot}$ yr^{-1}. A symbiotic recurrent nova has been proposed as progenitors for some Type Ia supernovae (della Valle & Livio 1996, Hachisu & Kato 2001, Pagnota 2012, Booth et al. 2016). In this scenario the accretion disk and the equatorial wind give rise to a highly bipolar structure, which includes a dense equatorial ring (Booth et al. 2016). Mohamed et al. (2013) provide a numerical simulation of the evolution of this structure (Figure 3.4). When it is viewed face-on the resulting hourglass–like structure may produce a double (or triple) shell morphology similar to that observed in G299.2-2.9. The bright inner shell of G299.2-2.9 would be associated with the dense

equatorial ring from the accretion disk, while the faint outer shell would correspond to the bi-polar outflow. According to numerical models the density gradient between the dense equatorial ring and the bi-polar outflow would be greater than a factor of 10, which is larger than our estimates for G299.2-2.9 (see Section 3.5). Our results from both our hydrodynamical models and estimated radial profiles of EM and electron temperature suggest that the bright inner shell is expanding into a uniform ambient medium. We also do not find evidence for the presence of a red giant ex–companion star (in the optical band) near the center of the remnant as described in Section 3.4. G299.2-2.9 appears not to be the result of a recurrent nova progenitor system.

For completeness, we note that there is marginal evidence that the faint outer shell may be expanding into a modified ambient medium. The generally inward increasing EM (Figure 2.9b) and inward decreasing electron temperature (Figure 2.9d) might suggest the $s = 2$ scenario. If this is the case, the shock may be expanding into medium modified by the progenitor system. If G299.2-2.9 is truly expanding into the wind-modified CSM, it may suggest a single-degenerate or core–degenerate scenario for G299.2-2.9. Such scenarios may include the formation of bi-polar jets, steady spherical winds, and outflows from the accretion disks (Beuther et al. 2002, Kippenhahn & Weigert 2012, Patel et al. 2005). Some of these features may create asymmetric structures in the resulting supernova remnants (e.g. "ear-like" features, Tsebrenko & Soker 2013). One important caveat for this scenario is that only part of the blast wave (the faint outer shell) might be expanding into the modified CSM. It is difficult to adequately accommodate such a case. A deeper X-ray observation is necessary to clearly tell the true radial profiles of the faint outer shell.

3.4   Binary Companion Search

The presence of the surviving binary companion star would be a smoking gun to identify the nature of the progenitor system (single degenerate versus double-degenerate). We search for such a companion star in the central regions of G299.2-2.9. We assume the geometric center of the main ejecta-rich nebula (RA = $12^h14^m50.508^s$ Dec = -65°28′14.51″) as the center for our search area. We use an upper limit to the linear velocity of the ex-companion to be 270 km s^{-1} corresponding to the maximum post–explosion velocity (Pan et al. 2014) of a main sequence star (giant and sub-giant stars would have much smaller post–explosion velocities). Assuming the distance d = 5 kpc to the supernova remnant and a time since the explosion of 3900 years (see Section 3.5), the radius of our search area is ~1.4 pc, corresponding to an angular size of ~1′. We use one of the latest, most complete star catalogs available to the public, the Naval Observatory Merged Astrometric Dataset (NOMAD). We find 126 sources projected within our search area. We exclude all sources with a proper motion measurement (51 sources), because we consider these stars to be nearby field stars ($d \ll$ 5 kpc). We then removed any sources whose color index was extremely blue (<-0.4, 20 sources) or red (>2.5, 1 source), because they are not associated with any known star classification and are likely background galaxies. We also exclude point sources whose color index and absolute magnitude (assuming a distance of $d \sim$ 5 kpc) do not correspond to any star on the main sequence, sub-giant and giant branches (white dwarfs are too faint to be seen at that distance). We removed any red giant stars with an angular distance of >8″ from the center of our search, which corresponds to a post–explosion linear velocity of >50 km s^{-1} (assuming the maximum velocity achievable by red giants post–explosion; Pan et al. 2014). There are another 25 sources that do not have both a measured B and R magnitudes. These 25 sources may also be candidates for the ex-companion, but we were unable to estimate their

physical parameters (Table 3.2). We are then left with 18 ex-companion candidates as shown in Table 3.2. More detailed optical observations are needed to determine their radial velocities and spectral characteristics in order to test their candidacy for the ex-companion.

3.5   Progenitor Scenarios

To estimate the explosion energy and the age of the supernova remnant, we apply self-similar Sedov solutions. For these purposes we assume that each of the bright inner and faint outer shells represents different parts of the forward shock (expanding into different ambient densities; see Section 3.3). Based on our results presented in Section 2.3.1, we estimate the pre-shock proton density n_0 for each shell. We assume that the post-shock density ratio $n_e = 1.2 n_H$ for a mean charge state with normal composition and $n_H = 4 n_0$ for the strong shock. For our volume estimates we assume that the path lengths through each region of the shells along the line of sight is similar to the physical scales corresponding to their angular widths. For the bright inner shell regions our measured EM values indicate pre-shock densities of $n_0 \sim (0.5\text{--}0.9)$ $d_5^{-1/2} f^{-1/2}$ cm^{-3}, with an average value of $n_0 = 0.71^{+0.04}_{-0.03}$ $d_5^{-1/2} f^{-1/2}$ cm^{-3}. For the faint outer shell we estimate pre-shock densities of $n_0 \sim (0.13\text{--}0.40)$ $d_5^{-1/2} f^{-1/2}$ cm^{-3} and an average density of $n_0 = 0.24^{+0.02}_{-0.01}$ $d_5^{-1/2} f^{-1/2}$ cm^{-3}. We note that our pre-shock density values are approximately a factor of 2 greater than those obtained by Park et al. (2007). This may be due to differences in our volume estimates. With improved photon counts from our deep *Chandra* observation we are able to extract X-ray spectra from smaller regions for the bright inner and faint outer shells (thus smaller path lengths for estimating the emitting volumes) than Park et al (2007). Our smaller volume estimates would correspond to larger EM estimates. Using Equation 1.2 we estimate the Sedov ages for the bright inner shell

($t_s \sim 3600^{+130}_{-150}$ d_5 yr) and the faint outer shell ($t_s \sim 4100^{+310}_{-280}$ d_5 yr). These results are generally consistent between the two shell structures, thus we take the average value ($\sim$3900 yr) for the Sedov age of the remnants. We estimate the explosion energy with Equation 1.1. Our estimated explosion energies are $E_0 \sim 2.00^{+0.38}_{-0.30} \times 10^{50}$ $d_5^{5/2} f^{-1/2}$ erg for the bright shell and $E_0 \sim 1.54^{+0.43}_{-0.33} \times 10^{50}$ $d_5^{5/2} f^{-1/2}$ erg for the faint shell. The estimated explosion energies between the bright inner and faint outer shells are consistent (within statistical uncertainties) with each other. Thus, we adopt the average value ($1.77^{+0.40}_{-0.32} \times 10^{50}$ erg) for the explosion energy of G299.2-2.9. Our estimated values for the explosion energy are generally consistent with the values obtained by Park et al. (2007).

Our estimated low explosion energy, coupled with the relatively small total ejecta and Fe masses may suggest a double detonation of a sub-Chandrasekhar mass white dwarf. Fink et al. (2010) performed hydrodynamic simulations predicting that the explosion of a CO white dwarf with a mass of $\sim$0.8 $M_\odot$ and a He-shell of $\sim$0.1 $M_\odot$ may produce an underluminous Type Ia supernova. It has also been shown that secondary detonations in sub–Chandrasekhar mass white dwarfs can be produced for CO cores with masses as low as 0.55 $M_\odot$ (Livne & Arnett 1995). Sim et al. (2012) produced 2D simulations of the double-detonation of sub–Chandrasekhar mass white dwarf for CO cores of 0.45 and 0.58 $M_\odot$ with 0.21 $M_\odot$ He-shells. In particular their CSDD-S model produces Fe, Si and O mass estimates similar to what we measured in G299.2-2.9. Our estimated masses for Fe, and S are also consistent with nucleosynthesis results from Kromer et al. (2010) for a 0.81 $M_\odot$ CO core with a 0.13 $M_\odot$ He-shell. Our estimated upper limit for the O mass is also consistent with Kromer et al. (2010). Also, several models for this scenario showed (Fink et al. 2010, Kromer et al. 2010, Maeda et al. 2010, Chamulak et al. 2012) asymmetry in the ejecta structure. In particular, the models by Maeda et al. (2010) and Chamulak

83

et al. (2012) show Si ejected at significantly high velocities on the side opposite the detonation, which results in significant one-sided asymmetry in the ejecta structure.

Alternatively, G299.2-2.9 may have been a 2002cx-like supernova event. 2002cx-like supernovae are characterized by low total ejecta masses (Foley et al. 2013; $\sim$0.2–1.4 $M_\odot$ with an average of 0.5 $M_\odot$), low ^{56}Ni masses (Foley et al. 2013; 0.003–0.27 $M_\odot$), strong mixing of the ejecta (Jha et al. 2006), and weak absorption lines from intermediate mass elements (Branch et al. 2004). It has been proposed that 2002cx-like supernova events are a variant of the single-degenerate scenario in which the deflagration is too weak to unbind the star and a detonation does not ensue (Jordan et al. 2012). Such "failed" deflagrations (also known as Type Iax; Foley et al. 2013) may leave behind a bound remnant of the original white dwarf. Estimates for our total ejecta mass, Fe mass, and explosion energy are in good agreement with the those of the N10def model from Fink et al. (2014) and also three models from Long et al. (2014). We were unable to compare our mass estimates of O, Si, S and Ne with these models as they do not include detailed nucleosynthesis results for these elements. We note that our estimated Si mass is below canonical Type Ia nucleosynthesis results (Section 3.2), and thus it may be consistent with the weak absorption lines from intermediate mass elements observed in 2002cx-like events. These "failed" deflagration explosions may produce relatively strong asymmetries in the ejecta (Jordan et al. 2012, Fink et al. 2014). These asymmetries, especially for models with fewer ignition points, show one-sided asymmetry in the ejecta structure of the supernova.

G299.2-2.9 unlikely originates from a canonical single-degenerate or double-degenerate progenitor system. In order to achieve an explosion energy similar to the canonical value the remnant must be located past ($\sim$9 kpc) our new conservative upper limit (8 kpc; Section 3.1) for the distance to G299.2-2.9. Also the estimated

ejecta mass for that distance would scale to be $\sim$3–5 $M_\odot$, which is unrealistically large for a Type Ia supernova progenitor white dwarf.

Shock fronts within supernova remnants may accelerate the ambient particles to cosmic ray energies through the process of diffusive shock acceleration. A significant portion of the supernova energy may be lost in this process which could modify the the hydrodynamical evolution of the supernova remnant (Castro et al. 2011). This process may explain our low estimated energy for G299.2-2.9. In order to explain G299.2-2.9 the majority ($\sim$65%, see Figure 2 in Castro et al. [2011]) of the explosion energy would have been deposited into the acceleration of cosmic rays. However, our estimated low total Fe ejecta mass cannot be described by this scenario, but is consistent with a low explosion energy for the progenitor.

Table 3.1.　Mass estimates for various elements at 5 kpc.

Element	South	West	North	Total
Fe	$0.056^{+0.008}_{-0.005}$	$0.050^{+0.008}_{-0.006}$	$0.061^{+0.013}_{-0.007}$	$0.17^{+0.03}_{-0.03}$
S	$0.032^{+0.007}_{-0.007}$	$0.029^{+0.007}_{-0.007}$	$0.024^{+0.002}_{-0.002}$	$0.08^{+0.03}_{-0.03}$
Si	$0.034^{+0.005}_{-0.004}$	$0.031^{+0.005}_{-0.004}$	$0.028^{+0.005}_{-0.004}$	$0.09^{+0.03}_{-0.03}$
Ne	<0.016	<0.014	<0.024	<0.05
O	<0.052	$0.04^{+0.01}_{-0.02}$	<0.066	<0.16

Note. — Ne and O masses are upper limits. All masses are in units of $M_{\odot}$.

Table 3.2.   Candidate Ex-Companion Stars for the Progenitor of G299.2-2.9

NOMAD ID	RA	Dec	Angular Offset	B	R	V	J	H	K
	hh:mm:ss.ss	dd:mm:ss.s	arcminute	mag	mag	mag	mag	mag	mag
0245-0298549	12 14 50.599	-65 28 44.86	0.117		17.63				
0245-0298585	12 14 51.272	-65 28 58.06	0.130	16.73	14.45	15.98	9.502	8.416	7.977
0245-0298465	12 14 48.996	-65 28 55.46	0.168	20.63	18.52				
0245-0298623	12 14 52.122	-65 28 49.79	0.171	19.2					
0245-0298520	12 14 50.027	-65 28 41.86	0.174	19.24	18.53				
0245-0298458	12 14 48.859	-65 28 55.70	0.183		18.12				
0245-0298631	12 14 52.342	-65 28 50.01	0.193	18.27					
0245-0298625	12 14 52.142	-65 28 45.60	0.199	19.09					
0245-0298438	12 14 48.484	-65 28 54.01	0.213	17.13	16.56		15.429	15.303	15.013
0245-0298556	12 14 50.787	-65 29 05.07	0.221	16.31	16.06	15.81	14.252	13.692	13.473
0245-0298619	12 14 52.091	-65 29 01.54	0.230	16.66	15.8	16.84	15.31	14.768	12.41
0245-0298429	12 14 48.313	-65 28 54.30	0.231		16.1				
0245-0298424	12 14 48.263	-65 28 35.78	0.355		18.49				
0245-0298336	12 14 46.574	-65 28 50.05	0.409				16.245	15.166	15.291
0245-0298334	12 14 46.561	-65 28 43.99	0.430		21				
0245-0298587	12 14 51.304	-65 28 26.34	0.433		18.27				
0245-0298595	12 14 51.396	-65 28 25.89	0.443		19.1				
0245-0298320	12 14 46.358	-65 29 02.32	0.464		17.53				
0245-0298662	12 14 52.993	-65 28 28.36	0.469		18.2				
0245-0298310	12 14 46.095	-65 28 42.90	0.482		21				
0245-0298460	12 14 48.873	-65 29 19.38	0.489	25					
0245-0298395	12 14 47.475	-65 28 28.10	0.506		18.49				
0245-0298414	12 14 47.925	-65 29 17.99	0.511	17.5	16.21		14.944	14.877	14.292
0245-0298590	12 14 51.350	-65 28 21.14	0.520	20.33	18.75				
0245-0298366	12 14 46.971	-65 28 29.03	0.529	17.36	17				
0245-0298785	12 14 55.329	-65 29 02.71	0.532	16.51	15.63				
0245-0298419	12 14 48.153	-65 29 20.28	0.533	13.41					
0245-0298448	12 14 48.681	-65 29 22.08	0.538	19.88					
0245-0298350	12 14 46.825	-65 28 28.60	0.544	17.74	17.34				
0245-0298285	12 14 45.415	-65 28 43.65	0.546		25				

Table 3.2 (cont'd)

| NOMAD ID | RA | Dec | Angular Offset | B | R | V | J | H | K |
	hh:mm:ss.ss	dd:mm:ss.s	arcminute	mag	mag	mag	mag	mag	mag
0245-0298797	12 14 55.647	-65 29 01.95	0.559		18.52				
0245-0298810	12 14 55.999	-65 28 45.02	0.581	17.08	16.33		15.663	15.327	15.019
0245-0298817	12 14 56.245	-65 28 58.00	0.604		18.72				
0245-0298811	12 14 56.041	-65 28 39.82	0.608	15.3	14.03	15.14	14.516	14.207	14.288
0245-0298415	12 14 48.016	-65 28 18.78	0.609		19.28				
0245-0298526	12 14 50.199	-65 29 28.39	0.610	17.29	16.82				
0245-0298815	12 14 56.141	-65 28 40.70	0.613		15.55				
0245-0298475	12 14 49.186	-65 28 15.07	0.629	16.9	16.26				
0245-0298580	12 14 51.179	-65 29 30.64	0.650				14.576	15.352	13.97
0245-0298277	12 14 45.220	-65 28 30.35	0.656	17.86	17.53		15.869	15.534	15.432
0245-0298720	12 14 54.059	-65 28 18.62	0.666	17.31					
0245-0298732	12 14 54.293	-65 28 19.52	0.667	18.32	17.68				
0245-0298554	12 14 50.708	-65 29 32.43	0.676	15.31	15.16	15.2	13.906	13.819	13.426

Note. —

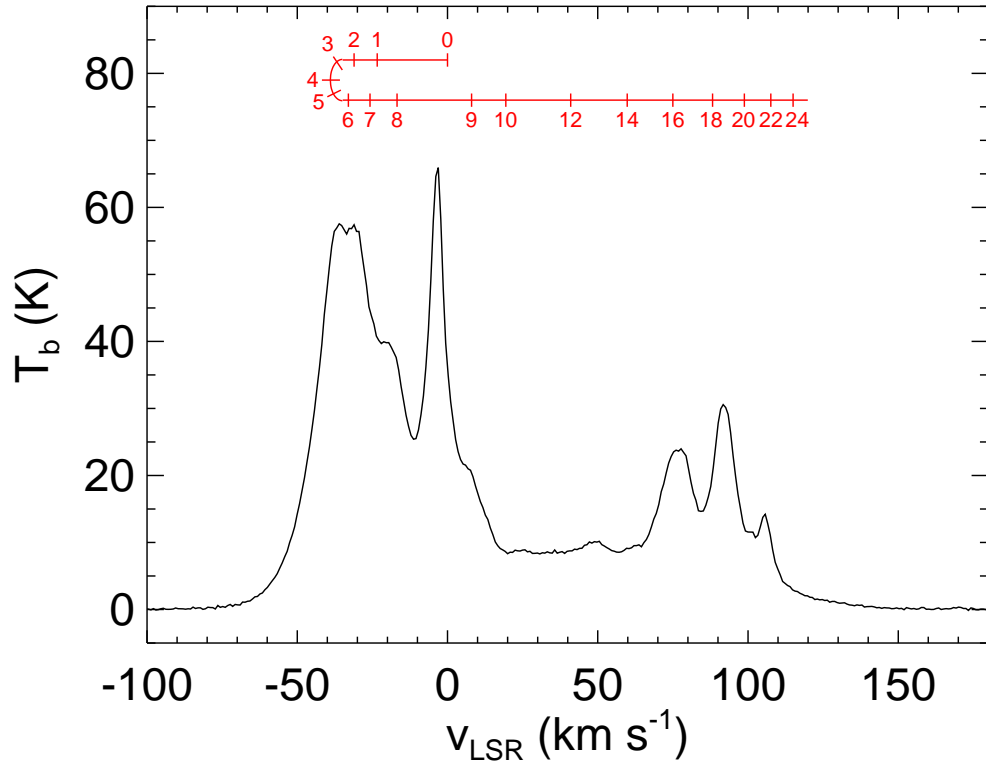[a]Photometry from the NOMAD Catalog (accuracy $\sim$ 0.3 mag)

Figure 3.1 H I emission line profile toward G299.2−2.9. The inset (red scale curve) shows how the heliocentric distance varies with the corresponding v_{LSR}. We adopt the Galactic rotation curve of McClure et al. (2007) inside the solar circle and the flat rotation curve outside the circle with $R_0 = 8.5$ kpc and the Galactic rotation speed at the solar circle $\Theta_0 = 220$ km s^{-1}. The red scale curve is in units of kpc
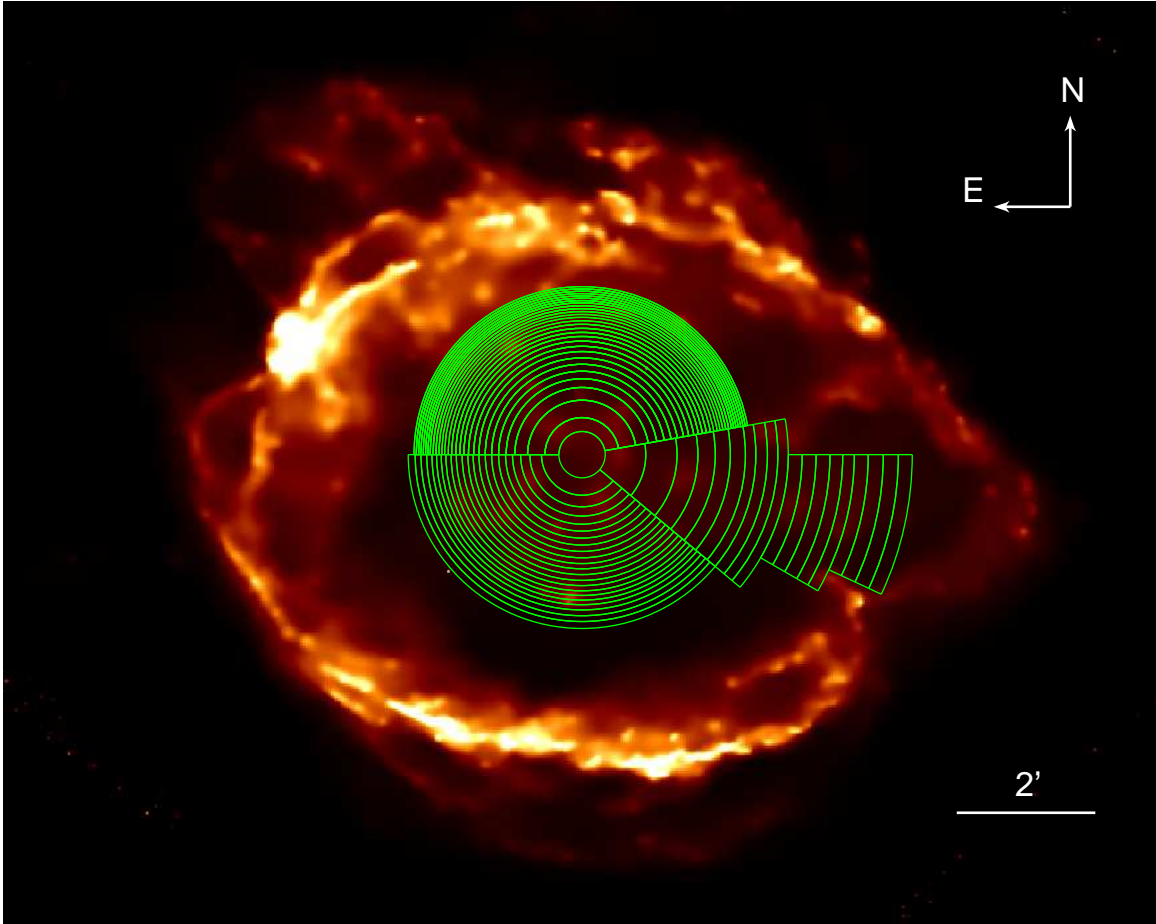
Figure 3.2 Broadband (0.3–3.0 keV) exposure corrected image of G299.2-2.9 with regions selected for ejecta mass calculations shown in green.
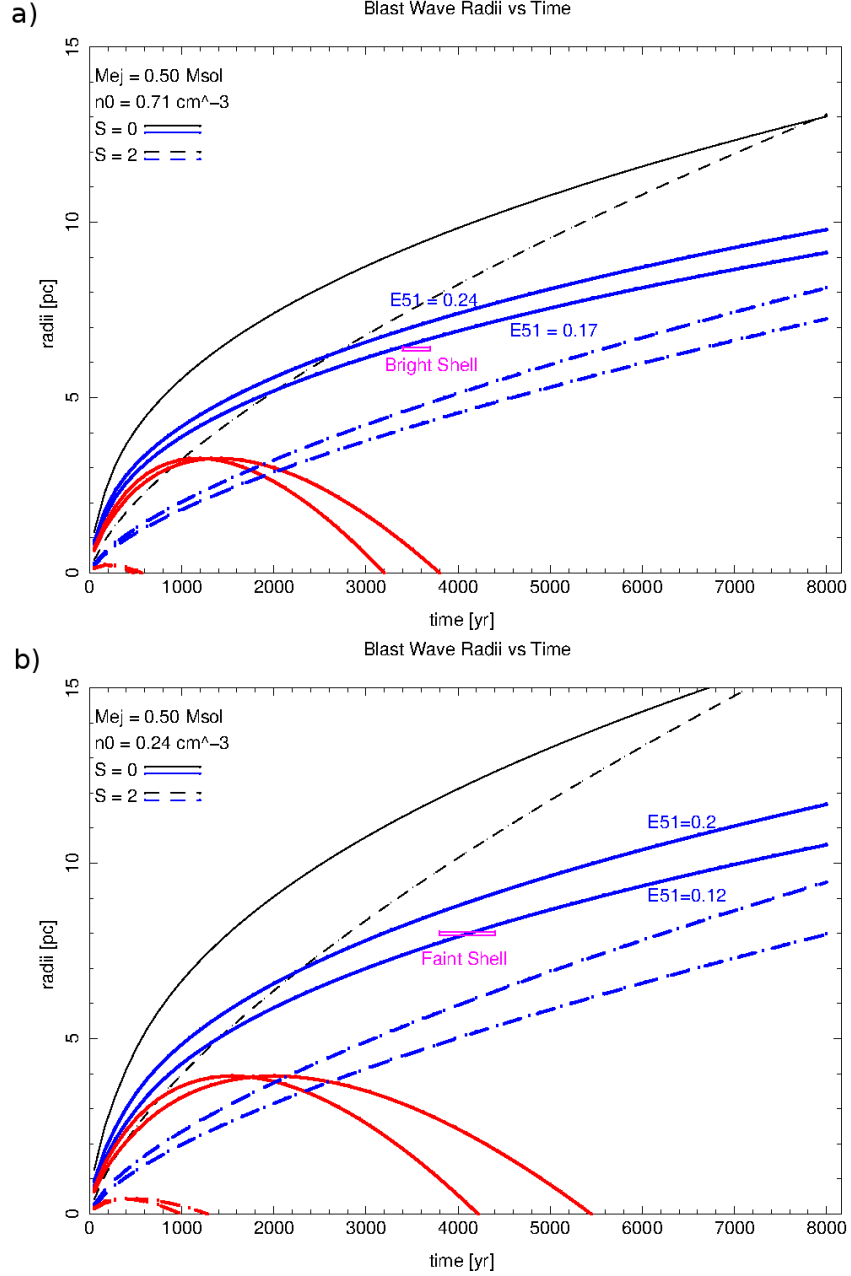
Figure 3.3 Hydrodynamical models for the evolution of the forward (blue lines) and reverse shocks (red lines) with a progenitor mass of 0.5 $M_{\odot}$ ([a] bright inner shell, [b] faint outer shell). The solid lines represent expansion into uniform ambient medium ($s = 0$) and the dashed expansion into wind modified ambient medium ($s = 2$). The black line in all panels represents the evolution of the forward shock for a canonical ($M_{ej} = 1.4\ M_{\odot}$, $E_0 = 1 \times 10^{51}$ erg) Type Ia supernova (the solid line is the uniform medium and the dashed line is the wind modified).
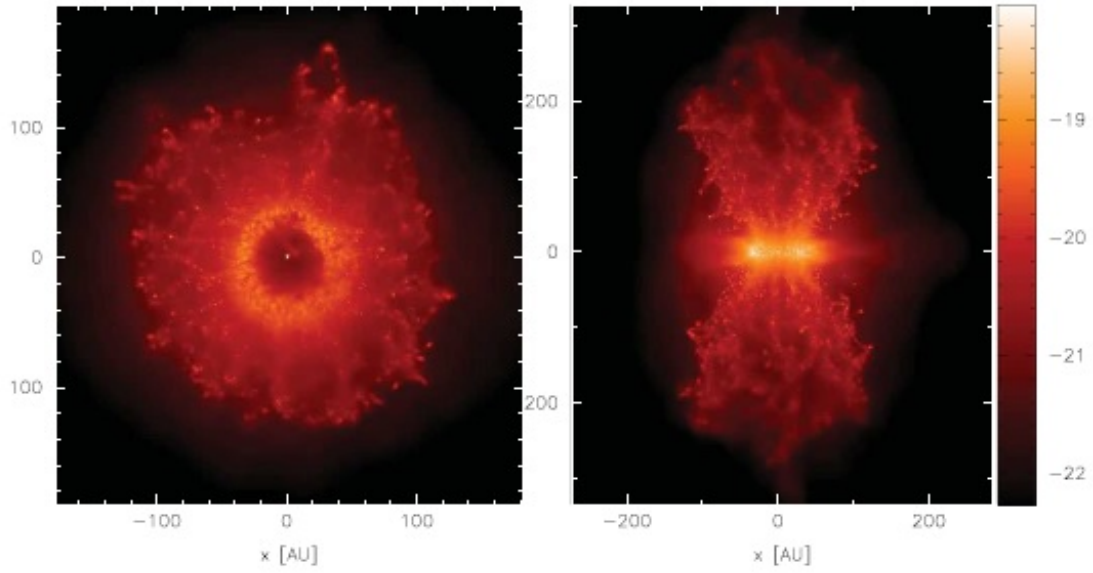
91

Figure 3.4 The projected gas density (y-axis; log $\rho[\mathrm{g\,cm}^3]$) produced by the interaction of a nova with the RS Oph circumstellar medium viewed with inclination angles $0°$ (face-on) [left] and $90°$ (edge-on) [right] credit: Figure 2 in Mohamed et al. (2013).

CHAPTER 4

Summary & Conclusions

We present the results of our comprehensive analysis of the data obtained from our deep *Chandra* observation of Galactic Type Ia supernova remnant G299.2-2.9. Our detailed spatially-resolved spectral analysis of the entire supernova remnant reveals the *complete* spatial distribution of the shocked metal-rich ejecta in G299.2-2.9. The ejecta material is mainly contained within a $\sim4.2'$ diameter circular region at the center of the remnant. We show for the first time an elongation of overabundant ejecta gas extending from the central region out to the western outermost boundary of G299.2-2.9. We also detect candidate metal-rich ejecta material near the southern, and northeastern outermost boundaries, which may be high-velocity ejecta gas resulting from a strongly asymmetric explosion, or caused by non-uniform ejecta expansion into ambient medium with low densities. We estimate a total ejecta mass of $M_{ej} \sim$ 0.5 $M_\odot$ from our hydrodynamical models, which is consistent with with results from our spectral analysis ($\lesssim$0.60 $M_\odot$). We also estimate a total Fe mass $M_{Fe} = 0.17$ $M_\odot$ for G299.2-2.9.

We perform a detailed spatially-resolved spectral analysis of the shell regions of G299.2-2.9 in order to characterize the ambient medium into which the blast wave is expanding. We constructed radial profiles for gas temperature and *EM* behind the forward shock, and compare them to theoretical predictions. Profiles for the bright inner and faint outer shells indicate that the shock is expanding into a uniform ambient medium. Our hydrodynamical model calculations show that the physical size of the bright inner and faint outer shells are also consistent with shocks expanding

into a uniform ambient medium. These results suggest that the complex multi-shell morphology of G299.2-2.9 is the result of an explosion near the boundary between two regions of different ISM densities rather than an explosion from a recurrent nova.

We place a new, conservative upper limit of $\sim$8 kpc on the distance to G299.2-2.9 based on the HI gas distribution along the line of sight. Based on this upper limit, we estimate $d \sim 5$ kpc (with conservative uncertainties of $\sim$50%) for the distance to G299.2-2.9. We estimate the explosion energy $E_0 \sim 1.8 \times 10^{50}$ $d_5^{5/2} f^{-1/2}$ erg. This low explosion energy estimate is not consistent with a canonical explosion of a Type Ia supernova remnant. We also estimate a Sedov age of 3900 yr for the G299.2-2.9.

Based on our results we explore the nature of the progenitor system and explosion mechanism of G299.2-2.9. Various models for the double-detonation of a sub-Chandrasekahr mass white dwarf and also for a failed deflagration of a white dwarf are generally consistent with our estimated values for the low explosion energy, total ejecta mass, total Fe mass and other elemental masses. The observed asymmetry in the ejecta structure of G299.2-2.9 may also be consistent with the asymmetric explosion produced by these models.

REFERENCES

[Anders & Grevesse (1989)] Anders, E., & Grevesse, N. 1989, Geochimica et Cosmochimica Acta, 53, 197

[Baade & Zwicky (1934)] Baade, W., & Zwicky, F. 1934, *Proceedings of the National Academy of Science*, 20, 259-263

[Badenes et al. (2007)] Badenes, C., Hughes, J., Bravo, E., et al. 2007, ApJ, 662, 472

[Badenes & Maoz (2012)] Badenes, C., & Maoz, D. 2012, ApJ, 749, 11

[Baganoff et al. (2001)] Baganoff F., Bautz, M., Feigelson, E., et al. 2001 AAS, 198, 8708

[Bai & Wang (2000)] Bai, L., & Wang, Z. 1995, ApJ, 539, 760

[Booth et al. (2016)] Booth, R., Mohamed, S., & Podsiadlowski, P. 2016, MNRAS, 457, 822

[Borkowski et al. (2001)] Borkowski, K. J., Lyerly, W. J., & Reynolds, S. P. 2001, ApJ, 548, 820

[Bovy et al. (2012)] Bovy, J., Allende, P., Carlos, B., et al. 2012, ApJ, 759, 131

[Branch et al. (1995)] Branch, D., Livio, M., Yungleson, L. R., Boffi, F. R., Baron, E. 1995, PASP, 107, 1019

[Branch et al. (2004)] Branch, D., Baron, E., Thomas, R., et al. 2004, PASP, 116, 903

[Bravo & Garcia-Senz (2008)] Bravo, E., Garcia-Senz, D., 2008, A&A, 478, 843

[Broersen et al. (2014)] Broersen, S., Chiotellis, A., Vink, J., et al. 2014, MNRAS, in press (arXiv:1404.5434)

[Beuther et al. (2002)] Beuther, H., Schilke, P., Sridharan, T., et al. 2002, A&A, 383, 892

[Burkey et al. (2013)] Burkey, M., Reynolds, S., Borkowski, K., et al. 2013, ApJ, 764, 63

[Busser & Aschenbach (1995)] Busser, J.-U., & Aschenbach, B. 1995, IAU Circ. 6142

[Castro et al. (2011)] Castro, D., Slane, P., Patnaude, D., & Ellison, D., 2011 ApJ, 734, 85

[Chamulak et al. (2012)] Chamulak, D., Meakin, C., Sietenzahl, I., & Truran, J. 2012, ApJ, 744, 27

[Chiotellis et al. (2012)] Chiotellis, A., Schure, K., & Vink, J. 2012, A&A, 537, 139

[Churchwell et al. (2009)] Churchwell, E., Babler, B. L., Meade, M. R., et al. 2009, PASP, 121, 213

[della Valle & Livio (1996)] della Valle, M., & Livio, M. 1996, ApJ, 473, 240

[Di Stefano (2010)] Di Stefano, R. 2010, ApJ, 712, 728

[Dilday et al. (2012)] Dilday, B., Howell, D., Cenko, S., et al. 2012, Science, 337, 942

[Doull & Baron (2011)] Doull, B., & Baron, E. 2011, PASP, 123, 765

[Filippenko et al. (1992)] Filippenko, A., Richmon, M., Branch, D., et al. 1992, AJ, 104, 1543

[Filippenko (1997)] Filippenko, A. 1997, PhysReD, 35, 309

[Fink et al. (2007)] Fink, M., Hillebrandt, W., & Röpke, F. 2007, A&A, 476, 1133

[Fink et al. (2010)] Finke, M., Röpke, F., Hillebrandt, W., et al. 2010 A&A, 514, 53

[Fink et al. (2014)] Finke, M., Kromer, M., Seitenzahl, I., et al. 2014 MNRAS, 438, 1762

[Fisher & Jumper (2015)] Fisher, R., & Jumper, K. 2015, ApJ, 805, 150

[Foley et al. (2009)] Foley, R., Chornock, R., Filippenko, A., et al. 2009, AJ, 138, 376

[Foley et al. (2012)] Foley, R., et al. 2012, ApJ, 752, 101

[Foley et al. (2013)] Foley, R., Challis, P., Chornock, R., et al. 2013, ApJ, 767, 57

[Foster et al. (2012)] Foster A., Ji, L., Smith, R., & Brickhouse, N. 2012, ApJj, 756, 128

[Gamezo et al. (2005)] Gamezo, V., Khokhlov, A., & Oran, E. 2005, ApJ, 623, 337

[Garmire et al. (2003)] Garmire, G., Bautz, M., Mark, W., & et al. 2003, SPIE, 4851, 28

[Ghavamian et al. (2007)] Ghavamian, P., Laming, J., & Rakowski, C. 2007, ApJ, 654, L69

[Guo & Burrows (1997)] Gou, Z., & Burrows, D. 1997, ApJ, 480, 51

[Hachisu & Kato (2001)] Hachisu, I., Kato, M. 2001, ApJ, 540, 447

[Hamuy et al. (1993)] Hamuy, M., Maza, J., Phillips, M., et al. 1993, AJ, 106, 2392

[Hamuy et al. (2003)] Hamuy, M. 2003, Nature, 424

[Helder et al. (2009)] Helder, E., et al. 2009, Science, 325, 719

[Hillebrandt & Niemeyer (2000)] Hillebrandt, W., & Niemeyer, J. 2000, AAR&A, 38, 191

[Hughes et al. (2003)] Hughes, J., Ghavamian, P., Rakowski, C., & Slane, P. 2003, ApJ, 582, L95

[Hughes et al. (2007(] Hughes, J., Chugai, N., Chevalier, R., Lundqvist, P., & Schlegel, E. 2007, ApJ, 670, 1260

[Hwang et al. (2000)] Hwang, U., Holt, S., & Petre, R. 2000, ApJ, 537, 119

[Whang & Laming (2012)] Hwang, U., & Laming, J. 2012, ApJ, 746, 130

[Iben & Tutukov (1984)] Iben, I., & Tutukov, A. 1984, ApJ, 284, 719

[Iwamoto et al. (1999)] Iwamoto, K., Brachwitz, F., Nomoto, K., Kishimoto, N., Umeda, H., Hiz, R., & Thielemann, F. 1999, ApJ, 125, 439

[Jha et al. (2006)] Jha, S., Branch, D., Chornock, R., et al. 2006, AJ, 132, 189

[Jordan et al. (2012)] Jordan, G., IV, Perets, H., Fisher, R., et al. 2012, ApJ, 761, 23

[Kashi & Soker (2011)] Kashi, A., & Soker, N. 2011, MNRAS, 417, 1466

[Katsuda et al. (2015)] Katsuda, S., Raymond, J., Blair, W., et al. 2015, ApJ, 817, 36

[Katz & Dong (2012)] Katz, B., & Dong, S. 2012, arXiv:1211.4584

[Khokhlov (1991b)] Khokhlov, A. 1991, AAP, 245, L25

[Khokhlov (1995)] Khokhlov, A. 1995, ApJ, 449, 695

[Kippenhahn & Weigert (2012)] Kippenhahn, R., & Weigert, A. 1994, Stellar Structure and Evolution, (2nd ed. Astronomy and Astrophysics Library)

[Kotak (2008)] Kotak, R. 2008, ASPC 401, *RS Ophiuchi (2006) and the Recurrent Nova Phenomenon*, ed. A. Evans, M. F. Bode, T. J. OBrien, & M. J. Darnley, 150

[Kromer et al. (2010)] Kromer M., Sim S., Fink, M., et al. 2010, ApJ, 719, 106

[Kromer et al. (2013)] Kromer, M., Fink, M., Stanishev, V., et al. 2013, MNRAS, 429, 2287

[Kushnir et al. (2013)] Kushnir, D., Katz, B., Dong, S., Livne, E., et al. 2013, ApJ, 778, 37

[Langer et al. (2002)] Langer, N., Yoon, S., Wellstein, S., et al. 2002, ASPC 261, *The Physics of Cataclysmic Variables and Related Objects*, ed. B.T. Gänsicke, K. Beuermann, & K. Reinsch, 252

[Laughlin et al. (1997)] Laughlin, G., Bodenheimer, P., & Adams, F. 1997, ApJ, 482, 420

[Lee et al.(2010)] Lee, J., Park, S., Hughes, J., Slane, P., Gaensler, B., Ghavamian, P., & Burrows, D. 2008, ApJ, 711, 861L

[Lee et al.(2014)] Lee, j., Park, S., Hughes, J., Slane, P. 2014, ApJ, 789, 7L

[Leonard (2007)] Leonard, D. 2007, ApJ, 670, 1275

[Li et al. (2003)] Li, W., Filippenko, A., Chornock, R., et al. 2003, PASP, 115, 453

[Li et al. (2011a)] Li, W., Chornock, R., Leaman, J., et al. 2011, MNRAS, 412, 1441

[Li et al. (2011b)] Li, W., Leaman, J., Chornock, R., et al. 2011, MNRAS, 412, 1472

[Liedahl et al. (1995)] Liedahl, D., Osterheld, A., & Goldstein, W. 1995, ApJ, 438, 115

[Liszt (1983)] Liszt, H. 1983, ApJ, 275,163

[Livio & Riess (2003)] Livio, M., & Riess, A. 2003, ApJ, 594, 93

[Livne & Arnett (1995)] Livne, E., & Arnett, D. 1995, ApJ, 452, 62L

[Lopez et al. (2009)] Lpoez, L., Ramirez-Ruiz, E., Badenes, C., et al. 2009, ApJ, 706, 106

[Lopez et al. (2011)] Lopez, L., Ramirez-Ruiz, E., Badenes, C., Huppenkothen, D., & Pooley, D. 2011, ApJ, 732, 114

[Lyman et al. (2013)] Lyman, J., James, P., Perets, H., Anderson, J., Gal-Yam, A., Mazzali, P., & Percival, S. 2013, MNRAS, 434, 527

[Lyman et al. (2013)] Lyman, J., James, P., Perets, H., et al. 2013, MNRAS, 434, 527

[Maeda et al. (2010)] Maeda, K., et al. 2010, Nature, 466, 82

[Maguire et al (2013)] Maguire, K., et al. 2013, MNRAS, 436, 222

[Malone et al. (2014)] Malone, C., Nonaka, A., Woosley, S., Almgren, A., Bell, J., Dong, S., & Zingale, M. 2013, ApJ, 782, 11

[Maoz & Mannucci (2013)] Maoz, D., & Mannucci, F. 2013, PASA, 29, 447

[Maoz et al. (2014)] Maoz, D., Mannucci, F. & Nelemans, G. 2014, ARA&A, 52, 107

[Maund et al. (2010)] Maund, J., Höflich, P., Patat, F., Wheeler, C., Zelaya, P., Baade, D., Wang, L., Clocchiatti, A., & Quinn, J. 2010, ApJ, 725, L167

[McClure-Griffiths et al. (2005)] McClure-Griffiths, N. M., Dickey, J. M., Gaensler, B. M., et al. 2005, ApJs, 158, 178

[McClure-Griffiths & Dickey (2007)] McClure-Griffiths, N. M., & Dickey, J. M. 2007, ApJ, 671, 427

[McKee (1974)] McKee, C. F. 1974, ApJ, 188, 335

[Miceli et al. (2013)] Miceli, M., Orlando, S., Reale, F., et al. 2013, MNRAS, 430, 2864

[Mohamed et al. (2013)] Mohamed, S., Booth, R., & Podsiadlowski, P. 2013, ASPC, 469

[Murray (2001)] Murray, S. 2001, ASPC, 234, 155

[Nomoto & Iben (1985)] Nomoto, K., & Iben, I. 1984, ApJ, 297, 531

[Nomoto et al. (2006)] Nomoto, K., Tominaga, N., Umeda, H., Kobayashi, C., & Maeda, K. 2006, Nuclear Physics A, 777, 424

[Ott et al. (2012)] Ott, C., Abdikamalov, E., O'Conner, E., et al. 2012, ARA&A, 86, 024026

[Pakmor et al. (2010)] Pakmor, R., Kromer, M., R opke, F., et al. 2010, Nature, 463, 61

[Pakmor et al. (2012)] Pakmor, R., Kromer, M., Taubenberger, S., et al. 2010, Apj, 747, 10

[Pan et al. (2014)] Pan, K., Ricker, P., & Taam. R. 2014, ApJ, 792, 71

[Papish et al. (2015)] Papish, O., Soker, N., Garca-Berro, E., & AznarSiguan, G. 2015, MNRAS, 449, 1

[Park et al. (2002)] Park, S., Roming, P., Hughes, J., Slane, P., Burrows, D., Garmire, G., & Nousek, J. 2002, ApJ, 564, L39

[Park et al. (2007)] Park, S., Slane, P., Hughes, J., Mori, K., Burrows, D., & Garmire, G. P. 2007, ApJ, 665, 1173

[Park et al. (2012)] Park, S., Hughes, J., Slane, P., et al. 2012, ApJ, 748, 117

[Park et al. (2013)] Park, S., Badenes, C., Mori, K., et al. 2013, ApJ, 767, 10

[Patel et al. (2005)] Patel, N., Curiel, S., Sridharan, T., et al. 2005, Nature, 437, 109

[Patet et al. (2007)] Patet, F., et al. 2007, Science, 317, 924

[Patnaude et al. (2012)] Patnaude, D., Badenes, C., Park, S., & Laming, J. 2012, ApJ, 756, 6

[Perlmutter et al. (1999)] Perlmutter, S., Aldering, G., Goldhaber, G., et al. 1999, ApJ, 517, 565

[Phillips (1993)] Phillips, M. 1993, ApJ, 413, 105

[Post el al. (2014)] Post, S., Park, S., et al. 2014, ApJ,

[Rakowski et al. (2006)] Rakowski, C., Badenes, C., Gaensler, B., Gelfand, J., Hughes, J., & Slane, P. 2006, ApJ, 646, 982

[Reynolds (2007)] Reynolds, S., Borkowski, K., Hwang, U., et al. 2007, ApJ, 668, 135

[Reynolds (2008)] Reynolds, S. R. 2008, ARA&A, 46, 89

[Riess et al. (1998)] Riess, A., Filippenko, A., Challis, P., et al. 1998, AJ, 116, 1009

[Ropke et al. (2006)] Ropke, F., Hillebrandt, W., Niemeyer, J., et al. 2006, A&A, 448, 1

[Rosswog et al. (2009)] Rosswog, S., Kasen, D., Guillochon, J., et al. 2009, ApJ, 705, 128

[Ruiter et al. (2011)] Ruiter, A. J., Belczynski, K., Sim, S., Hillebrandt, W., Fryer, C., Fink, M., & Kromer, M. 2011, MNRAS, 417, 408

[Scalzo et al. (2014)] Scalzo, R., Ruiter, A., & Sim, S. 2014, MNRAS, 445, 2535

[Sedov (1959)] Sedov, L. I. 1959, Similarity and Dimensional Methods in Mechanics (New York: Academic)

[Shen et al. (2013)] Shen, K., Guillochon, J., & Foley, R. 2013, ApJ, 770, L35

[Sim et al. (2010)] Sim, S., Röpke, F., Hillebrandt, W., et al. 2010, ApJ, 714, 52

[Sim et al. (2012)] Sim, S., Fink, M., Kromer, M., et al. 2012, MNRAS, 420, 3003

[Simon et al. (2009)] Simon, J., et al. 2009, ApJ, 702, 1157

[Slane et al. (1996)] Slane, P., Vancura, O., & Hughes, J. 1996, ApJ, 465, 840

[Smith et al. (2001)] Smith, R., Brickhouse, N., Liedahl, D., & Raymond, J. 2001, ApJ, 556, L91

[Soker et al. (2013)] Soker, N., Kashi, A., Garcia-Berro, E., Torres, S., & Camacho, J. 2013, MNRAS, 431, 1541

[Soker et al. (2014)] Soker, N. 2014 Submitted (arXiv:1405.0173)

[Staveley-Smith et al.(1996)] Staveley-Smith et al. 1996, PASA 13, 243

[Sternberg et al. (2011)] Sterberg, A., Gal-Yam, A., Simon, D., et al. 2011, Science, 333, 856

[Sullivan et al. (2011)] Sullivan, M., Kasliwal, M., Nugent, P., et al. 2011, ApJ, 732, 118

[Thielemann et al. (1986)] Thielemann, F., Nomoto, K., & Yokoi, K. 1986, A&A, 158, 17

[Townsley et al. (2000)] Townsley, L., Broos, P., Garmire, G., & Nousek, J. 2000, ApJ, 534, L139

[Townsley & Bildsten (2005)] Townsley, D., Bildsten, L. 2005, ApJ, 628, 395

[Tsebrenko & Soker (2013)] Tsebrenko, D., & Soker, N. 2013, MNRAS, 435, 320

[Uchida et al. (2013)] Uchida, H., Yamaguchi, H., & Koyama, K. 2013, ApJ, 771, 56

[Valenti et al. (2009)] Valenti, S., Pastorello, A., Cappellaro, E., et al. 2009, Nature, 459, 674

[van Dyk (1992)] van Dyk, S. 1992, AJ, 103, 1788

[Vancura et al. (1995)] Vancura, O., Gorenstein, P., & Hughes, J. 1995, ApJ, 441, 680

[Van Kerwijk et al. (2010)] van Kerwijk, M., Chang, P., & Justham, S., 2010, ApJ, 722, 157

[Wang & Chevalier(2001)] Wang, C., & Chevalier, R. 2001, ApJ, 549, 1119

[Wang & Wheeler (2008)] Wang, L., & Wheeler, J. 2008, ARA&A 46, 433

[Whittet (2003)] Whittet, D. 2003, *Dust in the Galactic Environment*, CRC Press

[Winkler et al. (2014)] Winkler, F., Williams, B., Reynolds, S., et al., & Hwang, U. 2014, ApJ, 781, 65

[Woosley & Weaver (1994)] Woosley, S., & Weaver, T. 1994, ApJ, 423, 371

[Yamaguchi et al. (2014)] Yamaguchi, H., et al. 2014, ApJ, 785L, 27

[Yamaguchi et al. (2015)] Yamaguchi, H., Badenes, C., Foster, A., et al. 2014, ApJ, 801, 31